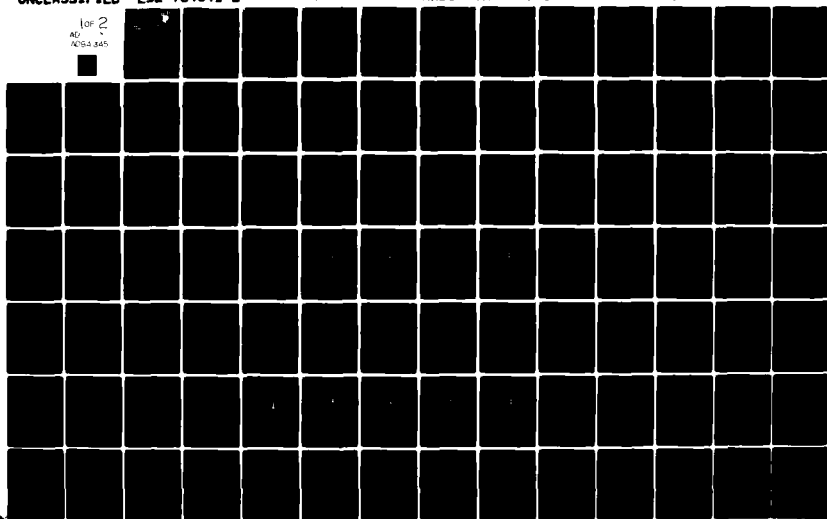


AD-A084 345

OHIO STATE UNIV COLUMBUS ELECTROSCIENCE LAB F/G 20/14
RADIATION BY SOURCES ON PERFECTLY CONDUCTING CONVEX CYLINDERS M--ETC(U)
JAN 80 L ERSOY, P H PATHAK F19628-77-C-0107
ESL-784641-2 RADC -TR-79-281 NL

UNCLASSIFIED

1 of 2
AD-A084 345



5.4
12
RADC-TR-79-281

Final Technical Report

January 1980

LEVEL



RADIATION BY SOURCES ON PERFECTLY CONDUCTING CONVEX CYLINDERS WITH AN IMPEDANCE SURFACE PATCH

The Ohio State University ElectroScience Laboratory

L. Ersoy
P. H. Pathak

APPROVED FOR PUBLIC RELEASE; DISTRIBUTION UNLIMITED

DTIC
ELECTE
MAY 20 1980
S A D

**ROME AIR DEVELOPMENT CENTER
Air Force Systems Command
Griffiss Air Force Base, New York 13441**

80 5 19 021

ADA 084345

FILE COPY

This report has been reviewed by the RADC Public Affairs Office (PA) and is releasable to the National Technical Information Service (NTIS). At NTIS it will be releasable to the general public, including foreign nations.

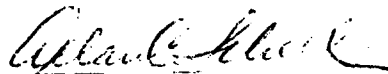
RADC-TR-79-281 has been reviewed and is approved for publication.

APPROVED:



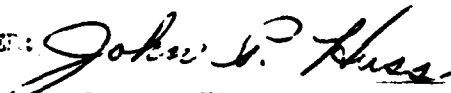
NICHOLAS P. KERNWEIS
Contract Monitor

APPROVED:



ALLAN C. SCHELL, Chief
Electromagnetic Sciences Division

FOR THE COMMANDER:



JOHN P. HUSS
Acting Chief, Plans Office

If your address has changed or if you wish to be removed from the RADC mailing list, or if the addressee is no longer employed by your organization, please notify RADC (EEA) Hanscom AFB MA 01731. This will assist us in maintaining a current mailing list.

Do not return this copy. Retain or destroy.

| 19 REPORT DOCUMENTATION PAGE | | READ INSTRUCTIONS BEFORE COMPLETING FORM | |
|---|-------------------------------------|---|--------|
| 1. REPORT NUMBER 18 RADC-TR-79-281 | 2. GOVT ACCESSION NO. AD A084345 | 3. RECIPIENT'S CATALOG NUMBER | |
| 4. TITLE (and Subtitle) 6 RADIATION BY SOURCES ON PERFECTLY CONDUCTING CONVEX CYLINDERS WITH AN IMPEDANCE SURFACE Patch. | | 5. TYPE OF REPORT & PERIOD COVERED 9 Final Technical Report - 6 Jan 77 - 5 Jan 79 | |
| 7. AUTHOR(s) 10 L./Ersoy P. H./Pathak | | 14. PERFORMING ORG. REPORT NUMBER 14 ESL-784641-2 | |
| 8. PERFORMING ORGANIZATION NAME AND ADDRESS Ohio State University ElectroScience Laboratory Department of Electrical Engineering Columbus OH 43212 | | 15. CONTRACT OR GRANT NUMBER(s) 15 F19628-77-C-0107 | |
| 11. CONTROLLING OFFICE NAME AND ADDRESS Deputy for Electronic Technology (RADC/EEA) Hanscom AFB MA 01731 | | 10. PROGRAM ELEMENT, PROJECT, TASK AREA & WORK UNIT NUMBERS 61102F 2305306 | 17. J3 |
| 14. MONITORING AGENCY NAME & ADDRESS (if different from Controlling Office) Same | | 12. REPORT DATE January 1980 | |
| 16. DISTRIBUTION STATEMENT (of this Report) Approved for public release; distribution unlimited. | | 13. NUMBER OF PAGES 122 | |
| 17. DISTRIBUTION STATEMENT (of the abstract entered in Block 20, if different from Report) Same | | 15. SECURITY CLASS. (of this report) UNCLASSIFIED | |
| 18. SUPPLEMENTARY NOTES The material contained in this report is also used as a dissertation submitted to the Ohio State University Graduate School as partial fulfillment for the degree Doctor of Philosophy. RADC Project Engineer: Nicholas P. Kernweis (EEA) | | 15a. DECLASSIFICATION/DOWNGRADING SCHEDULE N/A | |
| 19. KEY WORDS (Continue on reverse side if necessary and identify by block number) Impedance Surfaces Perfectly conducting cylinders partly covered by an impedance patch Radiation from Sources on an impedance patch Asymptotic high frequency solutions Currents excited by sources on curved impedance surfaces Perturbation type integral equations | | | |
| 20. ABSTRACT (Continue on reverse side if necessary and identify by block number) → This report deals with an asymptotic high frequency analysis of the radiation patterns of a magnetic line source, or a magnetic line dipole, located on a uniform impedance surface patch which partly covers an electrically large perfectly conducting convex cylinder. This work is relevant, for example, to the analysis of fuselage mounted airborne antennas for satellite communication purposes. In the latter application impedance surface patches may be employed to increase the radiation intensity near the horizon over that which would ordinarily exist in the absence of any such impedance loading. In the present | | | |

UNCLASSIFIED

SECURITY CLASSIFICATION OF THIS PAGE(When Data Entered)

analysis, the impedance surface patch is represented as an equivalent aperture in the rest of the perfectly conducting convex cylinder. Approximate asymptotic expressions for the "equivalent aperture distribution;" i.e., for the "currents on the impedance surface patch" are developed in this work for the two source types; these expressions for the currents are valid in the neighborhood of the source. The radiation pattern of this configuration is then found in a straightforward manner by numerically integrating this current distribution in conjunction with a simple and accurate asymptotic high frequency form of the perfectly conducting, convex cylinder Green's function. Since the cylinder Green's function is employed, one needs to integrate only over the currents which exist on the impedance surface patch (i.e., over the equivalent aperture) and not over the currents on the remaining, perfectly conducting, portion of the cylinder. Radiation pattern calculations based on this analysis are found to compare quite well with a numerical moment method type solution, a previous GTD solution for those impedances which support an Elliot mode, and also with some presently available experimental results. It is seen that a moderately large increase in the radiation intensity can be obtained in the vicinity of the horizon for cylinders loaded by an impedance surface which support Elliot type modes.

| | |
|---|--|
| Accession For | |
| 1. U.S. Army | <input checked="checked" type="checkbox"/> |
| 2. U.S. Navy | <input type="checkbox"/> |
| 3. U.S. Air Force | <input type="checkbox"/> |
| 4. U.S. Marine Corps | <input type="checkbox"/> |
| 5. U.S. Coast Guard | <input type="checkbox"/> |
| 6. U.S. Customs Service | <input type="checkbox"/> |
| 7. U.S. Department of Justice | <input type="checkbox"/> |
| 8. U.S. Department of Education | <input type="checkbox"/> |
| 9. U.S. Department of Health, Education & Welfare | <input type="checkbox"/> |
| 10. U.S. Department of Agriculture | <input type="checkbox"/> |
| 11. U.S. Department of the Interior | <input type="checkbox"/> |
| 12. U.S. Department of Energy | <input type="checkbox"/> |
| 13. U.S. Department of Transportation | <input type="checkbox"/> |
| 14. U.S. Department of Commerce | <input type="checkbox"/> |
| 15. U.S. Department of Labor | <input type="checkbox"/> |
| 16. U.S. Department of Housing & Urban Development | <input type="checkbox"/> |
| 17. U.S. Department of Social Services | <input type="checkbox"/> |
| 18. U.S. Department of Veterans Affairs | <input type="checkbox"/> |
| 19. U.S. Department of State | <input type="checkbox"/> |
| 20. U.S. Department of Defense | <input type="checkbox"/> |
| 21. U.S. Department of the Treasury | <input type="checkbox"/> |
| 22. U.S. Department of the Environment | <input type="checkbox"/> |
| 23. U.S. Department of the Interior | <input type="checkbox"/> |
| 24. U.S. Department of Energy | <input type="checkbox"/> |
| 25. U.S. Department of Transportation | <input type="checkbox"/> |
| 26. U.S. Department of Commerce | <input type="checkbox"/> |
| 27. U.S. Department of Labor | <input type="checkbox"/> |
| 28. U.S. Department of Housing & Urban Development | <input type="checkbox"/> |
| 29. U.S. Department of Social Services | <input type="checkbox"/> |
| 30. U.S. Department of Veterans Affairs | <input type="checkbox"/> |
| 31. U.S. Department of State | <input type="checkbox"/> |
| 32. U.S. Department of Defense | <input type="checkbox"/> |
| 33. U.S. Department of the Treasury | <input type="checkbox"/> |
| 34. U.S. Department of the Environment | <input type="checkbox"/> |
| 35. U.S. Department of the Interior | <input type="checkbox"/> |
| 36. U.S. Department of Energy | <input type="checkbox"/> |
| 37. U.S. Department of Transportation | <input type="checkbox"/> |
| 38. U.S. Department of Commerce | <input type="checkbox"/> |
| 39. U.S. Department of Labor | <input type="checkbox"/> |
| 40. U.S. Department of Housing & Urban Development | <input type="checkbox"/> |
| 41. U.S. Department of Social Services | <input type="checkbox"/> |
| 42. U.S. Department of Veterans Affairs | <input type="checkbox"/> |
| 43. U.S. Department of State | <input type="checkbox"/> |
| 44. U.S. Department of Defense | <input type="checkbox"/> |
| 45. U.S. Department of the Treasury | <input type="checkbox"/> |
| 46. U.S. Department of the Environment | <input type="checkbox"/> |
| 47. U.S. Department of the Interior | <input type="checkbox"/> |
| 48. U.S. Department of Energy | <input type="checkbox"/> |
| 49. U.S. Department of Transportation | <input type="checkbox"/> |
| 50. U.S. Department of Commerce | <input type="checkbox"/> |
| 51. U.S. Department of Labor | <input type="checkbox"/> |
| 52. U.S. Department of Housing & Urban Development | <input type="checkbox"/> |
| 53. U.S. Department of Social Services | <input type="checkbox"/> |
| 54. U.S. Department of Veterans Affairs | <input type="checkbox"/> |
| 55. U.S. Department of State | <input type="checkbox"/> |
| 56. U.S. Department of Defense | <input type="checkbox"/> |
| 57. U.S. Department of the Treasury | <input type="checkbox"/> |
| 58. U.S. Department of the Environment | <input type="checkbox"/> |
| 59. U.S. Department of the Interior | <input type="checkbox"/> |
| 60. U.S. Department of Energy | <input type="checkbox"/> |
| 61. U.S. Department of Transportation | <input type="checkbox"/> |
| 62. U.S. Department of Commerce | <input type="checkbox"/> |
| 63. U.S. Department of Labor | <input type="checkbox"/> |
| 64. U.S. Department of Housing & Urban Development | <input type="checkbox"/> |
| 65. U.S. Department of Social Services | <input type="checkbox"/> |
| 66. U.S. Department of Veterans Affairs | <input type="checkbox"/> |
| 67. U.S. Department of State | <input type="checkbox"/> |
| 68. U.S. Department of Defense | <input type="checkbox"/> |
| 69. U.S. Department of the Treasury | <input type="checkbox"/> |
| 70. U.S. Department of the Environment | <input type="checkbox"/> |
| 71. U.S. Department of the Interior | <input type="checkbox"/> |
| 72. U.S. Department of Energy | <input type="checkbox"/> |
| 73. U.S. Department of Transportation | <input type="checkbox"/> |
| 74. U.S. Department of Commerce | <input type="checkbox"/> |
| 75. U.S. Department of Labor | <input type="checkbox"/> |
| 76. U.S. Department of Housing & Urban Development | <input type="checkbox"/> |
| 77. U.S. Department of Social Services | <input type="checkbox"/> |
| 78. U.S. Department of Veterans Affairs | <input type="checkbox"/> |
| 79. U.S. Department of State | <input type="checkbox"/> |
| 80. U.S. Department of Defense | <input type="checkbox"/> |
| 81. U.S. Department of the Treasury | <input type="checkbox"/> |
| 82. U.S. Department of the Environment | <input type="checkbox"/> |
| 83. U.S. Department of the Interior | <input type="checkbox"/> |
| 84. U.S. Department of Energy | <input type="checkbox"/> |
| 85. U.S. Department of Transportation | <input type="checkbox"/> |
| 86. U.S. Department of Commerce | <input type="checkbox"/> |
| 87. U.S. Department of Labor | <input type="checkbox"/> |
| 88. U.S. Department of Housing & Urban Development | <input type="checkbox"/> |
| 89. U.S. Department of Social Services | <input type="checkbox"/> |
| 90. U.S. Department of Veterans Affairs | <input type="checkbox"/> |
| 91. U.S. Department of State | <input type="checkbox"/> |
| 92. U.S. Department of Defense | <input type="checkbox"/> |
| 93. U.S. Department of the Treasury | <input type="checkbox"/> |
| 94. U.S. Department of the Environment | <input type="checkbox"/> |
| 95. U.S. Department of the Interior | <input type="checkbox"/> |
| 96. U.S. Department of Energy | <input type="checkbox"/> |
| 97. U.S. Department of Transportation | <input type="checkbox"/> |
| 98. U.S. Department of Commerce | <input type="checkbox"/> |
| 99. U.S. Department of Labor | <input type="checkbox"/> |
| 100. U.S. Department of Housing & Urban Development | <input type="checkbox"/> |
| 101. U.S. Department of Social Services | <input type="checkbox"/> |
| 102. U.S. Department of Veterans Affairs | <input type="checkbox"/> |
| 103. U.S. Department of State | <input type="checkbox"/> |
| 104. U.S. Department of Defense | <input type="checkbox"/> |
| 105. U.S. Department of the Treasury | <input type="checkbox"/> |
| 106. U.S. Department of the Environment | <input type="checkbox"/> |
| 107. U.S. Department of the Interior | <input type="checkbox"/> |
| 108. U.S. Department of Energy | <input type="checkbox"/> |
| 109. U.S. Department of Transportation | <input type="checkbox"/> |
| 110. U.S. Department of Commerce | <input type="checkbox"/> |
| 111. U.S. Department of Labor | <input type="checkbox"/> |
| 112. U.S. Department of Housing & Urban Development | <input type="checkbox"/> |
| 113. U.S. Department of Social Services | <input type="checkbox"/> |
| 114. U.S. Department of Veterans Affairs | <input type="checkbox"/> |
| 115. U.S. Department of State | <input type="checkbox"/> |
| 116. U.S. Department of Defense | <input type="checkbox"/> |
| 117. U.S. Department of the Treasury | <input type="checkbox"/> |
| 118. U.S. Department of the Environment | <input type="checkbox"/> |
| 119. U.S. Department of the Interior | <input type="checkbox"/> |
| 120. U.S. Department of Energy | <input type="checkbox"/> |
| 121. U.S. Department of Transportation | <input type="checkbox"/> |
| 122. U.S. Department of Commerce | <input type="checkbox"/> |
| 123. U.S. Department of Labor | <input type="checkbox"/> |
| 124. U.S. Department of Housing & Urban Development | <input type="checkbox"/> |
| 125. U.S. Department of Social Services | <input type="checkbox"/> |
| 126. U.S. Department of Veterans Affairs | <input type="checkbox"/> |
| 127. U.S. Department of State | <input type="checkbox"/> |
| 128. U.S. Department of Defense | <input type="checkbox"/> |
| 129. U.S. Department of the Treasury | <input type="checkbox"/> |
| 130. U.S. Department of the Environment | <input type="checkbox"/> |
| 131. U.S. Department of the Interior | <input type="checkbox"/> |
| 132. U.S. Department of Energy | <input type="checkbox"/> |
| 133. U.S. Department of Transportation | <input type="checkbox"/> |
| 134. U.S. Department of Commerce | <input type="checkbox"/> |
| 135. U.S. Department of Labor | <input type="checkbox"/> |
| 136. U.S. Department of Housing & Urban Development | <input type="checkbox"/> |
| 137. U.S. Department of Social Services | <input type="checkbox"/> |
| 138. U.S. Department of Veterans Affairs | <input type="checkbox"/> |
| 139. U.S. Department of State | <input type="checkbox"/> |
| 140. U.S. Department of Defense | <input type="checkbox"/> |
| 141. U.S. Department of the Treasury | <input type="checkbox"/> |
| 142. U.S. Department of the Environment | <input type="checkbox"/> |
| 143. U.S. Department of the Interior | <input type="checkbox"/> |
| 144. U.S. Department of Energy | <input type="checkbox"/> |
| 145. U.S. Department of Transportation | <input type="checkbox"/> |
| 146. U.S. Department of Commerce | <input type="checkbox"/> |
| 147. U.S. Department of Labor | <input type="checkbox"/> |
| 148. U.S. Department of Housing & Urban Development | <input type="checkbox"/> |
| 149. U.S. Department of Social Services | <input type="checkbox"/> |
| 150. U.S. Department of Veterans Affairs | <input type="checkbox"/> |
| 151. U.S. Department of State | <input type="checkbox"/> |
| 152. U.S. Department of Defense | <input type="checkbox"/> |
| 153. U.S. Department of the Treasury | <input type="checkbox"/> |
| 154. U.S. Department of the Environment | <input type="checkbox"/> |
| 155. U.S. Department of the Interior | <input type="checkbox"/> |
| 156. U.S. Department of Energy | <input type="checkbox"/> |
| 157. U.S. Department of Transportation | <input type="checkbox"/> |
| 158. U.S. Department of Commerce | <input type="checkbox"/> |
| 159. U.S. Department of Labor | <input type="checkbox"/> |
| 160. U.S. Department of Housing & Urban Development | <input type="checkbox"/> |
| 161. U.S. Department of Social Services | <input type="checkbox"/> |
| 162. U.S. Department of Veterans Affairs | <input type="checkbox"/> |
| 163. U.S. Department of State | <input type="checkbox"/> |
| 164. U.S. Department of Defense | <input type="checkbox"/> |
| 165. U.S. Department of the Treasury | <input type="checkbox"/> |
| 166. U.S. Department of the Environment | <input type="checkbox"/> |
| 167. U.S. Department of the Interior | <input type="checkbox"/> |
| 168. U.S. Department of Energy | <input type="checkbox"/> |
| 169. U.S. Department of Transportation | <input type="checkbox"/> |
| 170. U.S. Department of Commerce | <input type="checkbox"/> |
| 171. U.S. Department of Labor | <input type="checkbox"/> |
| 172. U.S. Department of Housing & Urban Development | <input type="checkbox"/> |
| 173. U.S. Department of Social Services | <input type="checkbox"/> |
| 174. U.S. Department of Veterans Affairs | <input type="checkbox"/> |
| 175. U.S. Department of State | <input type="checkbox"/> |
| 176. U.S. Department of Defense | <input type="checkbox"/> |
| 177. U.S. Department of the Treasury | <input type="checkbox"/> |
| 178. U.S. Department of the Environment | <input type="checkbox"/> |
| 179. U.S. Department of the Interior | <input type="checkbox"/> |
| 180. U.S. Department of Energy | <input type="checkbox"/> |
| 181. U.S. Department of Transportation | <input type="checkbox"/> |
| 182. U.S. Department of Commerce | <input type="checkbox"/> |
| 183. U.S. Department of Labor | <input type="checkbox"/> |
| 184. U.S. Department of Housing & Urban Development | <input type="checkbox"/> |
| 185. U.S. Department of Social Services | <input type="checkbox"/> |
| 186. U.S. Department of Veterans Affairs | <input type="checkbox"/> |
| 187. U.S. Department of State | <input type="checkbox"/> |
| 188. U.S. Department of Defense | <input type="checkbox"/> |
| 189. U.S. Department of the Treasury | <input type="checkbox"/> |
| 190. U.S. Department of the Environment | <input type="checkbox"/> |
| 191. U.S. Department of the Interior | <input type="checkbox"/> |
| 192. U.S. Department of Energy | <input type="checkbox"/> |
| 193. U.S. Department of Transportation | <input type="checkbox"/> |
| 194. U.S. Department of Commerce | <input type="checkbox"/> |
| 195. U.S. Department of Labor | <input type="checkbox"/> |
| 196. U.S. Department of Housing & Urban Development | <input type="checkbox"/> |
| 197. U.S. Department of Social Services | <input type="checkbox"/> |
| 198. U.S. Department of Veterans Affairs | <input type="checkbox"/> |
| 199. U.S. Department of State | <input type="checkbox"/> |
| 200. U.S. Department of Defense | <input type="checkbox"/> |
| 201. U.S. Department of the Treasury | <input type="checkbox"/> |
| 202. U.S. Department of the Environment | <input type="checkbox"/> |
| 203. U.S. Department of the Interior | <input type="checkbox"/> |
| 204. U.S. Department of Energy | <input type="checkbox"/> |
| 205. U.S. Department of Transportation | <input type="checkbox"/> |
| 206. U.S. Department of Commerce | <input type="checkbox"/> |
| 207. U.S. Department of Labor | <input type="checkbox"/> |
| 208. U.S. Department of Housing & Urban Development | <input type="checkbox"/> |
| 209. U.S. Department of Social Services | <input type="checkbox"/> |
| 210. U.S. Department of Veterans Affairs | <input type="checkbox"/> |
| 211. U.S. Department of State | <input type="checkbox"/> |
| 212. U.S. Department of Defense | <input type="checkbox"/> |
| 213. U.S. Department of the Treasury | <input type="checkbox"/> |
| 214. U.S. Department of the Environment | <input type="checkbox"/> |
| 215. U.S. Department of the Interior | <input type="checkbox"/> |
| 216. U.S. Department of Energy | <input type="checkbox"/> |
| 217. U.S. Department of Transportation | <input type="checkbox"/> |
| 218. U.S. Department of Commerce | <input type="checkbox"/> |
| 219. U.S. Department of Labor | <input type="checkbox"/> |
| 220. U.S. Department of Housing & Urban Development | <input type="checkbox"/> |
| 221. U.S. Department of Social Services | <input type="checkbox"/> |
| 222. U.S. Department of Veterans Affairs | <input type="checkbox"/> |
| 223. U.S. Department of State | <input type="checkbox"/> |
| 224. U.S. Department of Defense | <input type="checkbox"/> |
| 225. U.S. Department of the Treasury | <input type="checkbox"/> |
| 226. U.S. Department of the Environment | <input type="checkbox"/> |
| 227. U.S. Department of the Interior | <input type="checkbox"/> |
| 228. U.S. Department of Energy | <input type="checkbox"/> |
| 229. U.S. Department of Transportation | <input type="checkbox"/> |
| 230. U.S. Department of Commerce | <input type="checkbox"/> |
| 231. U.S. Department of Labor | <input type="checkbox"/> |
| 232. U.S. Department of Housing & Urban Development | <input type="checkbox"/> |
| 233. U.S. Department of Social Services | <input type="checkbox"/> |
| 234. U.S. Department of Veterans Affairs | <input type="checkbox"/> |
| 235. U.S. Department of State | <input type="checkbox"/> |
| 236. U.S. Department of Defense | <input type="checkbox"/> |
| 237. U.S. Department of the Treasury | <input type="checkbox"/> |
| 238. U.S. Department of the Environment | <input type="checkbox"/> |
| 239. U.S. Department of the Interior | <input type="checkbox"/> |
| 240. U.S. Department of Energy | <input type="checkbox"/> |
| 241. U.S. Department of Transportation | <input type="checkbox"/> |
| 242. U.S. Department of Commerce | <input type="checkbox"/> |
| 243. U.S. Department of Labor | <input type="checkbox"/> |
| 244. U.S. Department of Housing & Urban Development | <input type="checkbox"/> |
| 245. U.S. Department of Social Services | <input type="checkbox"/> |
| 246. U.S. Department of Veterans Affairs | <input type="checkbox"/> |
| 247. U.S. Department of State | <input type="checkbox"/> |
| 248. U.S. Department of Defense | <input type="checkbox"/> |
| 249. U.S. Department of the Treasury | <input type="checkbox"/> |
| 250. U.S. Department of the Environment | <input type="checkbox"/> |
| 251. U.S. Department of the Interior | <input type="checkbox"/> |
| 252. U.S. Department of Energy | <input type="checkbox"/> |
| 253. U.S. Department of Transportation | <input type="checkbox"/> |
| 254. U.S. Department of Commerce | <input type="checkbox"/> |
| 255. U.S. Department of Labor | <input type="checkbox"/> |
| 256. U.S. Department of Housing & Urban Development | <input type="checkbox"/> |
| 257. U.S. Department of Social Services | <input type="checkbox"/> |
| 258. U.S. Department of Veterans Affairs | <input type="checkbox"/> |
| 259. U.S. Department of State | <input type="checkbox"/> |
| 260. U.S. Department of Defense | <input type="checkbox"/> |
| 261. U.S. Department of the Treasury | <input type="checkbox"/> |
| 262. U.S. Department of the Environment | <input type="checkbox"/> |
| 263. U.S. Department of the Interior | <input type="checkbox"/> |
| 264. U.S. Department of Energy | <input type="checkbox"/> |
| 265. U.S. Department of Transportation | <input type="checkbox"/> |
| 266. U.S. Department of Commerce | <input type="checkbox"/> |
| 267. U.S. Department of Labor | <input type="checkbox"/> |
| 268. U.S. Department of Housing & Urban Development | <input type="checkbox"/> |
| 269. U.S. Department of Social Services | <input type="checkbox"/> |
| 270. U.S. Department of Veterans Affairs | <input type="checkbox"/> |
| 271. U.S. Department of State | <input type="checkbox"/> |
| 272. U.S. Department of Defense | <input type="checkbox"/> |
| 273. U.S. Department of the Treasury | <input type="checkbox"/> |
| 274. U.S. Department of the Environment | <input type="checkbox"/> |
| 275. U.S. Department of the Interior | <input type="checkbox"/> |
| 276. U.S. Department of Energy | <input type="checkbox"/> |
| 277. U.S. Department of Transportation | <input type="checkbox"/> |
| 278. U.S. Department of Commerce | <input type="checkbox"/> |
| 279. U.S. Department of Labor | <input type="checkbox"/> |
| 280. U.S. Department of Housing & Urban Development | <input type="checkbox"/> |
| 281. U.S. Department of Social Services | <input type="checkbox"/> |
| 282. U.S. Department of Veterans Affairs | <input type="checkbox"/> |
| 283. U.S. Department of State | <input type="checkbox"/> |
| 284. U.S. Department of Defense | <input type="checkbox"/> |
| 285. U.S. Department of the Treasury | <input type="checkbox"/> |
| 286. U.S. Department of the Environment | <input type="checkbox"/> |
| 287. U.S. Department of the Interior | <input type="checkbox"/> |
| 288. U.S. Department of Energy | <input type="checkbox"/> |
| 289. U.S. Department of Transportation | <input type="checkbox"/> |
| 290. U.S. Department of Commerce | <input type="checkbox"/> |
| 291. U.S. Department of Labor | <input type="checkbox"/> |
| 292. U.S. Department of Housing & Urban Development | <input type="checkbox"/> |
| 293. U.S. Department of Social Services | <input type="checkbox"/> |
| 294. U.S. Department of Veterans Affairs | <input type="checkbox"/> |
| 295. U.S. Department of State | <input type="checkbox"/> |
| 296. U.S. Department of Defense | <input type="checkbox"/> |
| 297. U.S. Department of the Treasury | <input type="checkbox"/> |
| 298. U.S. Department of the Environment | <input type="checkbox"/> |
| 299. U.S. Department of the Interior | <input type="checkbox"/> |
| 300. U.S. Department of Energy | <input type="checkbox"/> |
| 301. U.S. Department of Transportation | <input type="checkbox"/> |
| 302. U.S. Department of Commerce | <input type="checkbox"/> |
| 303. U.S. Department of Labor | <input type="checkbox"/> |
| 304. U.S. Department of Housing & Urban Development | <input type="checkbox"/> |
| 305. U.S. Department of Social Services | <input type="checkbox"/> |
| 306. U.S. Department of Veterans Affairs | <input type="checkbox"/> |
| 307. U.S. Department of State | <input type="checkbox"/> |
| 308. U.S. Department of Defense | <input type="checkbox"/> |
| 309. U.S. Department of the Treasury | <input type="checkbox"/> |
| 310. U.S. Department of the Environment | <input type="checkbox"/> |
| 311. U.S. Department of the Interior | <input type="checkbox"/> |
| 312. U.S. Department of Energy | <input type="checkbox"/> |
| 313. U.S. Department of Transportation | <input type="checkbox"/> |
| 314. U.S. Department of Commerce | <input type="checkbox"/> |
| 315. U.S. Department of Labor | <input type="checkbox"/> |
| 316. U.S. Department of Housing & Urban Development | <input type="checkbox"/> |
| 317. U.S. Department of Social Services | <input type="checkbox"/> |
| 318. U.S. Department of Veterans Affairs | <input type="checkbox"/> |
| 319. U.S. Department of State | <input type="checkbox"/> |
| 320. U.S. Department of Defense | <input type="checkbox"/> |
| 321. U.S. Department of the Treasury | <input type="checkbox"/> |
| 322. U.S. Department of the Environment | <input type="checkbox"/> |
| 323. U.S. Department of the Interior | <input type="checkbox"/> |
| 324. U.S. Department of Energy | <input type="checkbox"/> |
| 325. U.S. Department of Transportation | <input type="checkbox"/> |
| 326. U.S. Department of Commerce | <input type="checkbox"/> |
| 327. U.S. Department of Labor | <input type="checkbox"/> |
| 328. U.S. Department of Housing & Urban Development | <input type="checkbox"/> |
| 329. U.S. Department of Social Services | <input type="checkbox"/> |
| 330. U.S. Department of Veterans Affairs | <input type="checkbox"/> |
| 331. U.S. Department of State | <input type="checkbox"/> |
| 332. U.S. Department of Defense | <input type="checkbox"/> |
| 333. U.S. Department of the Treasury | <input type="checkbox"/> |
| 334. U.S. Department of the Environment | <input type="checkbox"/> |
| 335. U.S. Department of the Interior | <input type="checkbox"/> |
| 336. U.S. Department of Energy | <input type="checkbox"/> |
| 337. U.S. Department of Transportation | <input type="checkbox"/> |
| 338. U.S. Department of Commerce | <input type="checkbox"/> |
| 339. U.S. Department of Labor | <input type="checkbox"/> |
| 340. U.S. Department of Housing & Urban Development | <input type="checkbox"/> |
| 341. U.S. Department of Social Services | <input type="checkbox"/> |
| 342. U.S. Department of Veterans Affairs | <input type="checkbox"/> |
| 343. U.S. Department of State | <input type="checkbox"/> |
| 344. U.S. Department of Defense | <input type="checkbox"/> |
| 345. U.S. Department of the Treasury | <input type="checkbox"/> |
| 346. U.S. Department of the Environment | <input type="checkbox"/> |
| 347. U.S. Department of the Interior | <input type="checkbox"/> |
| 348. U.S. Department of Energy | <input type="checkbox"/> |
| 349. U.S. Department of Transportation | <input type="checkbox"/> |
| 350. U.S. Department of Commerce | <input type="checkbox"/> |
| 351. U.S. Department of Labor | <input type="checkbox"/> |
| 352. U.S. Department of Housing & Urban Development | <input type="checkbox"/> |
| 353. U.S. Department of Social Services | <input type="checkbox"/> |
| 354. U.S. Department of Veterans Affairs | <input type="checkbox"/> |
| 355. U.S. Department of State | <input type="checkbox"/> |
| 356. U.S. Department of Defense | <input type="checkbox"/> |
| 357. U.S. Department of the Treasury | <input type="checkbox"/> |
| 358. U.S. Department of the Environment | <input type="checkbox"/> |
| 359. U.S. Department of the Interior | <input type="checkbox"/> |
| 360. U.S. Department of Energy | <input type="checkbox"/> |
| 361. U.S. Department of Transportation | <input type="checkbox"/> |
| 362. U.S. Department of Commerce | <input type="checkbox"/> |
| 363. U.S. Department of Labor | <input type="checkbox"/> |
| 364. U.S. Department of Housing & Urban Development | <input type="checkbox"/> |
| 365. U.S. Department of Social Services | <input type="checkbox"/> |
| 366. U.S. Department of Veterans Affairs | <input type="checkbox"/> |
| 367. U.S. Department of State | <input type="checkbox"/> |
| 368. U.S. Department of Defense | <input type="checkbox"/> |
| 369. U.S. Department of the Treasury | <input type="checkbox"/> |
| 370. U.S. Department of the Environment | <input type="checkbox"/> |
| 371. U.S. Department of the Interior | <input type="checkbox"/> |
| 372. U.S. Department of Energy | <input type="checkbox"/> |
| 373. U.S. Department of Transportation | <input type="checkbox"/> |
| 374. U.S. Department of Commerce | <input type="checkbox"/> |
| 375. U.S. Department of Labor | <input type="checkbox"/> |
| 376. U.S. Department of Housing & Urban Development | <input type="checkbox"/> |
| 377. U.S. Department of Social Services | <input type="checkbox"/> |
| 378. U.S. Department of Veterans Affairs | <input type="checkbox"/> |
| 379. U.S. Department of State | <input type="checkbox"/> |
| 380. U.S. Department of Defense | <input type="checkbox"/> |
| 381. U.S. Department of the Treasury | <input type="checkbox"/> |
| 382. U.S. Department of the Environment | <input type="checkbox"/> |
| 383. U.S. Department of the Interior | <input type="checkbox"/> |
| 384. U.S. Department of Energy | <input type="checkbox"/> |
| 385. U.S. Department of Transportation | <input type="checkbox"/> |
| 386. U.S. Department of Commerce | <input type="checkbox"/> |
| 387. U.S. Department of Labor | <input type="checkbox"/> |
| 388. U.S. Department of Housing & Urban Development | <input type="checkbox"/> |
| 389. U.S. Department of Social Services | <input type="checkbox"/> |
| 390. U.S. Department of Veterans Affairs | <input type="checkbox"/> |
| 391. U.S. Department of State | <input type="checkbox"/> |
| 392. U.S. Department of Defense | <input type="checkbox"/> |
| 393. U.S. Department of the Treasury | <input type="checkbox"/> |
| 394. U.S. Department of the Environment | <input type="checkbox"/> |
| 395. U.S. Department of the Interior | <input type="checkbox"/> |
| 396. U.S. Department of Energy | <input type="checkbox"/> |
| 397. U.S. Department of Transportation | <input type="checkbox"/> |
| 398. U.S. Department of Commerce | <input type="checkbox"/> |
| 399. U.S. Department of Labor | <input type="checkbox"/> |
| 400. U.S. Department of Housing & Urban Development | <input type="checkbox"/> |
| 401. U.S. Department of Social Services | <input type="checkbox"/> |
| 402. U.S. Department of Veterans Affairs | <input type="checkbox"/> |
| 403. U.S. Department of State | <input type="checkbox"/> |
| 404. U.S. Department of Defense | <input type="checkbox"/> |
| 405. U.S. Department of the Treasury | <input type="checkbox"/> |
| 406. U.S. Department of the Environment | <input type="checkbox"/> |
| 407. U.S. Department of the Interior | <input type="checkbox"/> |
| 408. U.S. Department of Energy | <input type="checkbox"/> |
| 409. U.S. Department of Transportation | <input type="checkbox"/> |
| 410. U.S. Department of Commerce | <input type="checkbox"/> |
| 411. U.S. Department of Labor | <input type="checkbox"/> |
| 412. U.S. Department of Housing & Urban Development | <input type="checkbox"/> |
| 413. U.S. Department of Social Services | <input type="checkbox"/> |
| 414. U.S. Department of Veterans Affairs | <input type="checkbox"/> |
| 415. U.S. Department of State | <input type="checkbox"/> |
| 416. U.S. Department of Defense | <input type="checkbox"/> |
| 417. U.S. Department of the Treasury | <input type="checkbox"/> |
| 418. U.S. Department of the Environment | <input type="checkbox"/> |
| 419. U.S. Department of the Interior | <input type="checkbox"/> |
| 420. U.S. Department of Energy | |

TABLE OF CONTENTS

| Chapter | | Page |
|----------|--|------|
| I | INTRODUCTION. | 1 |
| II | METHOD OF SOLUTION. | 7 |
| | A. Formulation of the Radiation Integral | 7 |
| | B. Approximation for the Surface Currents on the Impedance Patch | 13 |
| | C. Numerical Evaluation of the Surface Currents on the Impedance patch | 25 |
| III | RELIABILITY OF THE SURFACE CURRENT INTEGRATION METHOD (SCIM). | 30 |
| IV | RELATION OF RADIATION PATTERN PROPERTIES TO THE PERTINENT PARAMETERS OF THE PROBLEM. | 58 |
| V | CONCLUSIONS. | 80 |
| Appendix | | |
| A | AN ANALYSIS OF THE RADIATION FROM LINE SOURCES ON AN INFINITE PLANAR IMPEDANCE SURFACE. | 83 |
| | I. TE_z or Magnetic Line Source Excitation Case | 84 |
| | a. z Saddle Point Approximation | 86 |
| | b. Asymptotic Evaluation of the Perturbation Green's Function Representation | 89 |
| | II. TM_z or Magnetic Line Dipole Source Excitation Case | 92 |
| | a. Saddle Point Approximation | 94 |
| | b. Asymptotic Evaluation of the Perturbation Green's Function Representation | 95 |
| B | AN ANALYSIS OF THE RADIATION FROM LINE SOURCES ON A CIRCULAR CYLINDER COMPLETELY COVERED WITH AN IMPEDANCE SURFACE | 99 |
| | I. TE_z or Magnetic Line Source Excitaiton Case | 99 |
| | a. z Debye Approximation | 102 |
| | b. Watson Approximation | 105 |
| | c. Creeping Wave Formulation | 108 |
| | II. TM_z or Magnetic Line Dipole Source Excitation Case | 109 |
| | a. Debye Approximation | 113 |
| | b. Watson Approximation | 116 |
| | c. Creeping Wave Formulation | 118 |
| | REFERENCES. | 120 |

EVALUATION

This is the final report on Contract F19628-77-C-0107. It covers research and experiments performed during the period 6 January 1977 to 5 January 1979. The objective of the work was to increase the radiation intensity near the horizon of a magnetic line source, or a magnetic line dipole, located on a uniform impedance surface patch which partly covers an electrically large perfectly conducting convex cylinder. Various methods for analyzing and computing the radiation patterns of such magnetic sources are described and the near and far fields can be predicted fairly well.



NICHOLAS P. KERNWEIS
Project Engineer

CHAPTER I INTRODUCTION

An approximate, asymptotic high frequency analysis of the radiation patterns is presented for a two-dimensional (2-D) magnetic line source or a magnetic line dipole source located on a uniform impedance surface patch which partly covers an electrically large, perfectly conducting convex cylinder as in Figure 1. The purpose of this work is to assess the effects of such an impedance loading on the radiation patterns with a view towards being able to increase the pattern level in the vicinity of the horizon. The latter application is of interest in the design of a crossed-slot type fuselage mounted airborne antenna for satellite communication purposes. On a large, perfectly conducting convex cylinder, a circumferential slot typically radiates a field at the horizon (or shadow boundary) which is roughly 20 dB below that of an axial slot. In the crossed slot application, it is therefore desirable to enhance the fields of a circumferential slot near the horizon by impedance loading, while at the same time not significantly degrading the performance of the axial slot in the crossed slot antenna configuration.

In the present method of analysis, the impedance surface is represented by an equivalent aperture in an otherwise perfectly conducting convex cylinder. Approximate, asymptotic expressions for the "equivalent-aperture distribution" corresponding to the surface currents excited by a source on the impedance patch are developed for both the magnetic line source and the magnetic line dipole cases. A magnetic line source simulates a thin axial slot; whereas, a magnetic line dipole simulates a thin circumferential type slot. The asymptotic expressions obtained for the surface currents on the impedance patch remain valid in the vicinity of the source at Q' . The radiation pattern of the configuration in Figure 1 is then found in a straightforward fashion by numerically integrating this current distribution in conjunction with an accurate, asymptotic form of the perfectly conducting, convex cylinder Green's function as given by Pathak and Kouyoumjian[1]; a slightly improved version of this Green's function also appears in a report by Pathak and Huang[2]. As a result of employing this special cylinder Green's function rather than the usual free space Green's function, one needs to integrate the currents only over

the impedance surface patch. This method of analysis will be referred to as the surface current integration method (SCIM). Radiation pattern calculations based on this SCIM are found to compare quite well with those obtained via a numerical moment method type solution, a previous GTD solution for those impedances which support an Elliot mode, and also with some presently available experimental results. A moderately large increase in the radiation intensity can be obtained in the vicinity of the horizon for cylinders loaded by an impedance surface which support Elliot type modes[3]. An Elliot mode field is one which propagates on a curved impedance boundary with negligible leakage, and is therefore usually the dominant contributor to the field on such a surface; furthermore, as the curvature of the surface vanishes, it reduces to the usual "bound" surface wave mode on a planar impedance surface. It is noted that an Elliot mode can be excited by a magnetic line source if the surface impedance is inductive; whereas, it can be excited by a magnetic line dipole source if the surface impedance is capacitive.

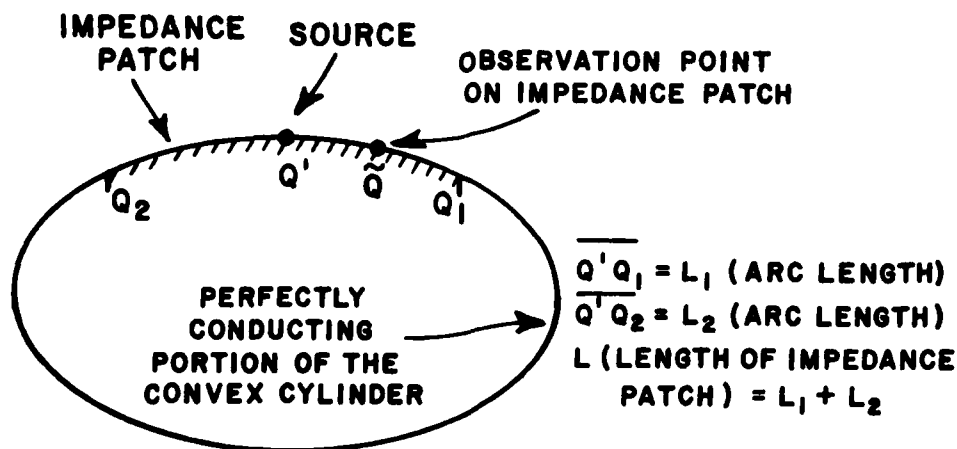


Figure 1--An illustration of an antenna on a perfectly conducting convex cylinder which is partly covered by an impedance patch.

This present work represents an important extension and generalization of some of the earlier work [2,4,5]. The earlier approach by Pathak [4] which led to a preliminary, asymptotic solution, for this problem could be designated as the diffraction coefficient or the geometrical theory of diffraction approach (GTD). A second approach presented by Pathak and Huang [2] which is based on the numerical solution of the integral equation for this problem is

designated as the MM-GTD approach [2]. This numerical solution was based on the moment method with some important simplifications resulting from the use of uniform and accurate GTD approximations for the excitation and the kernel of the integral equation. This MM-GTD solution [2] is employed primarily as an independent check on the GTD solution [4]; it also serves as a check on the SCIM solution. The MM-GTD solution in [2], which employs the cylinder surface Green's function as a kernel, is rather well suited for the TE case. However, one needs to be careful in employing it to the TM case because the kernel is far more singular than for the TE case, and it then appears to be necessary to properly incorporate the edge conditions on the fields at Q_1 and Q_2 in order to obtain a completely stable numerical result. While some initial success has been obtained for the TM case, further work is necessary to complete the MM-GTD treatment more satisfactorily for this case. Preliminary modifications and extensions of this work in [2] and [4] were reported later by Pathak and Ersoy [5] in which the SCIM procedure was outlined and a study of the asymptotic approximations for the surface currents to be employed in this SCIM procedure was initiated.

The work based on the GTD approach in [4] is an extension of the GTD solution of Hwang, Kouyoumjian and Pathak [6] for analyzing the radiation by a magnetic line source on a perfectly conducting box that is partly covered by a finite dielectric panel (over the face on which the source is located). In contrast to the work of Hwang et al. [6], a GTD analysis of the curved geometry in Figure 1 requires the solutions to more and different canonical problems, because of the complexity introduced into the analysis by the presence of the curvature. In this context, it is noted that the GTD solutions including the one in [1] and [4] are based on the local properties of wave propagation and diffraction at high frequencies, and can hence be "built up" from the asymptotic solutions to appropriate canonical problems which accurately model the local regions from where excitations or diffractions of the fields take place. For example, the field at a far zone observation point which is generated by the source at Q' is obtained by summing up the fields which propagate along the direct ray path, from the source to the field point as well as along the various diffracted ray paths such as those emanating from the ends of the patches at Q_1 and Q_2 , and also those that are shed tangentially after creeping around the back of the cylinder upon being launched from Q_1 and Q_2 . The ray picture of the GTD as illustrated in Figure 2 is physically appealing as it provides an insight into the nature of the radiation and diffraction mechanisms. The GTD analysis [4] was restricted to an impedance surface which would support an Elliot mode and for which this mode alone would be the dominant contributor to the fields diffracted from the edges of the impedance patch at Q_1 and Q_2 . The other component of the surface field (i.e., besides the Elliot mode field) diffracts not only from the edges

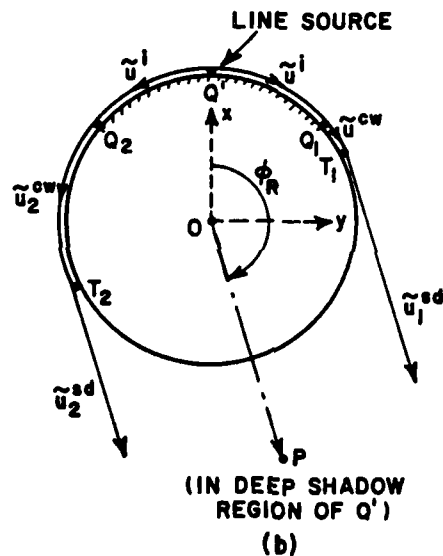
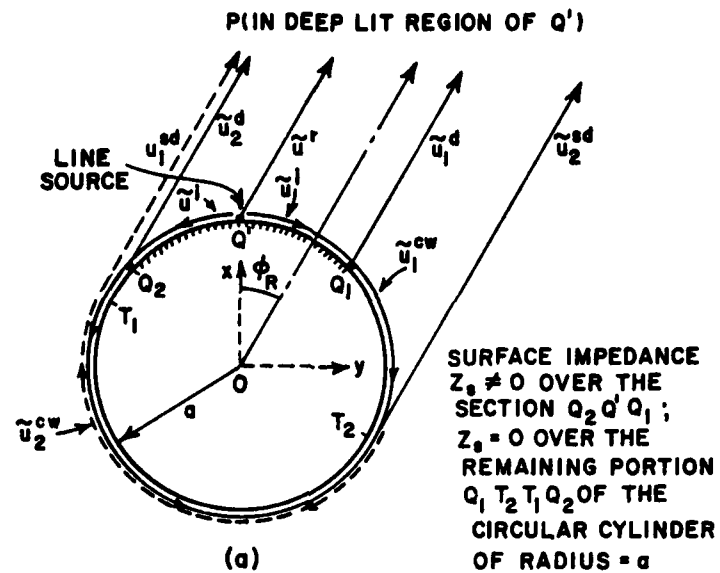


Figure 2--Rays and shadow boundaries associated with the GTD solution of [4].

of the impedance patch but also from the impedance surface via a continual leakage along the ray propagation path from Q' to Q_1 or Q_2 . If this leakage is significant, then the diffraction from just the Elliot mode may not provide a sufficiently accurate radiation pattern near the horizon. One expects this leakage effect, which is partly governed by the type of impedance, to become important as the cylinder size decreases. Furthermore, if the type of impedance chosen does not support an Elliot mode field, then this other field component is all that is left. For the latter case, the GTD analysis of [4] must be substantially modified to obtain a uniform diffraction coefficient for the diffraction from the edges of the patch, of this component of the field which continually leaks (or sheds) energy from the impedance surface. A uniform asymptotic solution of an appropriate canonical problem which would lead to such a uniform diffraction coefficient is somewhat complicated and is not attempted at the present time. The GTD technique presented in [4] is thus useful for sufficiently large cylinders with a sufficiently long impedance patch on which an Elliot mode can establish itself. It is noted that a pure Elliot mode is established beyond a certain minimum launching distance on the impedance patch. For more general situations; namely, for the case when the cylinders are only moderately large and for impedance surfaces which are not necessarily restricted to those that can support an Elliot mode field, the approach based on the SCIM appears to lead to a relatively simpler and sufficiently practical method of solution for the problem in Figure 1. Furthermore, this SCIM solution is constructed without essentially losing much of the physical insight provided by GTD solutions. Also, the SCIM can take into account impedance surface patches which are reasonably small; more will be said about this in Chapter III. It is noted that while the SCIM can handle more general situations than the previous GTD solution, it is also restricted at this time as is the latter solution to an impedance surface which is uniform (or at the most one which is very slowly varying if it is non-uniform). The MM-GTD procedure[2] can take non-uniform impedance into consideration quite easily; however, it does not provide the physical insight afforded by the SCIM.

It may be mentioned that Wait[7-12] has done considerable work on the asymptotic calculation of the surface fields which are diffracted past an impedance discontinuity as at Q_1 and Q_2 of Figure 1. Indeed, some of his work[7,9,12] has been helpful in the asymptotic analysis of the currents which exist on a curved impedance boundary. Nevertheless, Wait's results have not been directly applied here, as they do not furnish surface current representations which are suitable in the construction of an approximate solution based in particular on the SCIM. Additional comments comparing Wait's results with the ones developed here are presented in Section IIB. Also, Shapira, Felsen and Hessel[13,14] have analyzed the radiation from an active slot in an array of slots on

a perfectly conducting convex cylinder via asymptotic techniques; they employ a local periodic structure (LPS) model in which the array is viewed as an effective surface impedance. They also include the edge effects arising from finiteness of the array. It is noted that the surface fields obtained in the LPS method of [13] is not valid in the close neighborhood of the source; whereas, in the SCIM, it is important to obtain a surface field representation which remains valid in the source region as is done in this work. Furthermore the radiated field in the LPS method of [13] is not as easily obtained in the vicinity of the horizon as it is with the SCIM.

The organization of this dissertation is as follows. Chapter II describes the method of solution based on SCIM. The starting point of this solution is a generalized reaction formulation of the problem which leads to an integral representation for the fields radiated by the configuration in Figure 1. This integral representation is obtained in terms of the surface fields on an equivalent aperture corresponding to the extent of the impedance surface patch. The approximate, asymptotic expressions developed in here for these surface fields over the impedance patch are also indicated in that chapter together with a brief description on the final steps involving the integration of these surface fields to obtain the radiated fields. Chapter III discusses the accuracy of the solution obtained via SCIM. Numerical results illustrating the effect of different values of impedances and cylinder sizes on the radiation patterns of a magnetic line source or a magnetic line dipole source at Q' are presented in Chapter IV. The major conclusions of this work are presented in Chapter V. Analytical details pertaining to the development of the present SCIM solution are outlined in several appendices.

CHAPTER II

METHOD OF SOLUTION

The method of solution employed here for treating the radiation problem depicted in Figure 1 is discussed in this chapter. As pointed out earlier, in this solution based on the SCIM, the impedance surface patch is viewed as an equivalent aperture in the rest of the perfectly conducting convex cylinder. The field radiated by this configuration is then expressed in terms of an integral just over the surface current distribution which exists on the aperture (or the impedance surface patch) because one employs an asymptotic high frequency form of the perfectly conducting convex cylinder Green's function in this radiation integral. The formulation of this radiation integral over the equivalent current distribution in the aperture is discussed in part A of this chapter. The surface current distribution on the impedance patch, which is produced by the source at Q' is approximately found from the asymptotic solutions to two auxiliary canonical problems. The solutions to these auxiliary canonical problems and the form of the surface currents on the impedance patch are discussed in part B. The final step in the solution involves incorporating the surface currents found from part B into the radiation integral of part A, and then evaluating this integral to obtain the radiated field. The latter integration is performed efficiently and in a straightforward manner via standard numerical techniques, as discussed in part C. In the following analysis, an $e^{j\omega t}$ time dependence will be assumed and suppressed.

A. Formulation of the Radiation Integral

The pertinent radiation integral may be obtained in several different ways. The procedure by which this radiation integral is obtained in the present work is based on a generalization of the reaction theorem[15,16]. The same radiation integral could also be obtained via an application of the scalar Green's theorem (since the problem considered here is two-dimensional), or the dyadic Green's theorem (and its specialization to the two-dimensional vector problem considered here), or an application of the compensation theorem for electromagnetic fields[17]. In the methods based on the Green's theorems, an appropriate Green's function which satisfies the boundary conditions for a perfectly conducting convex cylinder must be employed. The generalized reaction theorem which is employed here for formulating the radiation integral is somewhat related to the other methods mentioned above; it is chosen

as it allows one to treat both, the TE_z and the TM_z cases simultaneously for this vector problem.

Consider the integral expressions relating the electric and magnetic fields (\vec{E}_b, \vec{H}_b) generated by a magnetic current source \vec{M} at P which radiates in the presence of the actual or perturbed geometry of Figure 3, to the fields (\vec{E}_0, \vec{H}_0) generated by a test source \vec{T} at P' which radiates in the presence of the unperturbed geometry of the same figure. This integral relationship indicated below in (8) is obtained in a manner similar to that done in a previous report[5]. Here, the perturbed problem refers to a closed, perfectly-conducting surface partly covered with an impedance surface patch; whereas, the unperturbed problem refers to the same perfectly-conducting surface without the impedance surface patch.

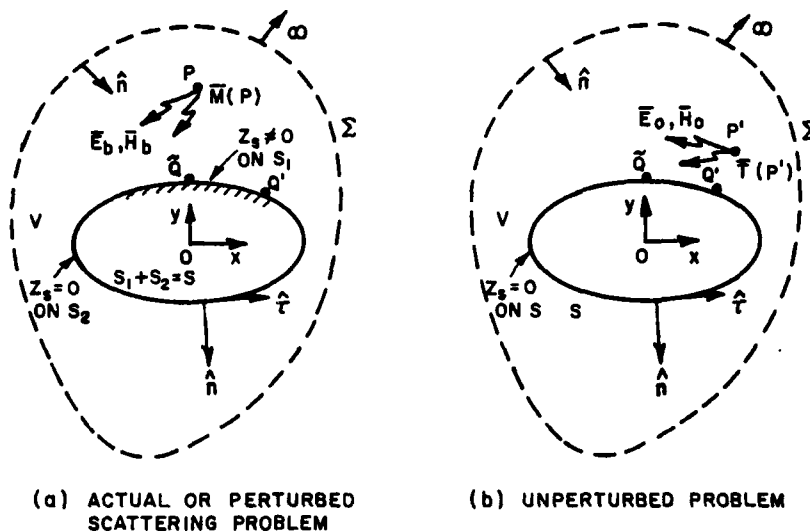


Figure 3--The actual scattering problem, and the related unperturbed problem.

In the case of the unperturbed problem, the test source, \vec{T} is assumed to be either an electric line source in which case the fields generated by this source will be denoted by $(\vec{E}_0^e, \vec{H}_0^e)$, or \vec{T} is a magnetic line source, generating fields which are denoted by $(\vec{E}_0^m, \vec{H}_0^m)$. The following analysis will reveal that, the fields $(\vec{E}_0^e, \vec{H}_0^e)$ can be related to the fields (\vec{E}_b, \vec{H}_b) for the case when \vec{M} is a magnetic line dipole source, i.e., for the TM_z -case; likewise the fields $(\vec{E}_0^m, \vec{H}_0^m)$ can be related to the fields (\vec{E}_b, \vec{H}_b) for the case when \vec{M} is a magnetic line source, i.e., for the TE_z -case. From Maxwell's equations, one obtains

$$\nabla \times \vec{E}_0^e = -jkZ_0 \vec{H}_0^e; \quad \nabla \times \vec{H}_0^e = jkY_0 \vec{E}_0^e + \vec{J}_T; \quad \text{if } T=J_T \quad (1a,b)$$

and

$$\nabla \times \vec{E}_0^m = -jkZ_0 \vec{H}_0^m - \vec{M}_T; \quad \nabla \times \vec{H}_0^m = jkY_0 \vec{E}_0^m; \quad \text{if } T=M_T \quad (2a,b)$$

Furthermore, (\vec{E}_0, \vec{H}_0) satisfy the radiation condition over the surface Σ at infinity, and \vec{E}_0 satisfies the following boundary conditions on the surface s ;

$$\hat{n} \times \vec{E}_0^{e,m} = 0, \quad \text{on } s. \quad (3)$$

In (1) and (2) k is the free space wavenumber, and $Z_0=1/Y_0$ is the free space impedance (i.e., $Z_0=120 \pi$ ohms).

The fields, \vec{E}_b, \vec{H}_b of the perturbed problem also satisfy the Maxwell's equations

$$\nabla \times \vec{E}_b = -jkZ_0 \vec{H}_b - \vec{M}; \quad \nabla \times \vec{H}_b = jkY_0 \vec{E}_b \quad (4a,b)$$

and the radiation condition over the surface Σ at infinity. Also \vec{E}_b and \vec{H}_b satisfy the following boundary conditions on s :

$$\vec{E}_b - (\hat{n} \cdot \vec{E}_b) \hat{n} = Z_s \hat{n} \times \vec{H}_b \quad \left. \begin{array}{l} \text{on } s_1 \\ \\ \text{on } s_2 \end{array} \right\} \quad s=s_1+s_2 \quad (5a)$$

$$\hat{n} \times \vec{E}_b = 0 \quad \left. \begin{array}{l} \text{on } s_1 \\ \\ \text{on } s_2 \end{array} \right\} \quad (5b)$$

where Z_s denotes the value of the surface impedance in the perturbed problem.

Combination of (2), (4) and (1), (4) respectively yields

$$\nabla \cdot [\vec{E}_0^m \times \vec{H}_b - \vec{E}_b \times \vec{H}_0^m] = \vec{M} \cdot \vec{H}_0^m - \vec{M}_T \cdot \vec{H}_b; \quad TE_z\text{-case} \quad (6)$$

and

$$\nabla \cdot [\vec{E}_0^e \times \vec{H}_b - \vec{E}_b \times \vec{H}_0^e] = \vec{M} \cdot \vec{H}_0^e + \vec{J}_T \cdot \vec{E}_b; \quad TM_z\text{-case} \quad (7)$$

Applying the divergence theorem to (6) and (7) and using the radiation condition on Σ , and the boundary conditions (3) and (5) yields:

$$\int_{s_1}^e ds \bar{H}_0^m(\tilde{Q}|P') \cdot [Z_s(\tilde{Q}) \hat{n} \times \hat{n} \times \bar{H}_b(\tilde{Q}|P)] =$$

$$\left\{ \begin{array}{l} \iiint_V dv [\bar{H}_0^e(P|P') \cdot \bar{M}(P) + \bar{E}_b(P'|P) \cdot \bar{T}(P')] , \\ \text{if } T = J_t \\ \\ \iiint_V dv [\bar{H}_0^m(P|P') \cdot \bar{M}(P) - \bar{H}_b(P'|P) \cdot \bar{T}(P')] , \\ \text{if } T = M_t \end{array} \right. \quad (8)$$

The volume v is enclosed between the closed surfaces $s=s_1+s_2$ and Σ (which recedes to infinity). The notation of the type $(A|B)$ in the argument of the field functions $\bar{H}_0^{e,m}$ and (\bar{E}_b, \bar{H}_b) is introduced for convenience, and it refers to the field at A due to source at B . Specializing the above equations to the two-dimensional field and source configurations (i.e., configurations which are uniform in the \hat{z} -direction), one obtains

$$\int_{s_1}^e d\ell \bar{H}_0^m(\tilde{Q}|P') \cdot [Z_s(\tilde{Q}) \hat{n} \times \hat{n} \times \bar{H}_b(\tilde{Q}|P)] =$$

$$\left\{ \begin{array}{l} \iint_{s_M} dx dy \bar{H}_0^e(P|P') \cdot \bar{M}(P) + \iint_{s_T} dx dy \bar{E}_b(P'|P) \cdot \bar{T}(P') \\ \text{if } T = J_t, \\ \\ \iint_{s_M} dx dy \bar{H}_0^m(P|P') \cdot \bar{M}(P) - \iint_{s_T} dx dy \bar{H}_b(P'|P) \cdot \bar{T}(P') \\ \text{if } T = M_t. \end{array} \right. \quad (9)$$

The regions s_M and s_T are the cross-sectional areas of the 2-D source distribution \bar{M} and \bar{T} , respectively. Also, ds in (8) is given as $ds = d\ell dz > 0$ with $dz > 0$; hence, the 2-D arc length integral on the boundary s , (LHS of (9)) is chosen to proceed in the direction for which $d\ell$ increases in the positive sense. Let the 2-D sources \bar{M} and \bar{T} be

$$\bar{M} = \hat{m} \delta(\bar{\rho} - \bar{\rho}_p) \quad (10a)$$

$$T = \begin{cases} \int_t \delta(\bar{\rho} - \bar{\rho}_{P'}) , & \text{if } T = J_t \\ \hat{m}_t \delta(\bar{\rho} - \bar{\rho}_{P'}) , & \text{if } T = M_t \end{cases} \quad (10b)$$

Let the point P' in (9) recede to infinity; whereas, the point P is moved down to the point Q' on the surface. Thus,

$$\int_{s_1} d\ell H_0^e(\tilde{Q}|P') \cdot [Z_s(\tilde{Q}) \hat{n} \times \hat{n} \times H_b(\tilde{Q}|Q')] = H_0^e(Q'|P') \cdot \hat{m} \cdot E_b(P'|Q') \cdot \hat{j}_t$$

for the TM_z case with $\hat{m} = \hat{z} M_d$ and $\hat{j}_t = \hat{z}$ (11a)

$$\int_{s_1} d\ell H_0^m(\tilde{Q}|P') \cdot [Z_s(\tilde{Q}) \hat{n} \times \hat{n} \times H_b(\tilde{Q}|Q')] = H_0^m(Q'|P') \cdot \hat{m} \cdot H_b(P'|Q') \cdot \hat{m}_t$$

for the TE_z case with $\hat{m} = \hat{z} M$ and $\hat{m}_t = \hat{z}$. (11b)

The $E_b(P'|Q')$ in the TM_z problem pertaining to (11a) is the electric field which is produced at P' (in the far zone) by a unit strength tangential magnetic line dipole source at Q' on the surface s_1 ; whereas, $H_b(P'|Q')$ is the magnetic field in the TE_z problem in (11b) which is produced at P' (in far zone) by a unit strength magnetic line source at Q' on the surface s_1 . $H_0^e(Q'$ or $\tilde{Q}|P')$ and $H_0^m(Q'$ or $\tilde{Q}|P')$ are the magnetic fields induced at Q' or \tilde{Q} on the unperturbed surface s of Figure 3 due to a test source T at P' in the far zone. In the case of H_0^e , the test source is an electric line source; whereas, for H_0^m , the test source is a magnetic line source. The expressions for $H_0^{e,m}$ are available in [1,2] in terms of the GTD approximation which will be employed here. The GTD approximation is valid for electrically large cylinders; the latter is assumed to be valid in the present analysis. Thus, the E_b and H_b on RHS of (11a) and (11b) may be found if $\hat{n} \times H_b(\tilde{Q}|Q')$ inside the integrals on the LHS of (11a;b) are known. The field $\hat{n} \times H_b(\tilde{Q}|Q')$ is the tangential magnetic field at \tilde{Q} on the surface s_1 of Figure 3 due to a source at Q' also on s_1 . In the TM_z case, the source at Q' is a tangential magnetic line dipole; whereas, in the TE_z case, the source is a magnetic line source as mentioned earlier.

An alternative expression for $E_b(P'|Q')$ for the TM_z -case of (11a) can be expressed in terms of electric field quantities alone via

$$\vec{H}_0^e(Q'|P') \cdot \hat{m} = -\vec{E}_0^m(P'|Q') \cdot \hat{j}_t \quad \text{with } \hat{j}_t = \hat{z} \quad (12)$$

as follows:

$$\vec{E}_b(P'|Q') \cdot \hat{z} = \vec{E}_0^m(P'|Q') \cdot \hat{z} + \frac{1}{M_d} \int_{s_1} d\ell [\vec{E}_0^m(P'|\vec{Q}) \cdot \hat{z}] \cdot [\vec{E}_b(\vec{Q}|Q') \cdot \hat{z}] \quad (13)$$

Furthermore, it is shown below in section B that the unknown $\vec{E}_b(\vec{Q}|Q')$ can be expressed as

$$\vec{E}_b(\vec{Q}|Q') \cdot \hat{z} = -M_d \delta(\vec{Q}|Q') + \vec{E}_b(\vec{Q}^+|Q') \cdot \hat{z} \quad (14)$$

In (14), $\vec{E}_b(\vec{Q}|Q') \cdot \hat{z}$ is the tangential electric field of the magnetic line dipole source, $\vec{M} = \hat{z} M_d \delta(\vec{\rho} - \vec{\rho}_0)$, and it is observed on the surface s_1 which lies "just underneath" the magnetic line dipole source; whereas, $\vec{E}_b(\vec{Q}^+|Q') \cdot \hat{z}$ is the tangential electric field of the same source, and this field is observed on a surface s_1^+ which lies "just above" the magnetic line dipole source. Here \vec{Q}^+ must be interpreted as $\vec{Q}^+ = \lim_{\epsilon \rightarrow 0} (\vec{\rho} = \vec{\rho}' + \epsilon; \phi)$ where $Q' = (\rho', \phi')$ and ϵ is

a positive number. Explicit expressions for the electric field $\vec{E}_b(Q|Q')$ and $\vec{E}_b(Q^+|Q')$ of (14) are given in Appendix B. Equation (14) is a well known expression for the discontinuity of the tangential electric field as one moves from the surface s_1 to the surface s_1^+ across a magnetic current.

When (14) is incorporated into (13), a further simplification results so that the final form of $\vec{E}_b(P'|Q')$ becomes

$$\vec{E}_b(P'|Q') = \frac{1}{M_d} \int_{s_1^+} d\ell [\vec{E}_0^m(P'|\vec{Q}) \cdot \hat{z}] [\vec{E}_b(\vec{Q}^+|Q') \cdot \hat{z}] \quad (15)$$

In (15) it is noted that the integral is performed on the surface s_1^+ "just above" the line dipole source.

The importance of introducing (15) will become evident in section (C) where it is pointed out that the expression for the unknown $\vec{E}_b(\vec{Q}^+|Q')$ in the TM_z case is less complicated than the one for the unknown $\vec{H}_b(Q'|Q')$ of (11a) for the same TM_z case.

An approximation for the unknown $\hat{z} \cdot \hat{n} \times \hat{n} \times \vec{H}_b(\vec{Q}|Q')$ in (11a; 11b) will be introduced next together with an approximation for $\vec{z} \cdot \vec{E}_b(\vec{Q}^+|Q')$.

B. Approximation for the Surface Currents on the Impedance Patch

The current $Z_s \hat{n} \times \hat{n} \times \vec{H}_b(\vec{Q}|\vec{Q}')$ of (11) which exists on the finite length impedance surface patch s_1 may be expressed as

$$Z_s \hat{n} \times \hat{n} \times \vec{H}_b(\vec{Q}|\vec{Q}') = -jKY_0 Z_s \begin{Bmatrix} -M\hat{z} \\ -M_d \hat{\tau} \end{Bmatrix} \begin{bmatrix} h & h \\ G^S & + G_R^S \end{bmatrix}, \text{ for the } \begin{cases} TE_z \text{ case} \\ TM_z \text{ case} \end{cases} \quad (16a)$$

and similarly the current $\vec{E}_b(\vec{Q}^+|\vec{Q}') \cdot \hat{z} (= \hat{\tau} \cdot \hat{n} \times \vec{E}_b(\vec{Q}^+|\vec{Q}'))$ of (15) which exists on the impedance surface patch s_1^+ is,

$$\vec{E}_b(\vec{Q}^+|\vec{Q}') \cdot \hat{z} = -\alpha_s M_d [G^e(\vec{Q}^+|\vec{Q}') + G_R^e(\vec{Q}^+|\vec{Q}')] \text{ for the } TM_z\text{-case} \quad (16b)$$

where α_s is defined in (20c). M or M_d are the strengths of the magnetic line source or line dipole source at Q' for the TE_z or

TM_z case, respectively. The $-jKY_0 Z_s \begin{Bmatrix} -M\hat{z} \\ -M_d \hat{\tau} \end{Bmatrix} G^S$ refers to that

component of the current which would exist if the cylinder was completely covered by an impedance surface. The quantity

$-jKY_0 Z_s \begin{Bmatrix} -M\hat{z} \\ -M_d \hat{\tau} \end{Bmatrix} G_R^S$ is then viewed as the correction or perturbation to the current $-jKY_0 Z_s \begin{Bmatrix} -M\hat{z} \\ -M_d \hat{\tau} \end{Bmatrix} G^S$ which arises from the

truncation of the impedance surface at Q_1 and Q_2 . The term

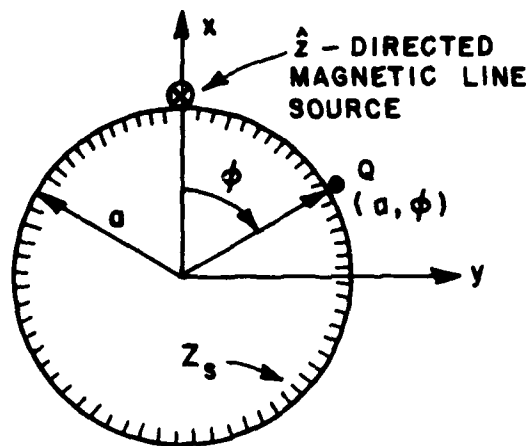
$-jKY_0 Z_s \begin{Bmatrix} -M\hat{z} \\ -M_d \hat{\tau} \end{Bmatrix} G_R^S$ thus refers to the component of the current which is reflected from the ends of the patch at Q_1 and Q_2 .

Explicit expressions for $G^e(\vec{Q}^+|\vec{Q}')$ is given in (B-44a) of Appendix B. A comparison of (B7) with (B-44a) reveals that, an asymptotic expansion for $G^e(\vec{Q}^+|\vec{Q}')$ can be obtained from the asymptotic expansion for G^h by simply changing α_h and β_h in the latter to α_s and β_s . The final form of G^h is given in (17a). The quantity $G_R^e(\vec{Q}^+|\vec{Q}')$ which is analogous to G_R^h arises from the fact that the impedance patch is of finite extent, and therefore there are reflections from the ends of the patch at Q_1 and Q_2 .

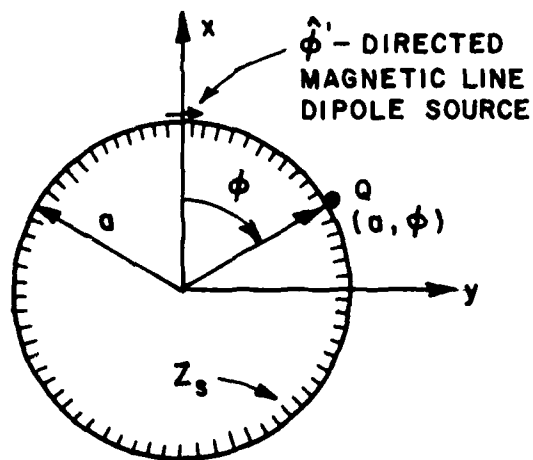
In particular the quantity $-jkY_0 Z_s \begin{Bmatrix} -M_z \\ -M_{\hat{r}} \end{Bmatrix} G^b$ may be explicitly found from the canonical problem of determining the surface fields of a magnetic line source or a magnetic line dipole on a circular cylinder which is completely covered with an impedance surface as in Figure 4. The radius of the cylinder is denoted by a . The points on the impedance patch are specified by the arc length $t(=a|\phi|)$ along the surface of the cylinder and it is measured from the source. In appendix B, an asymptotic approximation to G^b for the circular cylinder case is presented; this asymptotic approximation is valid for electrically large cylinders which are of interest in this study. While an exact circumferential eigenfunction (or modal) series expansion exists for G^b pertaining to the circular cylinder case, it is poorly convergent for large cylinders. Furthermore, this exact modal series representation for the circular case cannot be generalized to an arbitrary convex cylinder. In contrast, an asymptotic high frequency approximation for the G^b pertaining to a circular cylinder becomes increasingly accurate with an increase in the cylinder radius. Also, this asymptotic solution can be generalized rather easily via the local properties of high frequency field solutions to treat an arbitrary convex cylinder with a slowly varying curvature as in the geometrical theory of diffraction (GTD) procedure. The asymptotic approximation to G^b for the circular case is developed in sufficient detail in Appendix B; hence, only the final results are summarized below.

$$G^h \sim \begin{cases} \frac{1}{2j} H_0^{(2)}(kt) F_1^h(\xi) - j \frac{\alpha_h}{\beta_h} e^{-j\beta_h t} \epsilon_h - \frac{j\alpha_h}{k\sqrt{\pi}} e^{-jkt} Q(j\beta_h \sqrt{kt}) e^{-\tilde{b}_h^2 kt} \\ - \frac{jk^2}{4\alpha_h^2} \left[e^{-jkt} \left\{ \frac{1+jkt}{2} \frac{\alpha_h^2}{k^2} + 1 \right\} + 2 \left(1 - \alpha_h \frac{d}{d\alpha_h} \right) F_2^h(kt) \right] \frac{1}{2m^3} ; \\ t < \frac{1}{2} t_m \quad (17a) \\ -2\pi j \frac{e^{-jkt}}{4\pi m} \sum_{p=0}^{\infty} \frac{e^{-j\sigma_p \xi}}{\sigma_p + (\alpha_h k^{-1/m})^2} ; \quad t > \frac{1}{2} t_m \quad (17b) \end{cases}$$

and



(a) TE_z - CASE



(b) TM_z - CASE

Figure 4--Geometries of canonical problems of a line source on a circular cylinder covered completely by an impedance surface.

$$G^S \sim \begin{cases} \frac{1}{2j} \frac{H_1^{(2)}(kt)}{kt} F_1^S(\xi) - j \frac{\alpha_s^3}{k^2 \beta_s} e^{-j\beta_s t} \epsilon_s + \frac{2\alpha_s}{\beta_s} \delta(t) \epsilon_s - \frac{1}{2j} \left(1 + \frac{d^2}{d(kt)^2}\right) \\ \cdot [H_0^{(2)}(kt) \{1 - 2z e^{z^2} Q(z)\}] + \frac{jk}{2} \left(1 - \alpha_s \frac{d}{d\alpha_s}\right) F_2^S(kt) \frac{1}{2m^3}; & t < \frac{1}{2} t_m \quad (18a) \\ -2\pi j \frac{\alpha_s^2}{4\pi k^2 m} e^{-jkt} \sum_{p=0}^{\infty} \frac{e^{-j\sigma_p \xi}}{\sigma_p - (\alpha_s k^{-1} m)^2}; & t > \frac{1}{2} t_m \quad (18b) \end{cases}$$

where t_m is the maximum total impedance patch size beyond which the asymptotic representation of the currents in (17a) and (18a) cannot be trusted. An empirical equation for t_m is presented in Chapter III. Also, in (17)

$$F_1^h(\xi) = 1 - \frac{\sqrt{\pi j}}{4} \xi^{3/2} + \frac{j7}{60} \xi^3 + \frac{7\sqrt{-\pi j}}{512} \xi^{9/2} + \dots \quad (19a)$$

$$F_2^h(kt) = -\frac{k}{\beta_h} e^{-j\beta_h t} \epsilon_h + \frac{e^{-jkt}}{\sqrt{\pi}} Q(j\tilde{b}_h \sqrt{kt}) e^{-\tilde{b}_h^2 kt}; \quad \alpha_h \geq 0 \quad (19b)$$

$$t = a|\phi|; \quad \xi = m|\phi|; \quad m = \left(\frac{ka}{2}\right)^{1/3} \quad (19c, d, e)$$

$$\alpha_h = -jk \frac{Z_s}{Z_0}; \quad \beta_h = \sqrt{k^2 + \alpha_h^2} = 2\pi\lambda_h \quad (19f, g)$$

$$\tilde{b}_h = \frac{\alpha_h}{k} \sqrt{\frac{j}{2}}; \quad \alpha_h^- = -|\alpha_h|; \quad (19h, i)$$

$$\epsilon_h = \begin{Bmatrix} 1 \\ 0 \end{Bmatrix}, \quad \alpha_h \geq 0. \quad (19j)$$

σ_p are the roots of $w_2'(\sigma) - \alpha_m k^{-1} w_2(\sigma) = 0$ where $w_2(\sigma) = \pi[Bi(\sigma) - jAi(\sigma)]$ is the Fock-type Airy² function. The prime over w_2 indicates the derivative with respect to the argument. These roots have been extensively studied by Wait [7] and Logan [20], (also see Appendix B).

Similarly, the quantities in (18) are defined as follows:

$$F_1^S(\xi) = 1 - \frac{\sqrt{\pi j}}{2} \xi^{3/2} + \frac{j5}{12} \xi^3 + \frac{5}{64} \sqrt{\pi j} \xi^{9/2} + \dots \quad (20a)$$

$$F_2^S(kt) = \frac{e^{-j\beta_s t}}{\beta_s} \epsilon_s + \frac{e^{-jkt}}{k\sqrt{\pi}} Q(z) e^{z^2}; \quad \alpha_s \geq 0 \quad (20b)$$

$$\alpha_s = -jk \frac{Y_s}{Y_0}; \quad \beta_s = \sqrt{k^2 + \alpha_s^2} = 2\pi\lambda_s \quad (20c,d)$$

$$\tilde{b}_s = \frac{\alpha_s}{k} \sqrt{\frac{j}{2}}; \quad \alpha_s^- = -|\alpha_s|; \quad z = j\tilde{b}_s \sqrt{kt} \quad (20e,f,g)$$

$$\epsilon_s = \begin{cases} 1 \\ 0 \end{cases}, \quad \alpha_s \geq 0 \quad (20h)$$

in which the z of (20-g) is not to be confused with the z coordinates (the present analysis is independent of the z coordinate) and $Y_s = 1/Z_s$ is the surface admittance in mhos. σ_p are the roots of $w_2'(\sigma) - \alpha_s k^{-1} w_2(\sigma) = 0$.

The function Q is related to the complementary error function, erfc such that

$$Q(\Omega) = \frac{\sqrt{\pi}}{2} \text{erfc}(\Omega) = \int_{\Omega}^{\infty} e^{-x^2} dx.$$

It is important to point out that the asymptotic expansion for G^S given in (18a) is not unique. A second asymptotic expansion for G^S can be obtained from the tangential electric field (14) on s_1 due to a magnetic line dipole M , and the impedance boundary condition of (5a). Carrying out the necessary calculations yields

$$G^S(\tilde{Q}|Q') = \frac{\alpha_s}{k^2} \delta(\tilde{Q}|Q') + \left(\frac{\alpha_s}{k}\right)^2 G^e(\tilde{Q}^+|P') \quad (21)$$

where the expression for $G^e(\tilde{Q}^+|P')$ can be obtained from G^h of (17a) by simply changing the α_h and β_h to α_s and β_s . Consequently, incorporating G^S of (21) into the H field integral equation of (11a) yields

identically the same result as the one which is obtained via the E-field integral equation of (15) in conjunction with (16b). As pointed out earlier, (15) in conjunction with (16b) is to be preferred over (11a) in conjunction with (18a) for purposes of numerical calculations. It is interesting to note that if one adds the zero term, "1-1" to the integrand of (B46), one then again arrives at (21) after an appropriate recombination of the terms in the modified integrand.

It is observed that the approximation in (17a) and (18a) for G^h (and hence for G^e) and G^s are in terms of tabulated functions, and they can therefore be easily evaluated. The representations in (17a), (18a) and (16b) are valid for the arc lengths $Q'Q_1$ and $Q'Q_2$ which are only moderately large. For larger impedance patch lengths, i.e., for $t \gg t_m$, one must use a residue series representation of (17b) and (18b) for G^h and G^s , respectively. The development of the residue series representations given in (17b) and (18b) is also discussed in Appendix B; in particular, one is referred to (B37) and (B74) of Appendix B. Such a residue series representation has been studied extensively by Bremmer[21], Logan [20], and Wait[7]. However, the alternative representations in (17a) and (18a) which are valid close to the source appear to be different from those obtained by Wait[12]. Furthermore, the analysis [9] which was for a spherical surface, and only for the TE case, is not directly applicable to the 2-D case of interest here as it would lead to results that are not uniformly valid in the vicinity of the source (for both the TE_z and TM_z cases).

The representation in (17a) and (18a) for the TE_z and TM_z cases, respectively consists of several terms which have an important physical significance. The first set of terms in (17a) and (18a) corresponding to G^h and G^s of (B10) and (B49) in Appendix B, respectively represent the high frequency currents on a perfectly conducting circular cylinder; whereas, the remaining terms represent a perturbation or correction arising from the presence of a non-zero surface impedance. Furthermore, the first terms in (17a) and (18a) are expressed as a product of the currents on a perfectly conducting planar surface and the perturbation effects arising from the finite curvature of the perfectly conducting circular cylinder. Also, the second set of terms in (17a) and (18a) which represent an impedance perturbation to the perfectly conducting circular cylinder, have the same form as the impedance perturbation to a planar conducting surface. Thus, if these second set of terms were used in conjunction with "only those parts" of the first set of terms which correspond to the planar conducting surface, one would then obtain the same asymptotic currents as those on a planar impedance surface. Finally, the last set of terms in (17a) and (18a) are additional corrections to the first two sets of terms arising from a combination of curvature and impedance effects. Further details on the physical interpretation

of G^b for the completely impedance covered circular cylinder are available in Appendix B. It is important to note however, that the results in both (17a) and (18a) firstly reduce to the perfectly conducting circular cylinder case if the surface impedance vanishes, provided a slight loss is introduced in the external medium (free space) before performing the limit on (18a) to recover the perfectly conducting case. Secondly, they reduce to the results for the planar impedance surface as the curvature of the cylinder becomes vanishingly small. Thirdly, the results in (17a) and (18a) reduce to the results for a perfectly conducting planar surface as the curvature vanishes, and the surface impedance also vanishes. As pointed out earlier, the expressions for the surface currents should be well approximated in the vicinity of the source in order to obtain the radiation fields accurately. Since the radiation patterns calculated via SCIM are found to agree very well with those based on other trustworthy independent calculations, it is inferred that (17a) and (18a) are adequate for describing the source currents in the vicinity of the source.

The extension of the circular cylinder results in (17a) and (18a) to an arbitrary convex cylinder with a slowly varying curvature, in which the cylinder is completely covered by an impedance surface is carried out by assuming that each point on the cylinder may be approximated locally by a circular cylinder of the same local radius of curvature at that point. As mentioned previously, this procedure is based on the local properties of high frequency fields as employed in the GTD procedure. Thus, one replaces t of (19a) by $\int_0^{\tilde{Q}} dt$ where \tilde{Q} is the observation point of the currents on the impedance patch as shown in Figure 1; also, the Fock parameter, ξ of (19d) is replaced in the usual manner[22] by an integral to account for the variation of the surface curvature. To this end, one proceeds as follows. As in (19d)

$$\xi = m|\phi| = m \frac{t}{a} \quad (22a)$$

where a is the radius of the cylinder and t is the arclength defined in (19c). Since m (given in (19e)) is assumed to be slowly varying, then (22a) can be differentiated, yielding

$$d\xi \approx m \frac{dt}{\rho_g} \quad (22b)$$

where ρ_g in (22b) is now the local radius of curvature. Integration of (22b) from Q' to Q results with

$$\xi = \int_{Q'}^{\tilde{Q}} \frac{m dt}{\rho_g} ; \quad m = \left(\frac{k \rho_g(t)}{2} \right)^{1/3} \quad (23)$$

In (23), m may be taken outside the integral if one replaces m by $\sqrt{m(Q') m(\tilde{Q})}$ to represent some type of averaging effect to account for the slowly varying curvature; one notices that such an averaging is the geometric mean of m between points Q' and \tilde{Q} . Furthermore, this averaging effect is consistent with reciprocity.

In this work, the length of the impedance patch can be small; however, it cannot be too small such that the source at Q' lies close to either edge of the patch (at Q_1 and Q_2 of Figure 1). This is not a serious restriction since in practical situations of interest here, the patch needs to be at least moderately large enough in order to have a marked effect on the radiation patterns. Over such moderate distances from the source to the edges, the field component which continually leaks energy off the surface (unlike an Elliot mode type field which leaks little energy) is in general sufficiently weak at the edges of the patch to where the reflection of this field which travel back toward the source (while again shedding energy) may be neglected in the calculation of the radiation field. Furthermore, even the approximate asymptotic calculation of these reflections appears to be a rather complicated task which is not considered here. On the other hand, the current can be substantially modified by the reflection of an Elliot type mode field from the edges of the impedance patch. Hence, the present analysis incorporates the reflection of such an Elliot mode field through the use of a local reflection coefficient defined at the edges of the impedance patch. This reflection coefficient is found from the solution to the canonical problem of surface wave reflection from a discontinuity in planar impedance boundaries as shown in Figure 5. To recapitulate, one therefore basically assumes here that the total field incident on the edges of the impedance patch generates a reflected wave on the surface which is well approximated by only the reflected Elliot type mode field, since this mode is the dominant contributor to the surface field. The remaining, less significant component of the reflected field which is neglected consists of propagating and non-propagating (or evanescent) parts; the latter part does not contribute to the radiated fields and its exclusion is therefore justified. The propagating part is essentially a non-surface wave type field

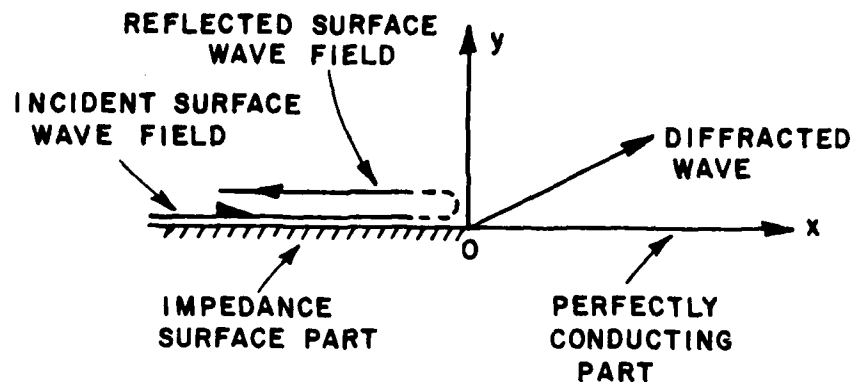


Figure 5--Geometry of the canonical problem of surface wave diffraction by a discontinuity in surface impedance associated with two part, planar impedance.

which leaks energy off the surface; in general it contributes sufficiently weakly to the radiated field for impedance patch lengths which are not extremely small and hence it is ignored.

The canonical two part problem in Figure 5 above has been analyzed via the Wiener-Hopf technique in conjunction with Weinstains factorization procedure[4]. The latter factorization procedure leads to relatively simple Wiener-Hopf factors. From [4], it is found that the surface wave reflection coefficient, R_s for this problem is

$$R_s = j \frac{\alpha_s}{\beta_s} e^{\frac{j}{\pi} \int_0^{2\xi} \frac{u}{\sinh u} du} ; \quad \xi = \sinh^{-1} \frac{\alpha_s}{k}; \text{ TM}_z \text{ case (24)}$$

$$R_h = - \frac{k - \beta_h}{\beta_h} e^{\frac{j}{\pi} \int_0^{2\xi} \frac{u}{\sinh u} du} ; \quad \xi = \sinh^{-1} \frac{\alpha_h}{k}; \text{ TE}_z \text{ case (25)}$$

The plots of R_h and R_s are illustrated in Figures 6 and 7, respectively.

As pointed out earlier, $G_p^{h,s}$ represents the perturbation to the current on the patch. This perturbation term arises from the truncation of the impedance surface at Q_1 and Q_2 . In the following

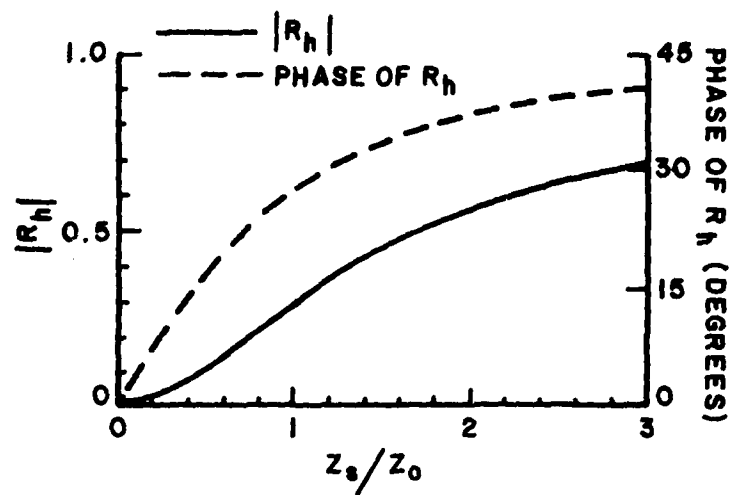


Figure 6--The magnitude and the phase of the reflection coefficient, R_h for the TE_z -case.

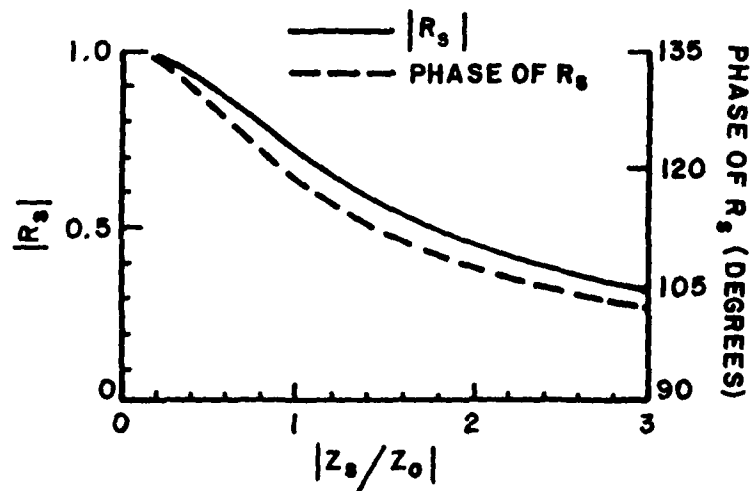


Figure 7--The magnitude and the phase of the reflection coefficient, R_s for the TM_z case.

analysis, the subscripts "s" and "h" are dropped, since it is equally applicable to both the TE_z and the TM_z cases.

Incorporating the above values of R , the G_R can be calculated via a self consistent procedure as follows:

The total incident current, $G_T(Q_1)$ at Q_1 consists of two terms which are the current $G(Q_1)$ generated by the principle source and observed at Q_1 , and the current, $G_R(Q_1|Q_2)$ reflected from Q_2 and evaluated at Q_1 , i.e., $G_T(Q_1) = G(Q_1) + G_R(Q_1|Q_2)$ as shown in Figure 8. The total incident current $G_T(Q_2)$ at Q_2 can be found similarly by interchanging subscripts 1 and 2, above. The term $G_R(Q_1|Q_2)$ can be related to $G_T(Q_2)$ via the reflection coefficient such that

$G_R(Q_1|Q_2) = R G_T(Q_2) e^{-j\beta \overline{Q_1 Q_2}}$, where $\overline{Q_1 Q_2}$ denotes the arclength between Q_1 and Q_2 . Similarly, the term $G_R(Q_2|Q_1)$ (which arises in the process of calculating $G_T(Q_2)$) can be written in terms of R , $G_T(Q_1)$ and $\overline{Q_2 Q_1}$. One may then solve for $G_T(Q_1)$ and $G_T(Q_2)$. It can be shown that:

$$G_T(Q_1) = \frac{G(Q_1) + R e^{-j\beta \overline{Q_1 Q_2}} G(Q_2)}{1 - R^2 e^{-j2\beta \overline{Q_1 Q_2}}} \quad (26)$$

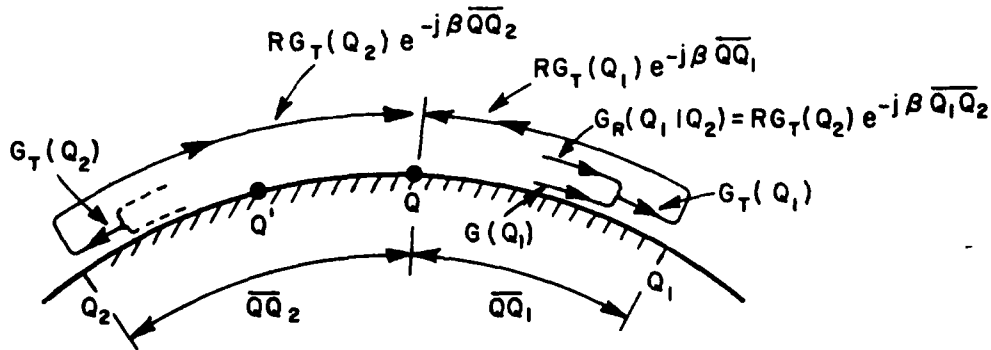


Figure 8--Incident and reflected rays associated with the self consistent method.

Interchanging subscripts 1 and 2 in (26) gives the corresponding expression for $G_T(Q_2)$. One notes that (26) reduces to a more familiar result when the source point is located at the center of the patch

so that $G(Q_1) = G(Q_2)$; in which case $G_1(Q_1) = G(Q_1) (1 - R e^{-j\beta Q_1 Q_2})^{-1}$. The perturbation current at a point Q on the patch is then given by the following equation

$$G_R(Q) = R G_T(Q_1) e^{-j\beta Q_1 Q} + R G_T(Q_2) e^{-j\beta Q Q_2}. \quad (27)$$

As the value of Z/Z_0 becomes smaller than 0.5, the corresponding values of $|R_s|$ becomes larger than 0.9 as seen from Figure 7. Such a large value of the reflection coefficient R_s implies via (27) that a very large number of multiple bounces between the edges of the impedance patch remain significant in the calculation of the TM_z Elliot mode field. In such a situation, the accuracy of the present solution (SCIM) may be impaired, because, a small error in the approximation to the Elliot mode field which is directly incident from the source onto the edges of the patch could be compounded through each subsequent reflection (bounce) from the edges. In practice, one would not employ values of $|Z/Z_0|$ for which $|R_s|$ is large anyway, as this is obviously not desirable from an antenna design point of view.

Furthermore, the earlier assumption; that is, the propagating, non-surface wave type fields which are generated by the "reflections" of Elliot mode from the edges contribute sufficiently weakly to the radiated field, does not hold for such large values of the reflection coefficient. Excluding this non-surface wave field results in an inaccurate representation of the currents on the patch in the vicinity of the edges. However, as indicated earlier, an accurate representation of the currents on the impedance patch is essential for accuracy in the SCIM. One notes that in the SCIM, an integration of the component of the current reflected from the edges gives rise to fields diffracted not only from the edges on which the reflected component terminates, but also from the opposite edges where the reflected component originates. The latter "spurious diffracted field" contribution is sensitive to errors in the currents at the edges; however, these errors are generally not large if the reflection coefficient is sufficiently small. An alternative approach for including the effects of multiple reflections in the total radiation field calculation is to simply superpose the solution based on the SCIM but without including the correction currents resulting from the reflections of the Elliot modes, with the part of the GTD ray solution of [4] for calculating the diffracted fields which result only from these reflections. The latter GTD diffracted field contribution is calculated via the self consistent approach for summing up the multiple reflections of the Elliot modes as indicated earlier. It is noted that,

the GTD solution does not require an exact knowledge of the form of the currents in the vicinity of the edges, hence it is suitable for the evaluation of the contribution to the radiation pattern from the multiple reflections. Furthermore, this alternative procedure is attractive from the point of making the numerical radiation field calculations more efficient.

C. Numerical Evaluation of the Surface Currents on the Impedance Patch

The last step of this analysis is to evaluate the integrals in (11a), (11b) and (15), numerically over the impedance patch. As pointed out earlier, $H_0^{e,m}(\tilde{Q}|P')$ is the magnetic field on the impedance patch due to an electric (magnetic) line source at P' ; $H_0^{e,m}(\tilde{Q}|P')$ is a well behaved function of the arclength on the cylinder and suitable for a numerical integration technique. The explicit form of this magnetic field is given in [1,2] and will not be repeated here.

The term $\hat{n}xH_b(\tilde{Q}|Q')$ in (11b) is related to (17a) via (16a). As it can be seen from (17a), this term has a log-type singularity (small argument approximation for $H_1^{(2)}(kt)$) as the variable of integration (i.e., the arclength) goes through the source. Such integrable singularities can be treated numerically in the computer via Gaus' method. Thus, the TE_z case presents no numerical difficulties. However, the term $\hat{n}xH_b(\tilde{Q}|Q')$ in (11a) is much too singular for a numerical integration scheme. In fact, from (18a), with the useage of the small argument approximation of $H_1^{(2)}(kt)$, one can show that this singularity is in the form of an inverse square of the arclength type (i.e., $1/(\text{arclength})^2$). Such singularities are not suitable for a numerical integration procedure and therefore one must reduce the singularity by means of the distributed source technique before any calculation work can be done. To this end, one proceeds as follows for the $\hat{n}xH_b$ of the TM_z case. Let the source be a distributed sinusoid such that the distribution function, $\Lambda(x')$ is given by

$$\Lambda(x') = \frac{\sin k(w-|x'|)}{\sin kw}, \quad (28)$$

where $2w$ is the total extent of the source. The resulting current on the patch from the sinusoidally distributed source can be found by weighting the currents generated by an infinitesimal source with the distribution function, $\Lambda(x')$ and then integrating it from $-w$ to w , i.e.,

$$\hat{n}x\bar{H}_b(\bar{Q}) = \int_{-w}^w \Lambda(x') \hat{n}x\bar{H}_b(\bar{Q}|Q') dx' , \quad (29)$$

where $\bar{H}_b(\bar{Q})$ and $\bar{H}_b(\bar{Q}|Q')$ in (29) are the magnetic fields observed at a point \bar{Q} on the surface of the patch due to a sinusoidally distributed magnetic line dipole, and an infinitesimal magnetic line dipole, respectively.

As mentioned above, the singularity of $\hat{n}x\bar{H}_b(\bar{Q}|Q')$ in (29) has the $H_1^{(2)}(kt)/kt$ form (see Equation (18a)) which can be rewritten as

$$\frac{H_1(kt)}{kt} = \left(1 + \frac{d^2}{d(kt)^2}\right) H_0^{(2)}(kt) . \quad (30)$$

In general, if a function, $F(k|x-x'|)$ can be rewritten in terms of another function $f(k|x-x'|)$ via

$$F(k|x-x'|) = \left[1 + \frac{d^2}{d^2(k|x-x'|)^2}\right] f(k|x-x'|) \quad (31)$$

then the integral of $F(k|x-x'|)$ with $\Lambda(x')$ over the interval $(-w,w)$ can be expressed in terms of $f(k|x-x'|)$ as follows

$$I = \int_{-w}^w \Lambda(x') F(k|x-x'|) dx' = \int_{-w}^w \Lambda(x') \left(1 + \frac{d^2}{d^2(k|x-x'|)^2}\right) f(k|x-x'|) dx' . \quad (32)$$

Repeated application of integration by parts to (32) yields

$$I = \Lambda(x') f'(k|x-x'|) \Big|_{-w}^w - \Lambda'(x') f(k|x-x'|) \Big|_{-w}^w + \int_{-w}^w dx' \Lambda(x') + \Lambda''(x') f(k|x-x'|) , \quad (33)$$

where primes over the functions indicate derivatives with respect to the argument.

The first term in (33) is zero because $\Lambda(\pm w)=0$. Furthermore the last term in (33) is also zero, because $\Lambda''(x') = -\Lambda(x')$. Hence (33) becomes

$$I = -\Lambda'(x')f(k|x-x'|)|_{-w}^0 - \Lambda'(x')f(k|x-x'|)|_0^w. \quad (34)$$

From the definition of $\Lambda(x')$, it can be shown that

$$\frac{d}{dx'} \Lambda(x') = \mp \frac{\cos k(w-|x'|)}{\sin kw} ; \quad x' \geq 0 \quad (35)$$

Substituting (35) into (34) yields the desired relationship

$$\begin{aligned} \int_{-b}^b \Lambda(x') \left(1 + \frac{d^2}{d(k|x-x'|)^2} \right) f(k|x-x'|) dx' &= \frac{1}{\sin kw} [f(k|x-w|) \\ &+ f(k|x+w|) - 2 \cos kw f(k|x|)] \end{aligned} \quad (36)$$

Substituting (30) into (18a) and employing (36) yields

$$\begin{aligned} \tilde{G}^S \sim & \sum_{i=-1}^1 \left[\frac{1}{2j} H_0^{(2)}(kt_i) F_1^S(\xi_i) - \frac{1}{2j} H_0^{(2)}(kt_i) \{1 - 2z_i e^{z_i^2} Q(z_i)\} \right] + \\ & + \int_{-b}^b \Lambda(t') \left[-j \frac{\alpha_s^3}{k^2 \beta_s} e^{-j\beta_s |t_0 - t'|} \epsilon_s + \frac{jk}{2} \left(1 - \alpha_s \frac{d}{d\alpha_s} \right) \right. \\ & \left. F_2^S(k|t_0 - t'|) \right] dt' + \frac{2\alpha}{\beta} \Lambda(t_0) \epsilon_s \end{aligned} \quad (37)$$

where \tilde{G}^S is the integral of G^S of (18a) weighted by $\Lambda(t')$ over the interval $-w$ to w . The t_1 , t_0 and t_{-1} are the arclengths between the observation point Q^1 on the patch and the points $-w$, 0 , and w of the distributed source, respectively as shown in Figure 9. ξ_i and z_i are defined in terms of t_i in a similar fashion,

such that $\xi_i = m \frac{t_i}{a}$ and $z_i = j\tilde{\beta}_s kt_i$. The result in (37) can be generalized to an arbitrary convex cylinder with a slowly varying curvature via (23).

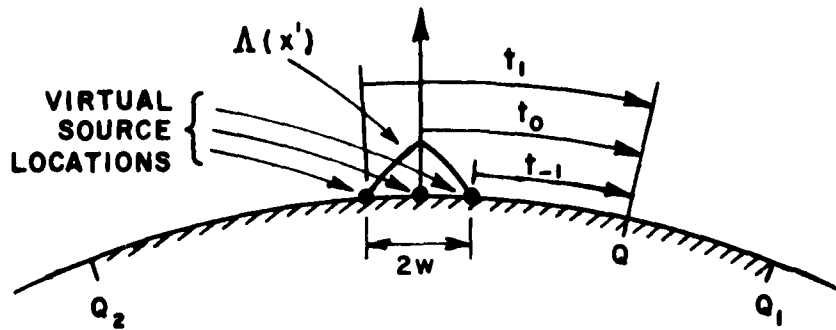


Figure 9--Sinusoidally distributed line source and related parameters.

The resulting current on the patch due to a distributed source, $\Lambda(t')$ can now be written as follows

$$\hat{n} \times \vec{H}_b(\vec{Q}|\vec{Q}') = -jY_0 M_d (\vec{G}^S + \vec{G}_R^S) \hat{z} \quad (38)$$

\vec{G}_R^S can be obtained from (27), if one uses \vec{G}^S instead of G^S .

As it can be seen from (37), the highest singularity in (38) is a log-type singularity; hence, the resulting integrals upon substitution of (38) into (11b) can be evaluated numerically as principal values.

The alternative formulation of the TM_z discussed above in Section IIB is recommended for the following reasons. Firstly, the currents of (18a) to be employed in the reaction integral formulation given in (11a) are highly singular at the source and therefore it is very difficult to obtain a satisfactory mathematical representation for the fields. Secondly an attempt at smoothing out these singularities (as it is done above) for the purposes of numerical treatment leads to a rather complicated and slow computer code. It is however important to point out that the results obtained from (11a) agree very well with other independent checks such as MM-GTD and GTD techniques. Nevertheless, the electric field integral representation given in (15) for the TM_z case is superior to the one given in (11a) because the formulation in (15) leads to source singularities which can be numerically integrated in the principle value sense; this numerical treatment is not complicated, and it leads to faster computer codes. Furthermore, the computer code for numerically processing the electric field

representation of (15) for the TM_z case can be obtained from the code for the TE_z case (11b) with only minor changes; hence, both cases can be incorporated into a single computer code. It is however important to note that, in the process of numerical integration, one should divide the impedance patch into small enough segments so that the integral subroutines can sample the variations of the currents on the patch accurately. It is observed that the segments which are as long as half an electric wavelength; i.e., π/β can accurately be integrated via a 5-point Gaussian quadrature formula. The β (β_h for TE_z and β_s for TM_z) is given in (19g) and (20d).

CHAPTER III

RELIABILITY OF THE SURFACE CURRENT INTEGRATION METHOD (SCIM)

This chapter is designed to establish the validity of the present analysis by comparing it with other independent methods. These numerical comparisons of the SCIM are illustrated only for the circular cylinder geometry of Figure 10. Nevertheless, as pointed out earlier, the present analysis based on the SCIM can also be directly employed to treat convex cylinders of arbitrary cross sections. For convenience, the source is located in the middle of the impedance patch. The impedance patch width is defined in terms of the angle, ϕ_p measured from the source. The angles, ϕ and ϕ_R specify the points on the impedance patch and the observation direction in the far field, respectively.

The SCIM is compared with three independent methods. Two of these methods are based on the different mathematical models of the problem, and they are called the MM-GTD and the GTD formulations. Some experimental results are also included as a third method. It is noted that like the SCIM, the MM-GTD and GTD formulations are also asymptotic in the sense that they are developed for electrically large cylinders. The MM-GTD and the GTD formulations are discussed in detail elsewhere [2,4] and some of the main features of these methods have been discussed in Chapter I, hence only a short summary of these methods will be repeated here for completeness.

The MM-GTD, a hybrid technique, combines the method of moments and the geometrical theory of diffraction. An application of the generalized reaction theorem, in a manner analogous to that employed in the development of the result in Figure 11, yields the governing integral equation employed in the present MM-GTD formulation as:

$$\int_{S_1} \vec{H}_{oz}(\vec{Q}|\vec{Q}') \cdot [Z_s(\vec{Q}) \hat{n} \times \hat{n} \times \vec{H}_b^m(\vec{Q}|\vec{P})] d\ell = -\vec{H}_b^m(\vec{Q}'|\vec{P}) \cdot \hat{z} + \vec{H}_{oz}(\vec{P}|\vec{Q}') \cdot \hat{z}$$

For TE_z case (39a)

$$\int_{S_1} \vec{H}_{ot}(\vec{Q}|\vec{Q}') \cdot [Z_s(\vec{Q}) \hat{n} \times \hat{n} \times \vec{H}_b^e(\vec{Q}|\vec{P})] d\ell = -\vec{H}_b^e(\vec{Q}'|\vec{P}) \cdot \hat{r} - \vec{E}_{ot}(\vec{P}|\vec{Q}') \cdot \hat{z}$$

For TM_z case. (39b)

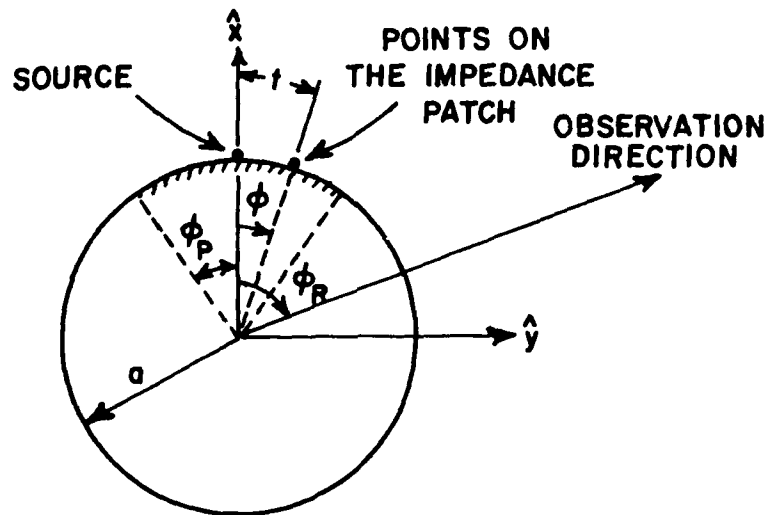


Figure 10--The antenna geometry and the related parameters.

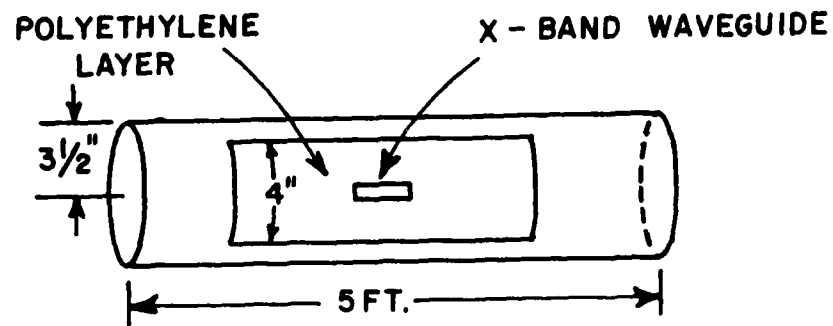


Figure 11--An illustration of the experimental set up.

In (39), \vec{H}^{0z} and \vec{E}^{0z} are produced by the source $\vec{M}_z = \hat{z}\delta(|\vec{p}-\vec{p}_0|)$; whereas \vec{H}^{0x} and \vec{E}^{0x} are produced by $\vec{M}_x = \hat{x}\delta(|\vec{p}-\vec{p}_0|)$. As in the SCIM, the subscripts "0" and "b" in (39), denotes the fields of the unperturbed and perturbed problem respectively. Equations (39a) and (39b), are first order inhomogeneous integral equations with unknown \vec{H}^b and \vec{E}^b respectively, and they can be solved via the moment method technique. What differentiates this method from the conventional moment method solution of integral equations pertaining to electromagnetic problems is the fact that in the former one, the free space Green's function is used as the kernel of the integral equation; whereas in the present analysis, a uniform GTD approximation for the perfectly conducting convex cylinder Green's function constitutes the kernel. This is the reason behind choosing the name MM-GTD. At the present time, the MM-GTD solution for the TE_z case appears to be very accurate; on the other hand, the TM_z case is expected to be only reasonably accurate since further work is needed to refine the MM-GTD procedure for the TM_z case as indicated in [5].

The GTD method is a ray optical method, and the ray picture for this problem is illustrated in Figure 2. The direct (or geometrical optics) ray field and the fields diffracted from the edges of the patch are calculated from appropriate canonical problems for TM_z and TE_z cases as explained in [4]. It is noted that the GTD solution presented in [4] is restricted to only those impedance surfaces which can support an Elliot type surface ray mode field.

As indicated above, an experimental verification of the accuracy of the SCIM solution is also carried out in this study. This verification is for the TE_z case. The experimental set-up consists of a 5 ft long, $3\frac{1}{2}$ inch radius cylinder, which models the infinitely long perfectly conducting cylinder. An x-band waveguide feeds an axial slot in this cylinder as illustrated in Figure 11. Polyethylene layers which are 4 inches wide, and 0.058 inches thick are employed to simulate the impedance patch. The value of the impedance can be changed by altering the number of polyethylene layers. The measurements are conducted at 10.77 GHz. At this operating frequency, the complex, dielectric constant of polyethylene is found to be $\epsilon = (2.25 + j9 \times 10^{-4})\epsilon_0$; ϵ_0 being the permittivity of the free space.

Comparisons of the results for the radiation patterns based on the SCIM with those based on the MM-GTD, the GTD, and the experimental data are presented in Figures 12 through 28.

The GTD patterns presented here appear to be reasonably accurate. However, it is observed that the GTD results in [4] for the circular cylinder TM_z case in general need to be refined further to make them as reliable as for the TE_z case, especially for a wider range of parameters than those considered in the GTD calculations presented here. In the case of a cylinder with a very small curvature

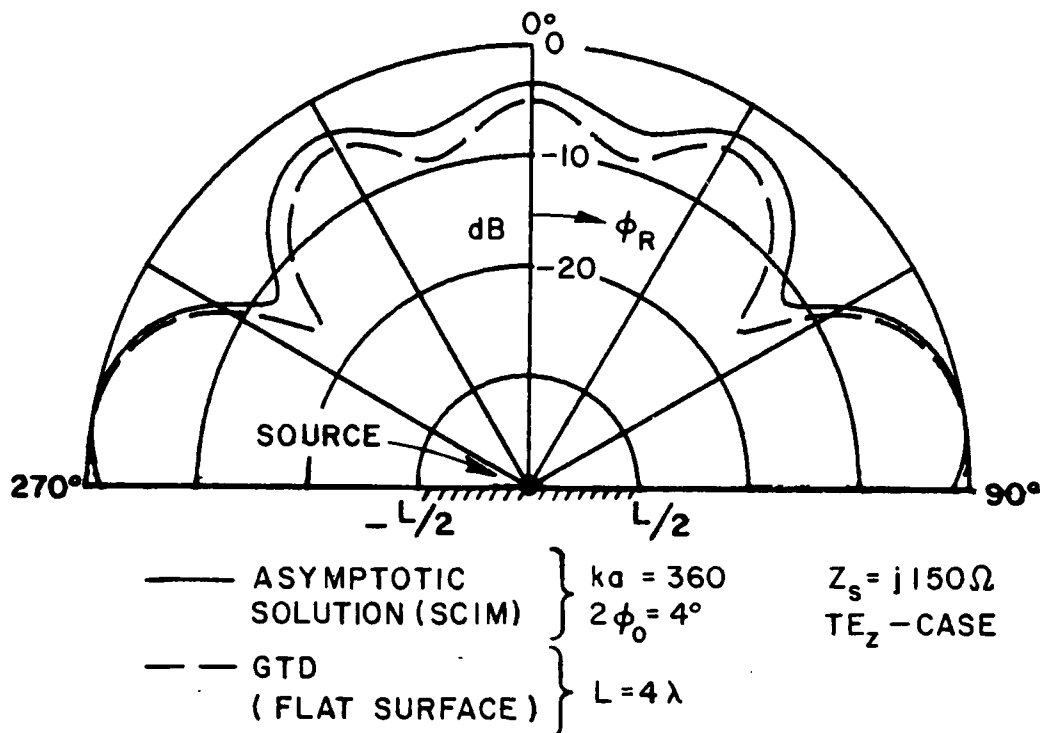


Figure 12--Radiation patterns of a magnetic line source on perfectly-conducting planar and circular cylindrical surfaces which are partly covered with an impedance surface patch.

($ka=360$), the asymptotic analysis (SCIM) in Figures 12, 13, 14, 25 and 26 are also compared with the results obtained from the GTD analyses for an impedance patch on a perfectly conducting ground plane (which is the limiting case of a cylinder with vanishing curvature.) These radiation patterns of an antenna on a flat surface can be used to predict with reasonable accuracy the pertinent parameters of the radiation patterns in the lit region of a similar antenna located on a cylindrical surface with small curvature.

In Figures 15 through 22, and 27 and 28, the SCIM is compared with the GTD and MM-GTD results. It is observed that the results obtained from these three independent methods compare very well with each other. However, it should be pointed out that there are no MM-GTD results presented for the TM_z case. This is because it is very cumbersome to obtain a satisfactory MM-GTD solution for this case at the present time, as has been mentioned before.

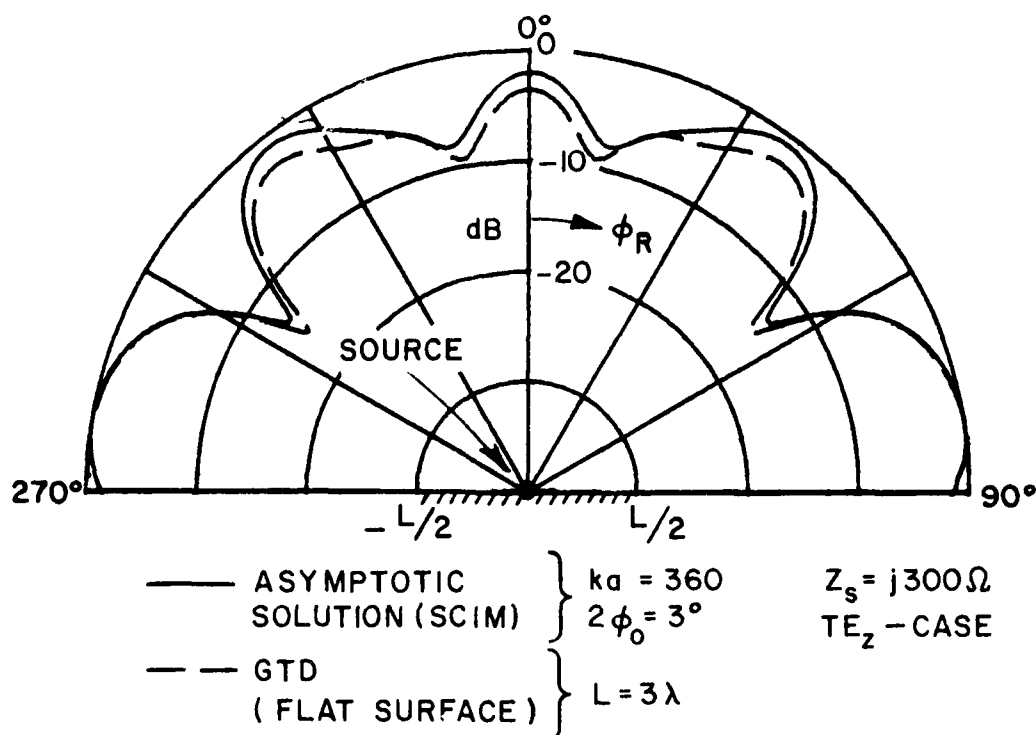


Figure 13. Radiation patterns of a magnetic line source on perfectly-conducting planar and circular cylindrical surfaces which are partly covered with an impedance surface patch.

The relative merits of these three methods (i.e., SCIM, MM-GTD and GTD) are presented in Table I. In Figures 22, 23, and 24, where the SCIM is compared with experimental results, it is modified by taking the impedance surface as being slightly lossy to account for the loss in polyethylene panels. The loss is introduced into the solution as an exponential decay along the impedance surface. From this point of view the solution may be considered as a perturbation to the lossless case. The SCIM is further modified by introducing the effect of the finite source distribution in the axial slot via a multiplicative slot pattern factor. The polyethylene layers are modeled as an impedance surface. These polyethylene layers which are 0.058 inches and 0.106 inches thick for the two experimental cases may be approximated by an equivalent impedance of $Z = j70\Omega$ and $Z = j150\Omega$, respectively; this equivalent inductive impedance is based on the flat surface approximation and the corrections to this impedance arising from the curvature of the cylinder have been ignored since the cylinder is over twenty wavelengths in circumference.

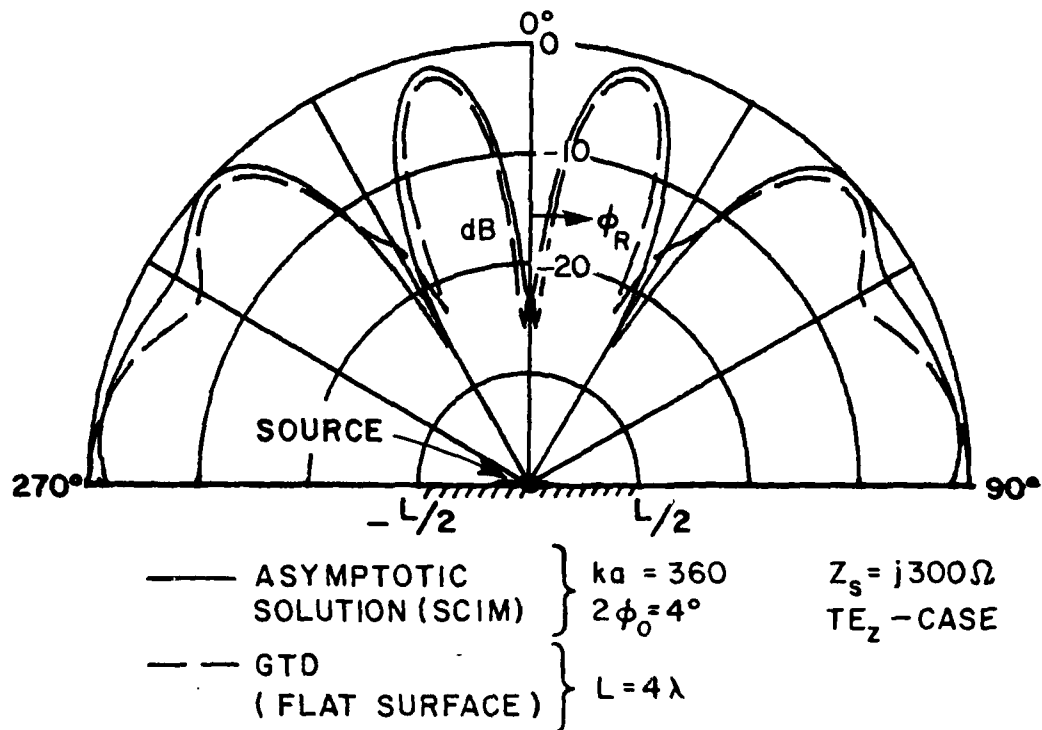


Figure 14. Radiation patterns of a magnetic line source on perfectly-conducting planar and circular cylindrical surfaces which are partly covered with an impedance surface patch.

Finally, it is recognized that the TM_z case is very nearly a dual of the TE_z configuration. The principle difference is that the TM_z source is a magnetic line dipole source which is of course not a dual of the magnetic line source and the conducting part of the surface in the TE_z case is not replaced by its dual for the TM_z case. Nevertheless, by a proper choice of surface impedances, it is possible to generate patterns (for the TM_z case) similar in nature to the smooth patterns of the TE_z case presented in this chapter. The following results for the TM_z case are taken for the range of impedances such that high ripples occur in the radiation pattern. This is done merely to compare the SCIM with the GTD solution in the domain where they both are valid, and to supplement the computations for the smooth patterns for the TE_z case. It is emphasized that smooth patterns can also be generated for the TM_z case as is shown in Figures 46 through 51.

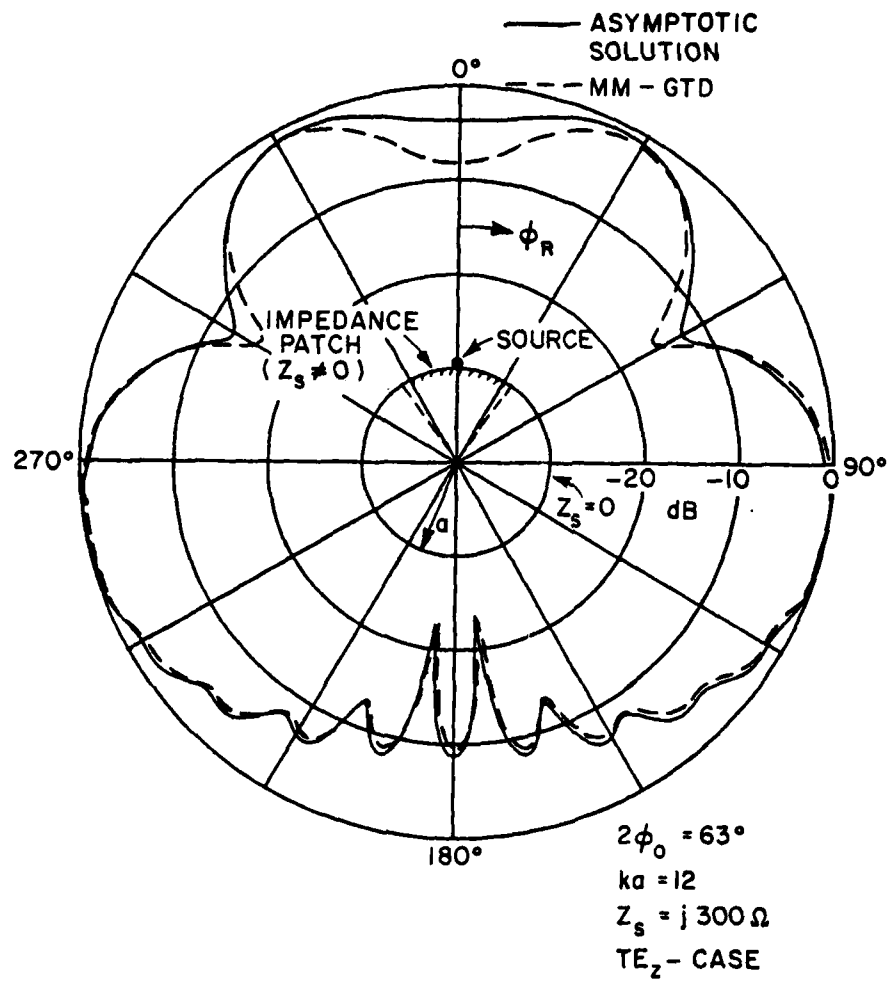


Figure 15--Radiation patterns of a magnetic line source on perfectly-conducting circular cylinder which is partly covered with an impedance surface patch.

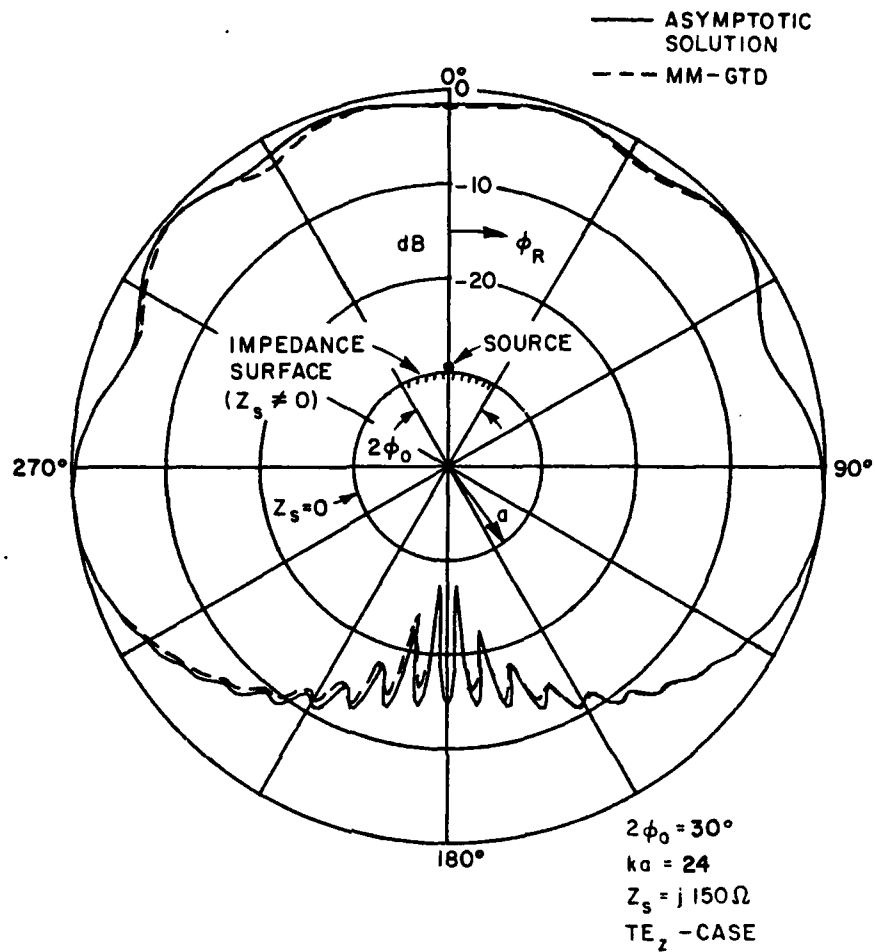


Figure 16--Radiation patterns of a magnetic line source on perfectly-conducting circular cylinder which is partly covered with an impedance surface patch.

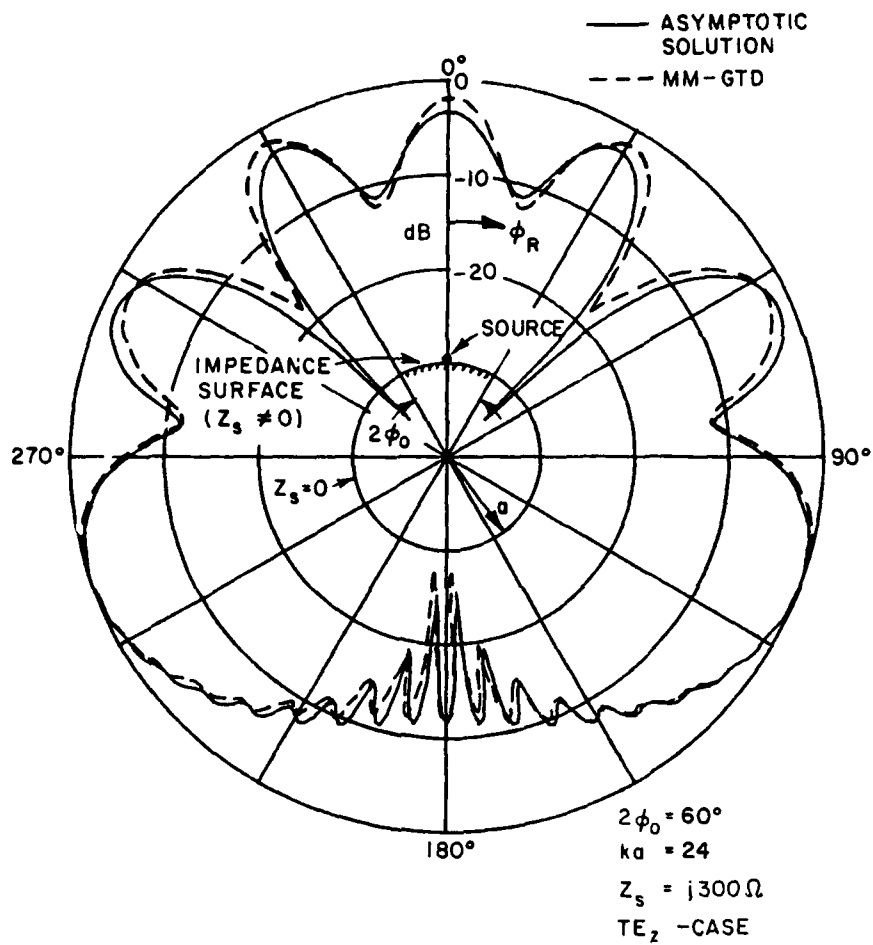


Figure 17--Radiation patterns of a magnetic line source on perfectly-conducting circular cylinder which is partly covered with an impedance surface patch.

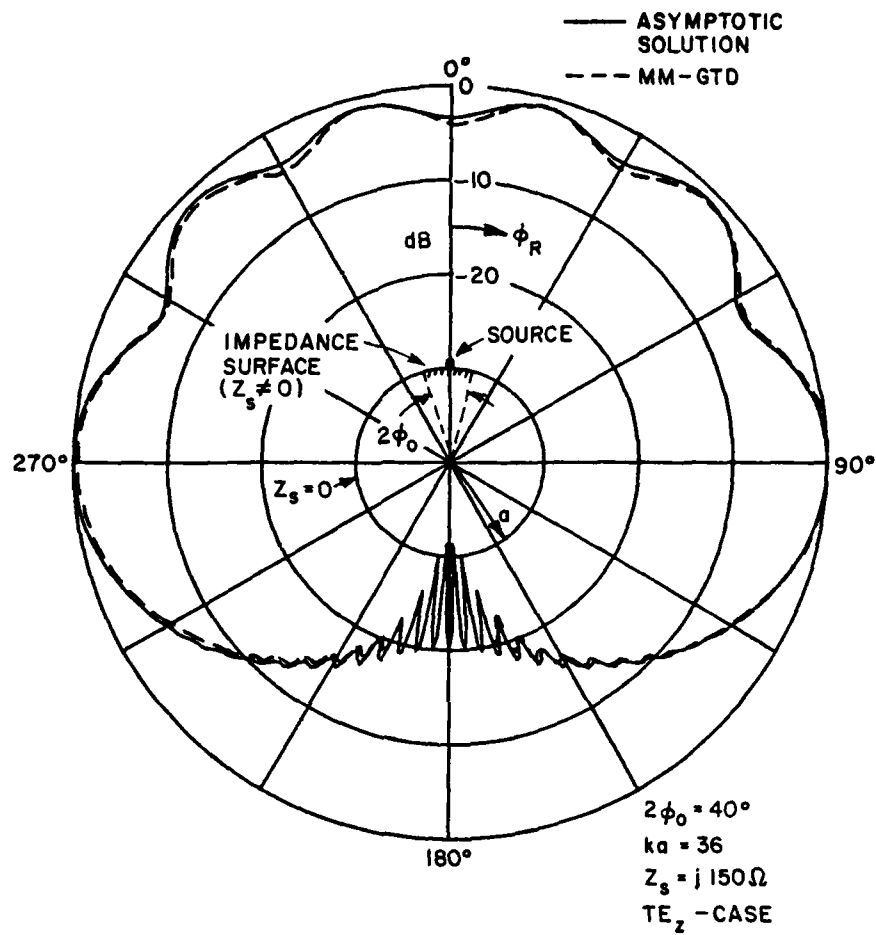


Figure 18--Radiation patterns of a magnetic line source on perfectly-conducting circular cylinder which is partly covered with an impedance surface patch.

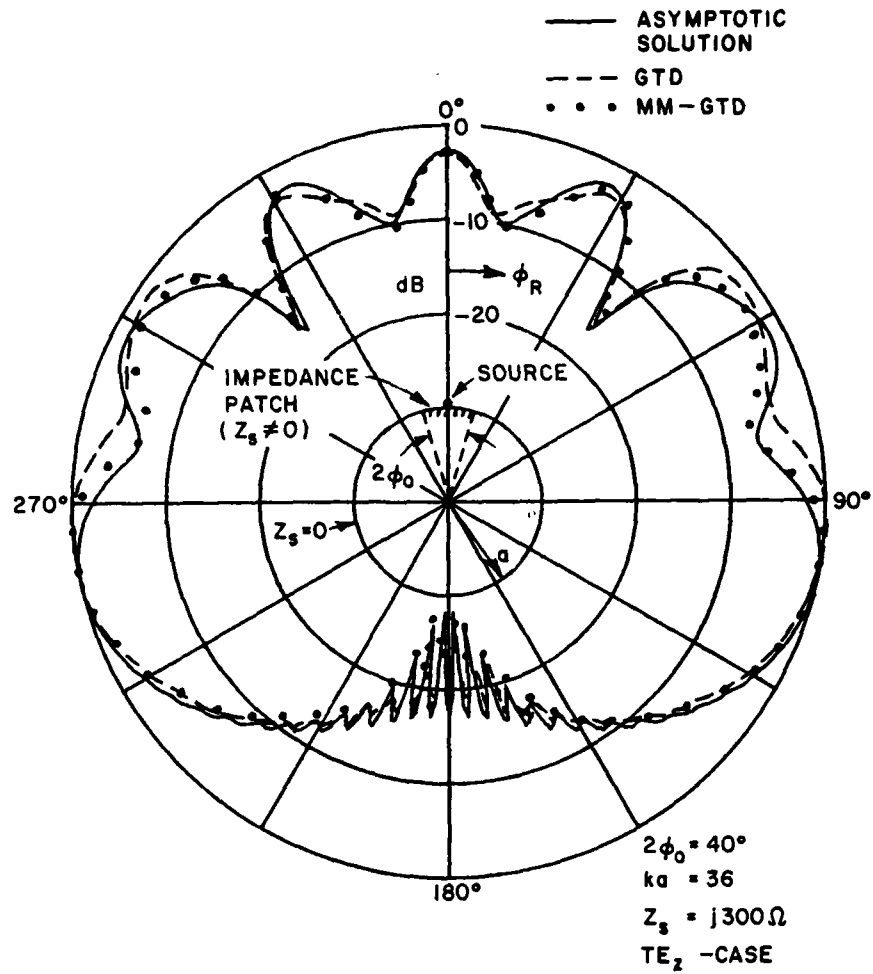


Figure 19--Radiation patterns of a magnetic line source on perfectly-conducting circular cylinder which is partly covered with an impedance surface patch.

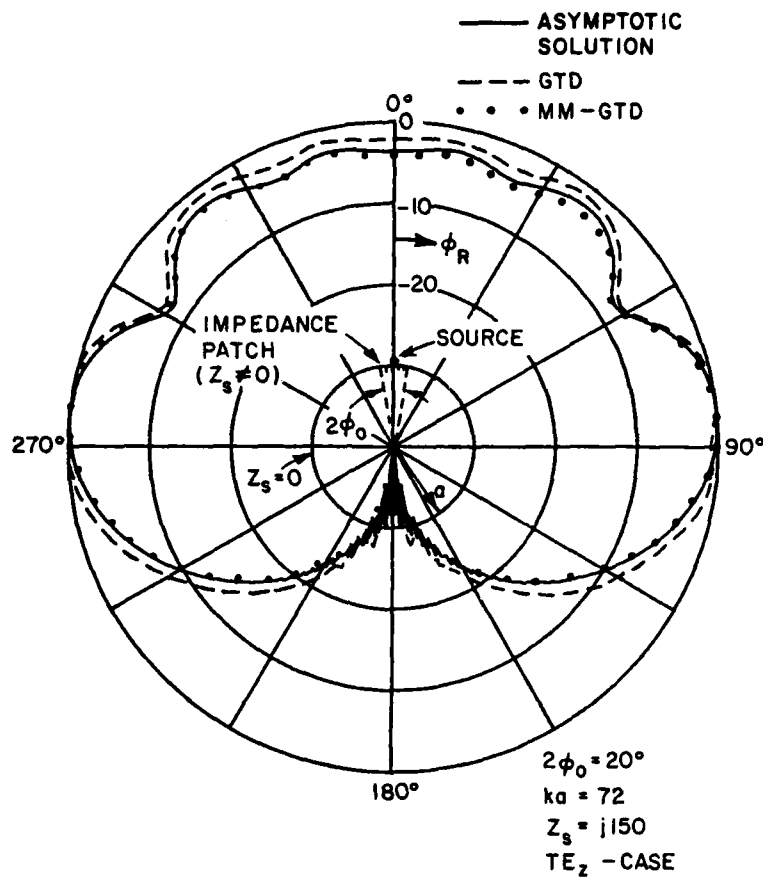


Figure 20--Radiation patterns of a magnetic line source on perfectly-conducting circular cylinder which is partly covered with an impedance surface patch.

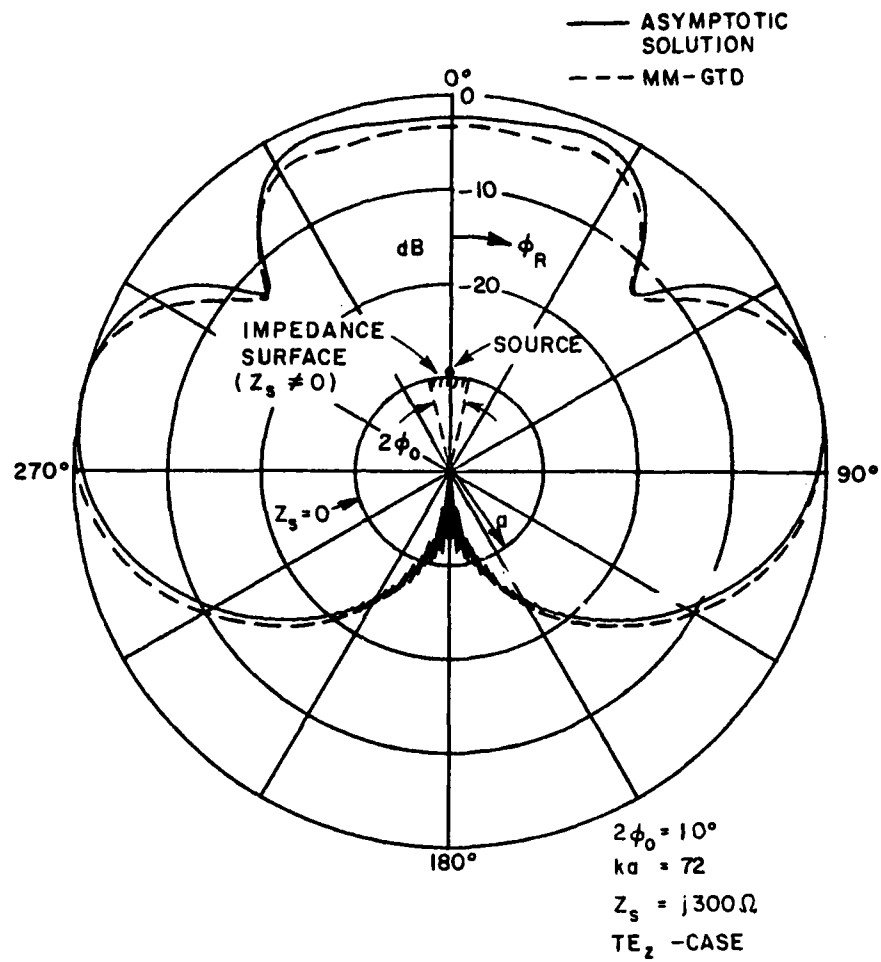


Figure 21--Radiation patterns of a magnetic line source on perfectly-conducting circular cylinder which is partly covered with an impedance surface patch.

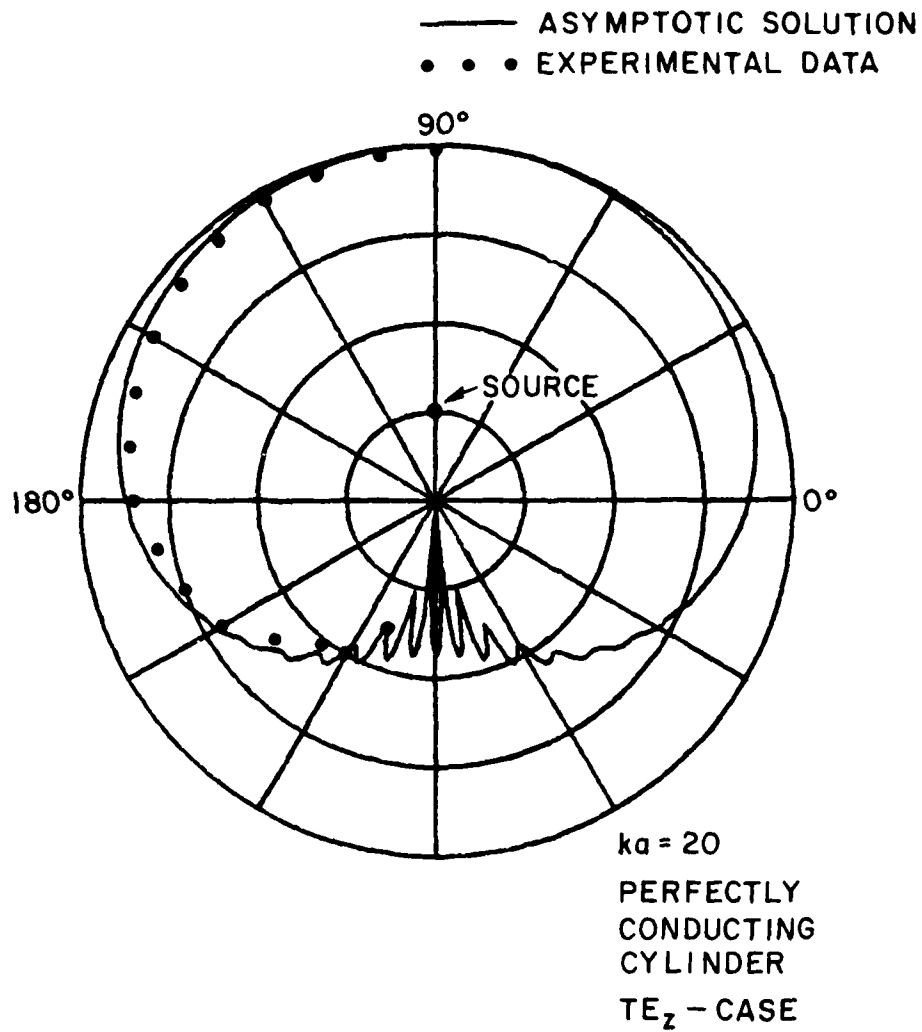


Figure 22--Radiation patterns of a magnetic line source on a perfectly-conducting cylinder.

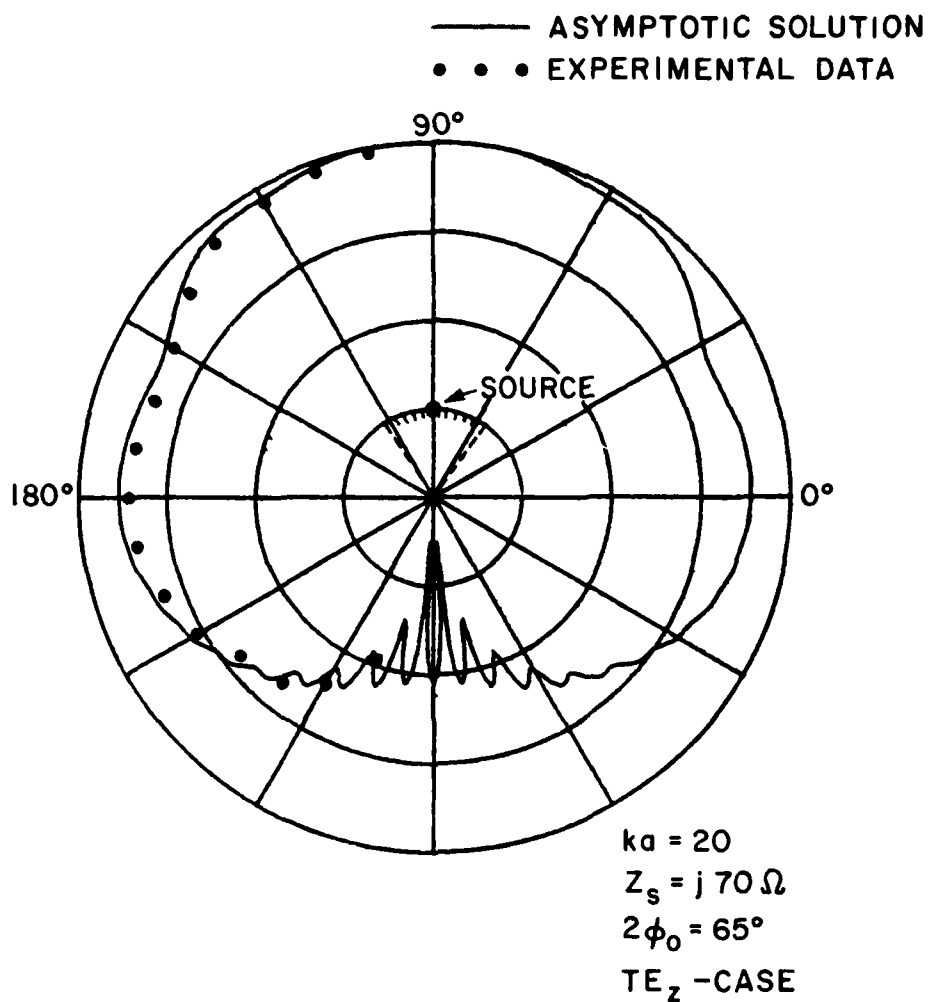


Figure 23--Radiation patterns of a magnetic line source on perfectly-conducting circular cylinder which is partly covered with an impedance surface patch.

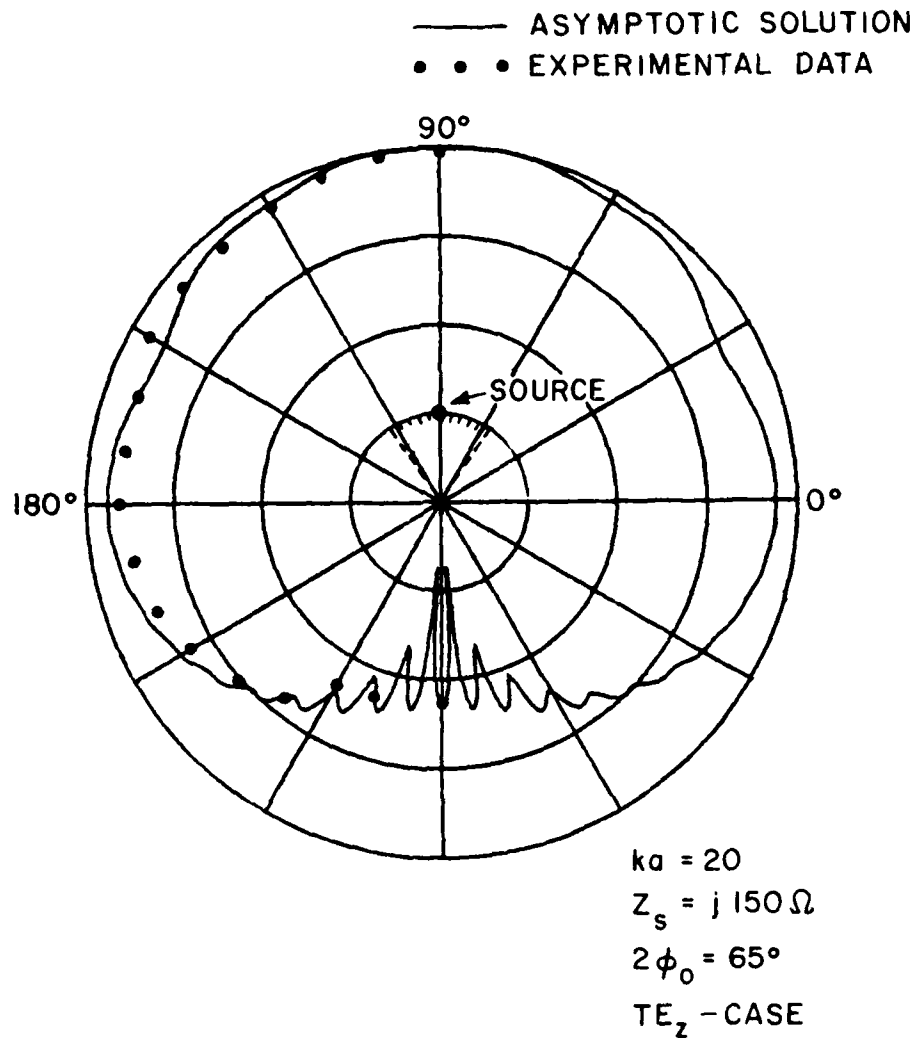


Figure 24--Radiation patterns of a magnetic line source on perfectly-conducting circular cylinder which is partly covered with an impedance surface patch.

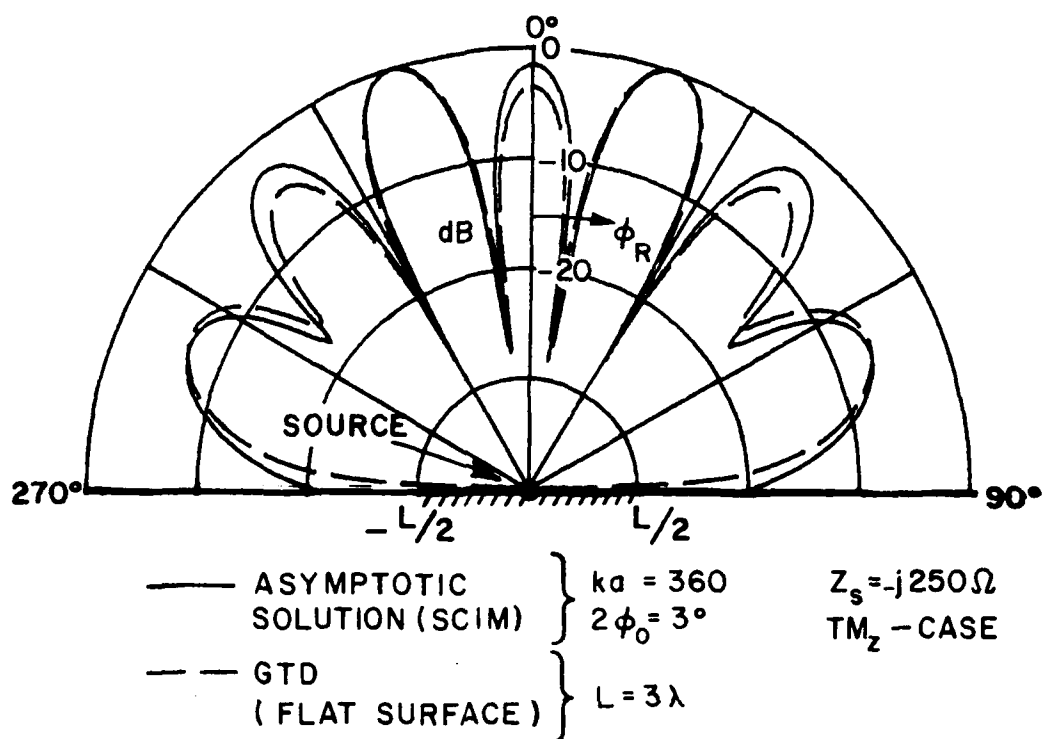


Figure 25--Radiation patterns of a magnetic line dipole source on perfectly-conducting planar and circular cylindrical surfaces which are partly covered with an impedance surface patch.

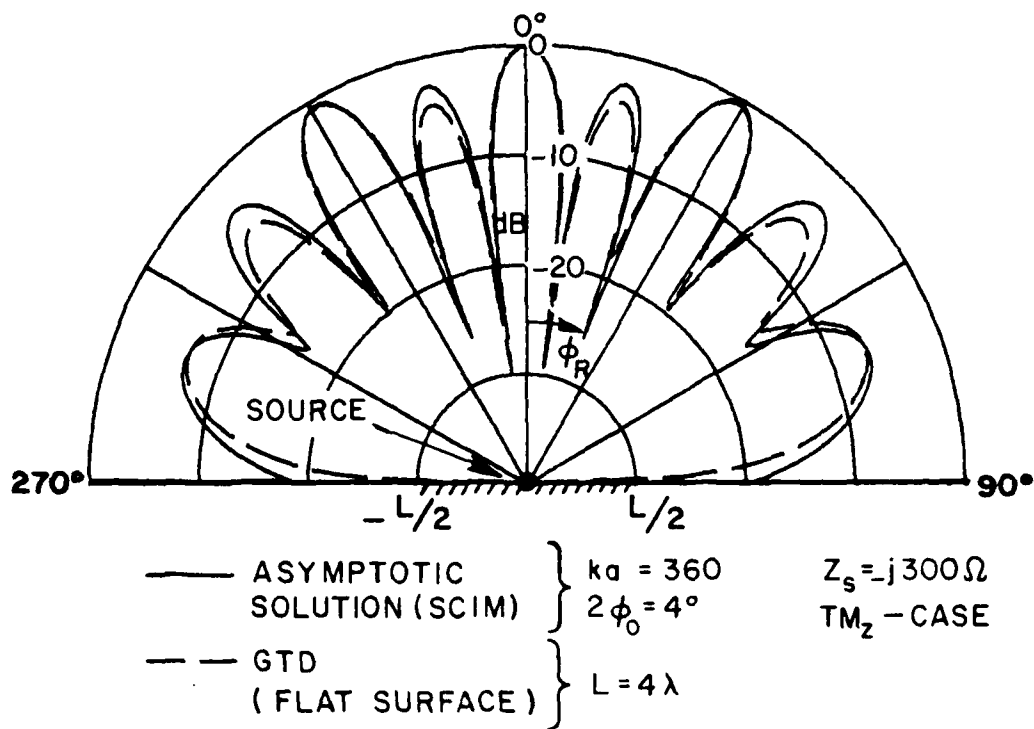


Figure 26--Radiation patterns of a magnetic line dipole source on perfectly-conducting planar and circular cylindrical surfaces which are partly covered with an impedance surface patch.

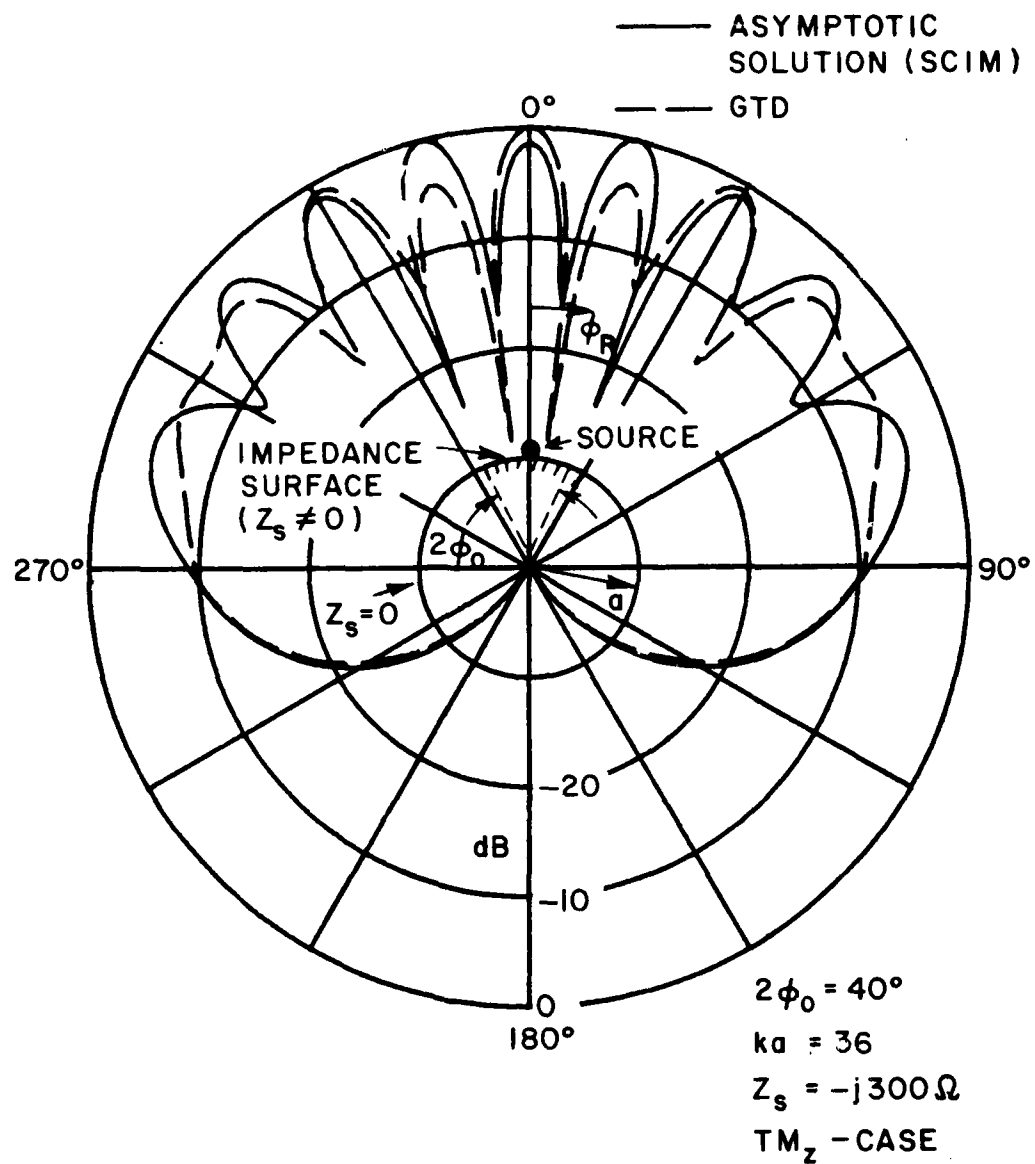


Figure 27--Radiation patterns of a magnetic line dipole source on perfectly-conducting circular cylinder which is partly covered with an impedance surface patch.

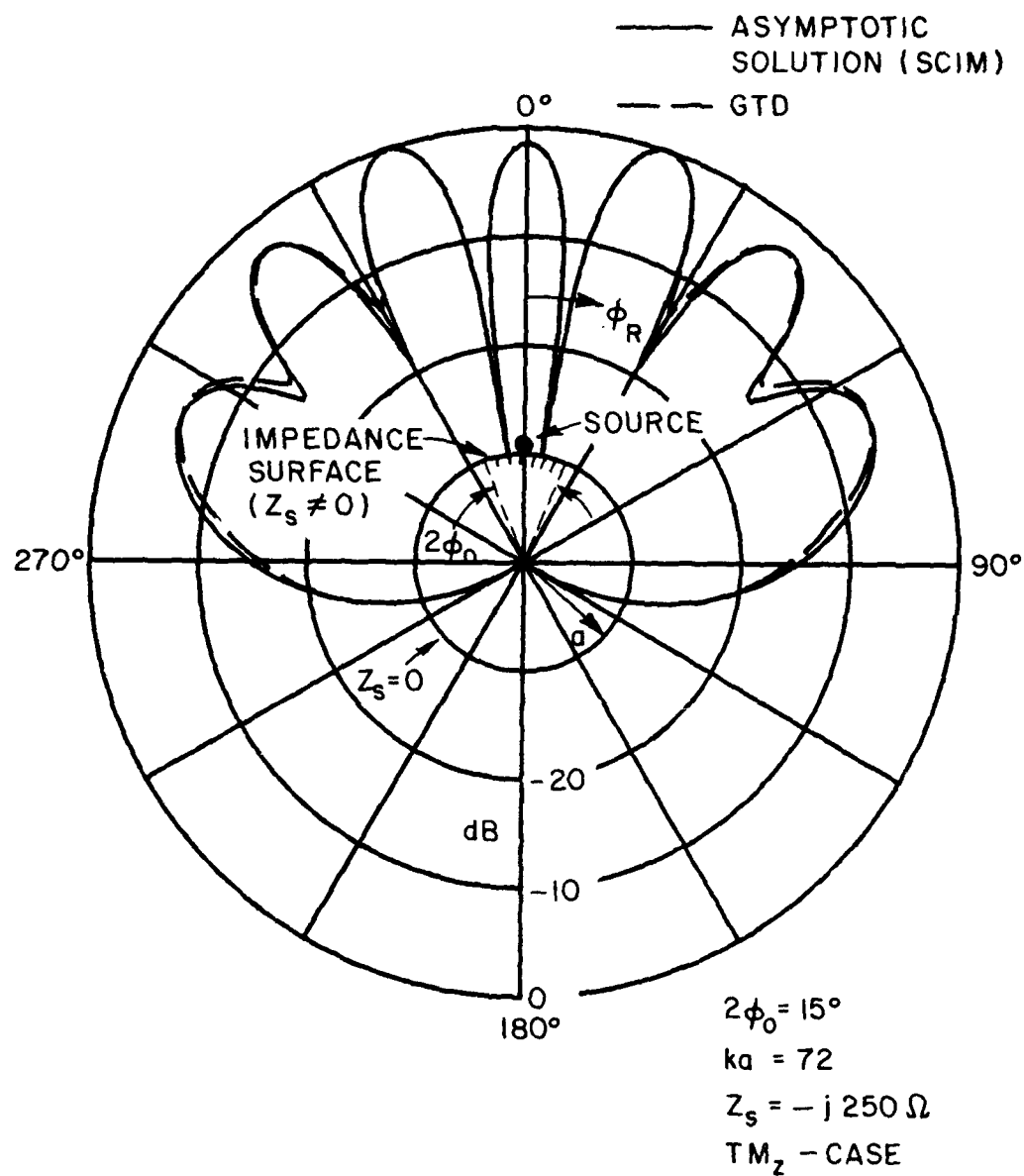


Figure 28--Radiation patterns of a magnetic line dipole source on perfectly-conducting circular cylinder which is partly covered with an impedance surface patch.

Table I

| GTD (as in Reference 4) | MM-GTD (as in Reference 2) | SCIM |
|---|---|--|
| Uniform impedance surface must support an Elliot mode | General impedance surface | Uniform Impedance surface |
| Leakage from the impedance surface is not included | It can handle the leakage from the impedance surface | It can handle the leakage from the impedance surface |
| Both the TE_z and TM_z cases can be handled easily | It is very difficult to handle the TM_z case | Both the TE_z and TM_z cases can be handled easily |
| Numerically very fast | Numerically slower than the other two | Numerically rather fast |
| Physically appealing | Physically not as appealing as the other two | Physically appealing |
| The precise form of the surface fields in the vicinity of the source and the edges of the patch is not required | A prior knowledge of the surface fields is not required | An accurate description of the fields on the entire surface of the impedance patch is required |

It is observed from these comparisons that the asymptotic solution (SCIM) indeed agrees very well with the other independent methods of analysis.

In the following paragraphs, the bounds for the asymptotic analysis (SCIM) are studied. The basic parameters of interest occurring in the SCIM are: (a) the distance from the source to the edge of the patch, (b) the radius of the cylinder, and (c) the value of the surface impedance. The range of these parameters over which the SCIM remains accurate have been established in an approximate fashion after an extensive numerical study. In particular, for a given value of impedance and the cylinder radius, there is a maximum patch size beyond which the asymptotic representation used in the SCIM for the currents on the impedance surface are strictly not valid. As indicated previously in Chapter II, the surface current on the impedance patch is assumed to consist partly of the Elliot mode or surface wave type component which propagates from the source to the edge of the patch, and secondly it consists of the component which is termed as the non-surface wave component, since the latter is the only current which propagates to the edge of the patch if the impedance surface can not support an Elliot mode field. Thirdly, there is a reflected component of the current to account for the reflections of the current incident on the edges of the patch. Also, as pointed out earlier this reflected component of the current is assumed to be produced by the Elliot mode field or surface wave component which impinges on the edge of the patch. A few typical plots of the magnitudes of the equivalent magnetic surface current densities which exist on an impedance patch located on a perfectly conducting circular cylinder are illustrated in Figures 29 through 34. The current densities ($\hat{z} \times \hat{n} \times \vec{H}(\vec{Q}|\vec{Q}')$) of (16a) for the TE_z-case and $\hat{n} \times \vec{E}_p(\vec{Q}|\vec{Q}')$ of (16b) for the TM_z-case) are plotted as a function of the arc-length, $t = a|\phi|/\lambda$, measured from the source placed at the center of the impedance patch where $\lambda = 2\pi/k$ and $|\phi|$ is the angle between the source point and the observation point on the impedance patch. As can be seen from these typical current plots, the amplitude of the non-surface wave component of the current begins to grow beyond a certain maximum distance, $t_m/2$ from the source. The non-surface wave current approximation is not expected to be accurate beyond the immediate neighborhood of this distance, $t_m/2$. For the TE_z-case, an empirical equation can be found relating the maximum total patch size, t_m (as defined above and measured in wavelengths; i.e., $2a|\phi|/\lambda$) to the magnitude of the normalized impedance, $|z_s| = |Z_p/Z_0|$, and the normalized radius of the cylinder, ka . For the asymptotic forms of the currents which are given in section IIB to order $1/(ka)^2$, such an empirical equation has the following form:

$$ka = [|z_s| + 0.04] (3.1 t_m^2 - 2.6 t_m + 2.8) + 3.6. \quad (40)$$

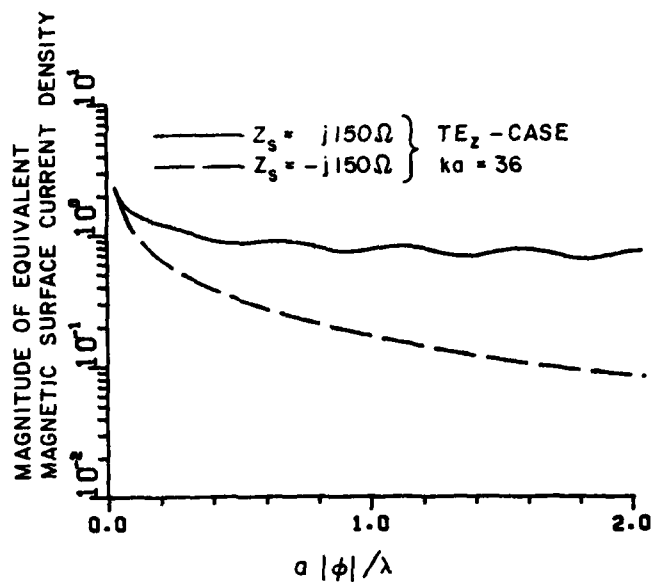


Figure 29--Magnitude of the equivalent magnetic current density on an impedance patch (which partly covers a circular cylinder) as a function of the arclength measured from the source. $R_h = 0.071/14^\circ$.

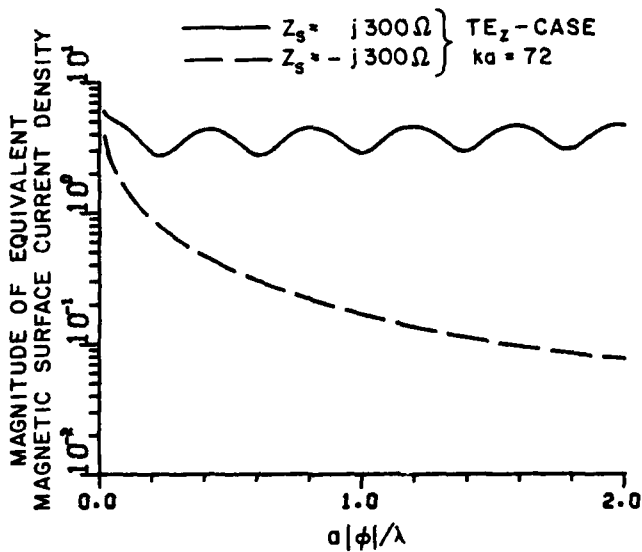


Figure 30--Magnitude of the equivalent magnetic current density on an impedance patch (which partly covers a circular cylinder) as a function of the arclength measured from the source. $R_h = 0.2173/24^\circ$.

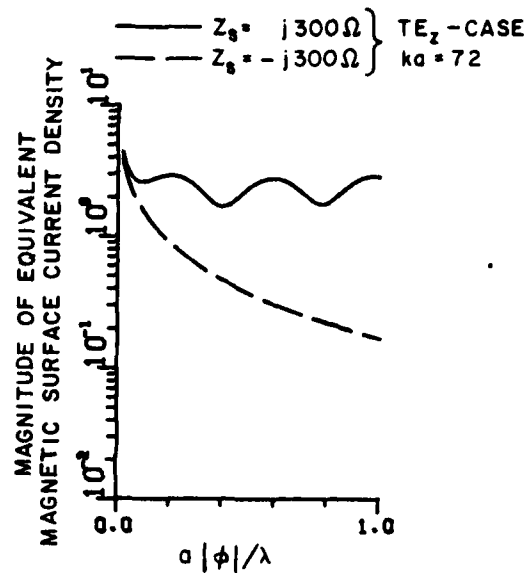


Figure 31--Magnitude of the equivalent magnetic current density on an impedance patch (which partly covers a circular cylinder) as a function of the arclength measured from the source. $R_h = 0.2173/24^\circ$.

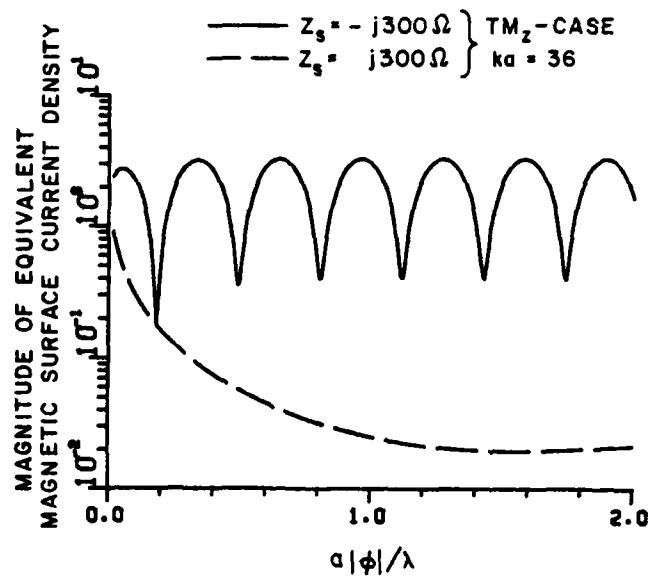


Figure 32--Magnitude of the equivalent magnetic current density on an impedance patch (which partly covers a circular cylinder) as a function of the arclength measured from the source. $R_s = 0.7825/121^\circ$.

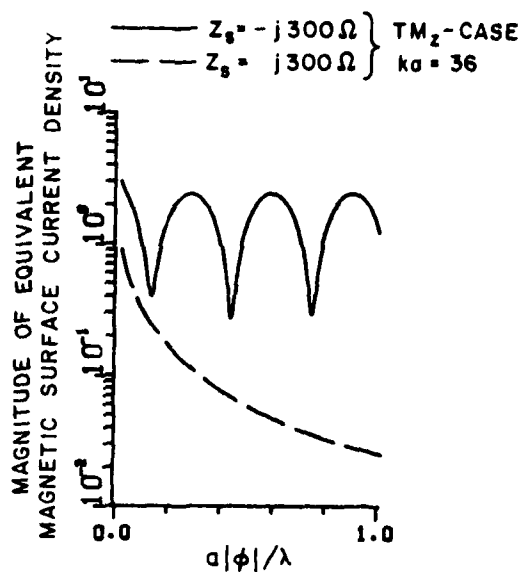


Figure 33--Magnitude of the equivalent magnetic current density on an impedance patch (which partly covers a circular cylinder) as a function of the arclength measured from the source. $R_s = 0.7825/121^\circ$.

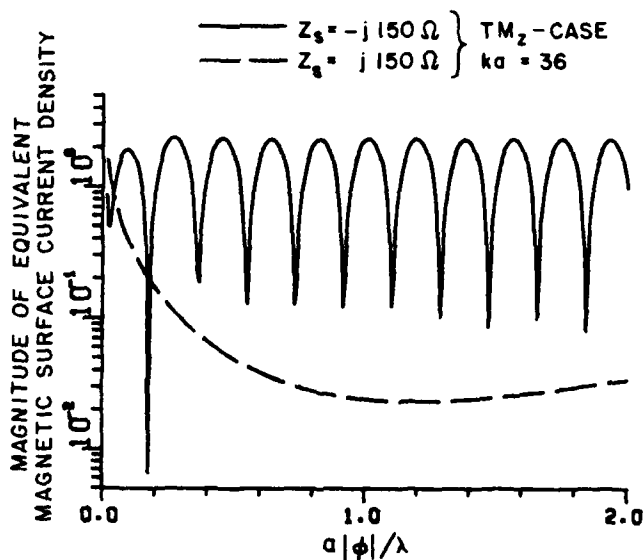


Figure 34--Magnitude of the equivalent magnetic current density on an impedance patch (which partly covers a circular cylinder) as a function of the arclength measured from the source. $R_s = 0.9292/129^\circ$.

In Figure 35, Equation (40) is compared with the data obtained from SCIM.

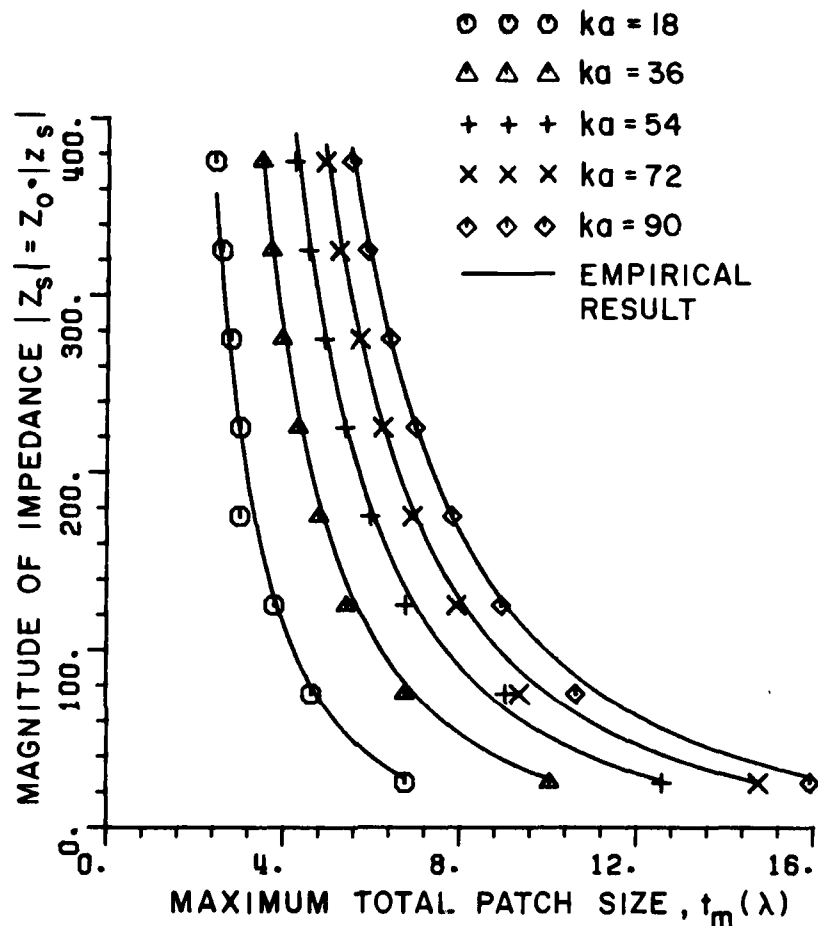


Figure 35--The maximum total patch size beyond which the asymptotic form of the currents in (17a) and (18a) may not be trusted.

The surface current incident on the edge of the impedance for the TM_z case of (15) is very similar in character to the corresponding TE_z case. The only essential difference between these two cases is that the z_s in the TE_z case is replaced by $y_s = Y/Y_0$ in the TM_z case. Thus, $S(40)$ may be used for TM_z case of (15) by simply replacing z_s by y_s .

It is noted that, (40) is a very conservative upper bound for both the TE_z and the TM_z cases. This is particularly true for the type of impedances which can allow an Elliot type of surface wave mode to exist, since this is the dominant component of the current and furthermore it remains valid even for distances larger than $t_m/2$. Figures, presented in (12) through (28), indicate that it is possible to obtain good agreement between the SCIM and other independent methods for patch sizes well beyond those allowed by (40). Typically, it is in general possible to treat half patch widths of the order of t_m with good accuracy.

For impedance patches which are larger than the limiting size indicated above, one should use the asymptotic form of the currents given in (17a) and (18a) up to t_m and then switch to the creeping wave representation for the currents which is explained in parts (IC) and (IIC) of Appendix B, for the TE_z and TM_z cases, respectively.

The component of the current reflected from the edges of the impedance patch is calculated by simply multiplying the incident Elliot mode field with a surface wave reflection coefficient R_b which characterizes the discontinuity in the impedance at the edges. This quantity, R_b is found in [4] via the solution to the problem of the surface wave diffraction by a two part planar, impedance surface. Multiple reflections between the edges of the patch are then summed in a self consistent manner as explained in section IIB. Plots of R_h (corresponding to TE_z case) and R_v (corresponding to TM_z case) are illustrated in Figures 6 and 7, respectively as a function of the surface reactance which is normalized to the free space impedance. It is noted from these plots that R_v is significantly higher than R_h for values of the normalized reactance which are less than unity. Consequently, the component of the current reflected from the edges of the impedance patch is expected to play a significant role in the radiation pattern calculations for the TM_z case.

In general, the SCIM is not expected to be accurate for the case when the magnitude of the reflection coefficient $|R_s|$ approaches unity. However, as mentioned at the end of section IIB, this is not a serious restriction on the SCIM since an antenna with such a large reflection coefficient is not desirable. Under the present assumption, the dominant reflected component of the current is produced by the incident Elliot mode field. In order for this assumption to hold, one requires that the size of the impedance patch be sufficiently large. From an extensive numerical study, it has been approximately determined that this minimum impedance patch length for the case when the impedance surface supports an Elliot mode field is $\pi/2\beta$ where β for both the TE_z and TM_z cases defined in (19g) and (20d) respectively. This study

basically indicates how far the edge of the patch has to be to lie outside the "effective source regions" where the component of the currents propagating away from the source are usually large (due to the singularity at the source). It is noted that $\pi/2\beta$ is generally very small compared to t , so that the current approximation employed in SCIM is indeed valid.

CHAPTER IV RELATION OF RADIATION PATTERN PROPERTIES TO THE PERTINENT PARAMETERS OF THE PROBLEM

In this chapter the dependence of the radiation patterns on certain parameters is discussed. It is observed that the number of lobes in the radiation pattern within the lit region is a function of the width of the impedance patch and the value of the impedance. For the TM_z case with a capacitive impedance patch, this number is primarily governed by the width of the impedance patch measured in wavelength, λ (where as before $\lambda=2\pi/k$). A simple ray picture of the GTD may be employed to explain why the number of the lobes in the lit region depends primarily on the impedance patch length. In this picture, the principle source and the edges of the impedance patch may be considered as three line sources. For the TM_z case, these line sources have similar pattern factors. Hence a simple array analysis indicates that the number of lobes in the radiation pattern within the lit region is approximately given by the following table.

Table 2

| Width of the impedance patch (in λ) | Approximate number of lobes in the TM_z radiation pattern (lit region) |
|--|--|
| Less than 0.5 | 1 |
| 0.5-1.5 | 3 |
| 1.5-2.5 | 5 |
| 2.5-3.5 | 7 |
| 3.5-4.5 | 9 |

Table 2 is in full agreement with the observed radiation patterns for the TM_z -case. Having a peak in the broadside direction (i.e., $\phi_R=0^\circ$) is a characteristic feature of this case.

For the TE_z case, with an inductive impedance patch, it is difficult to relate the number of lobes in the lit region to just the impedance patch length via a simple array analysis because the pattern factor of the principle source located at the center of the patch is different from the pattern factors of the equivalent sources of the fields diffracted from the edges at Q_1 and Q_2 . In general for the TE_z -case there may be a peak or a null in the broadside direction ($\phi_R=0^\circ$) and the number of lobes increases

with an increase in the patch length. Smooth radiation patterns with single lobe can be obtained for the TM_z -case with an inductive surface, and the TE_z -case with a capacitive² surface. It is also interesting to point out that there are lobes in the deep shadow region of the radiation pattern. These lobes are created by the diffraction of the waves that creep around the conducting portion of the cylinder, and the number of lobes in the deep shadow region depends on the radius of the cylinder rather than the impedance patch length. The number of lobes in the shadow region increases as the radius of the cylinder becomes larger; however, the level of the fields in that shadow region decreases considerably with an increase in the cylinder size to the point where the strength of these lobes is negligible in comparison to the fields in the lit region.

The reflection coefficient, R_s , can be used as a gauge for the lobe sizes, i.e., the ratio between the lobe maxima and minima. For values of $|R_s| < 0.9$ which is the region of interest in this work, the lobe size in the lit region reduces as the magnitude of the reflection coefficient decreases. In other words, antenna structures with high R_s leads to a larger break up in the radiation patterns; this aspect will be discussed further at the end of this chapter.

Additional useful information about the radiation pattern can be obtained if one studies the behavior of the far field pattern of the antenna at specific observation angles; namely $\phi_R = 0$ and $\phi_R = 90$ as a function of the value of the surface impedance, and also separately as a function of the length of the impedance patch. In Figures 36 through 41 the magnitude of the field $u(0)$ at $\phi_R = 0$, and likewise $u(90)$ at $\phi_R = 90$ are plotted in dB for both the TE_z and the TM_z cases. The magnitude of $u(90)$ in dB for the relevant unperturbed geometries (perfectly conducting cylinders without any impedance patch) are also included in these plots for comparison. The plots are normalized such that $|u(0)|$ for the unperturbed geometry is taken as zero dB.

A striking conclusion one draws from these data is that, for the TM_z case with a capacitive impedance patch, there are very sharp maximums which are spaced every half electric wavelength, $\lambda_z/2$. In such resonances, one may realize up to 15 dB increase in the magnitude of the field in the end fire direction ($\phi_R = 90$) over that which would exist for the unperturbed geometry. The TE_z case with an inductive impedance patch also exhibits an increase in the field strength in the end fire direction compared to that of the unperturbed geometry. However, the sharp resonances of the TM_z case do not appear to be present in the TE_z case. Some typical radiation patterns for the TE_z and TM_z cases are presented

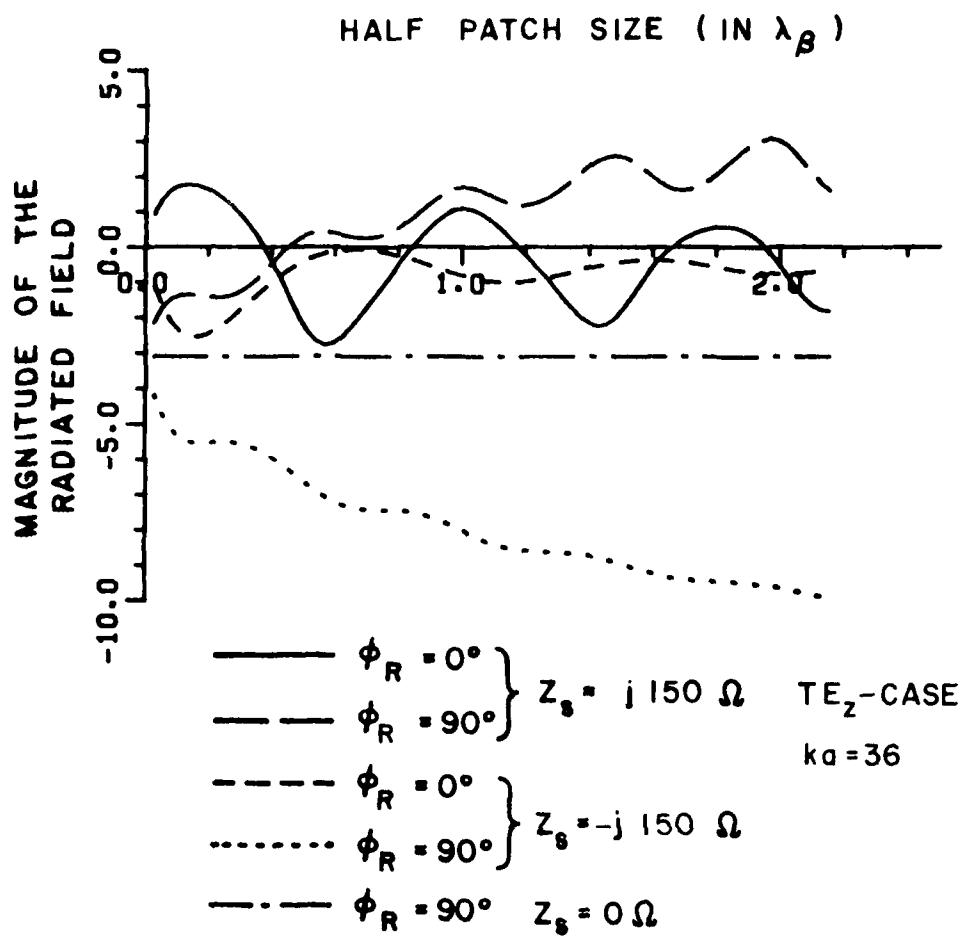


Figure 36--The magnitude of the radiation field of a line source (illustrated in Figure 10) as a function of the half patch size, $a\phi_p/\lambda_h$.

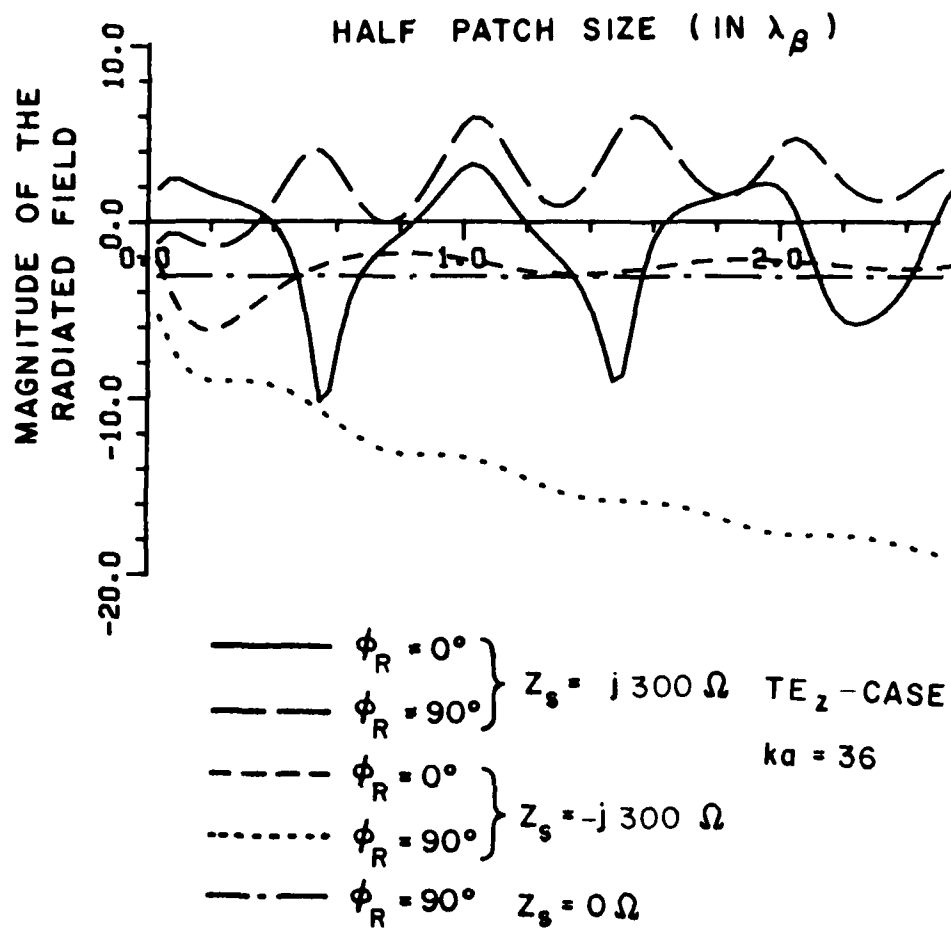


Figure 37--The magnitude of the radiation field of a line source (illustrated in Figure 10) as a function of the half patch size, $a\phi_p/\lambda_h$.

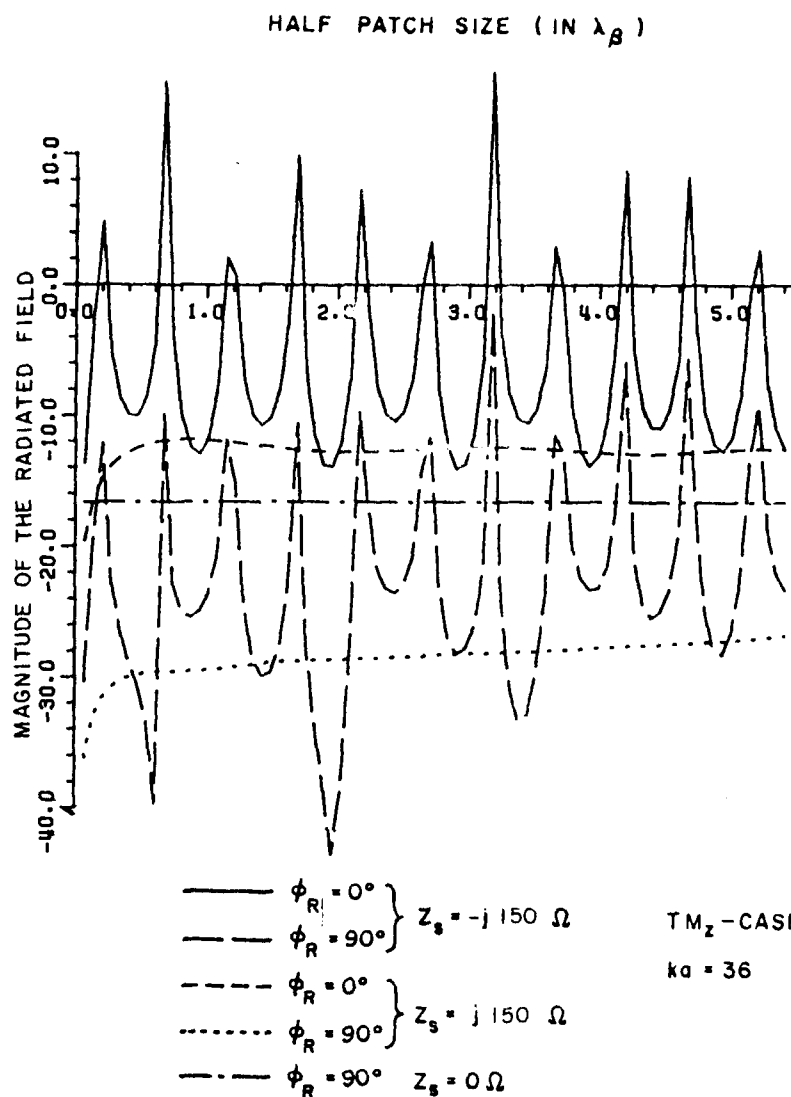


Figure 38--The magnitude of the radiation field of a line dipole source (illustrated in Figure 10) as a function of the half patch size, $a\phi_p/\lambda_h$.

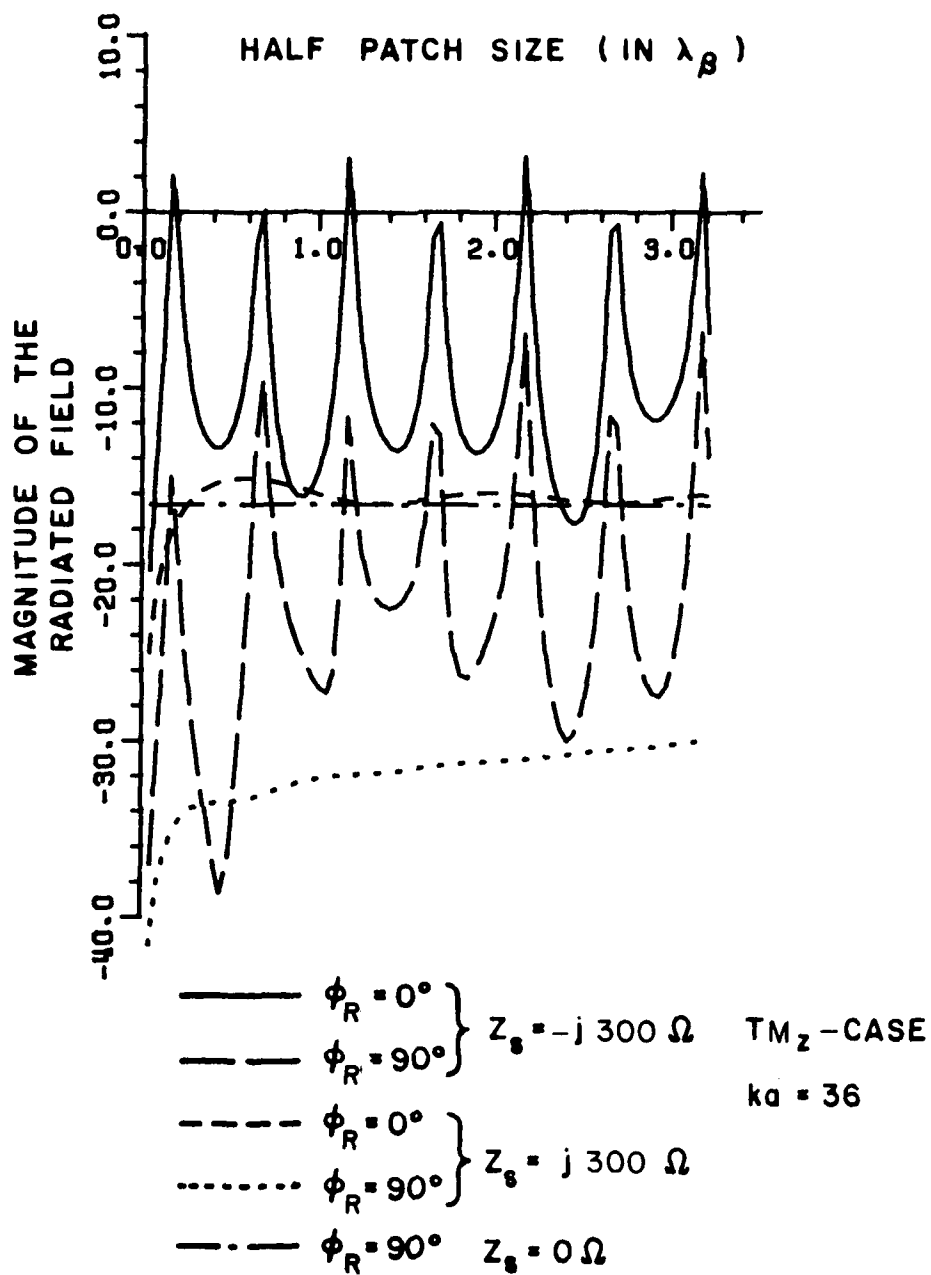


Figure 39--The magnitude of the radiation field of a line dipole source (illustrated in Figure 10) as a function of the half patch size, $a\phi_p/\lambda_h$.

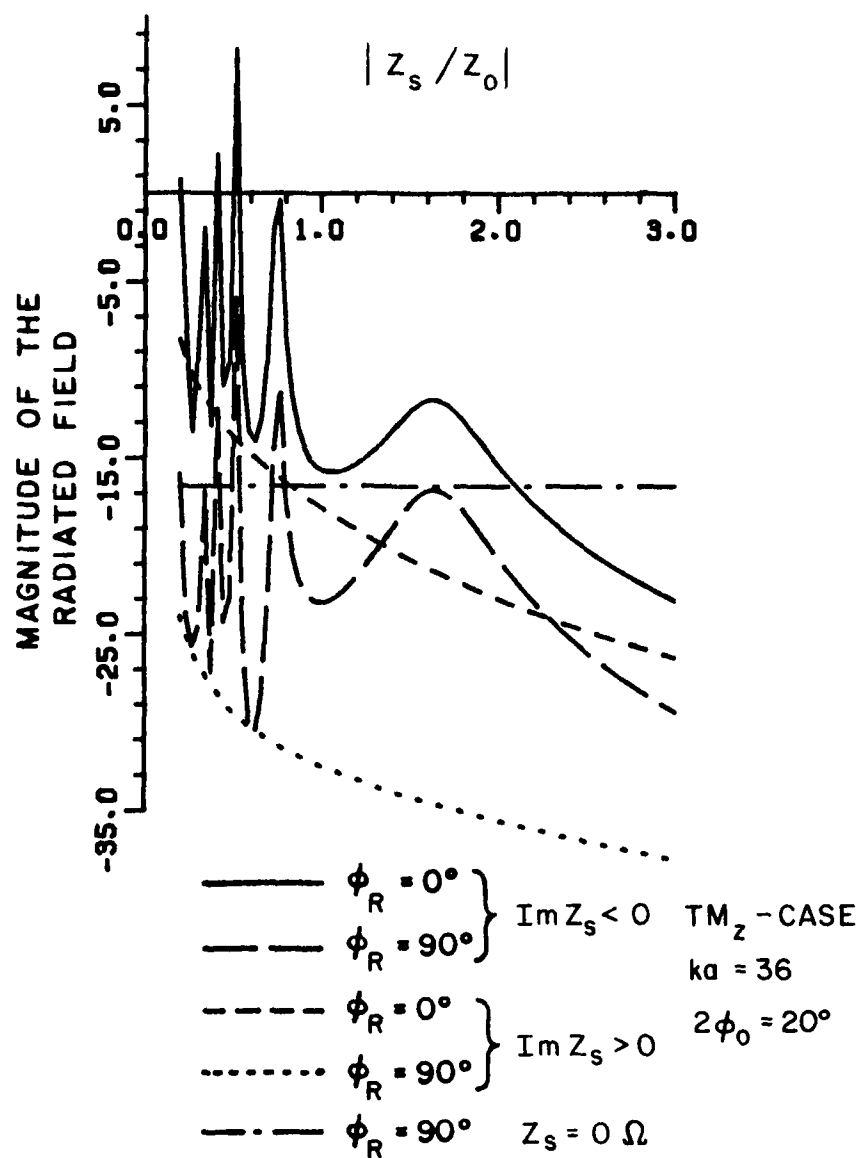


Figure 40--The magnitude of the radiation field of a line dipole source (illustrated in Figure 10) as a function of the normalized surface impedance.

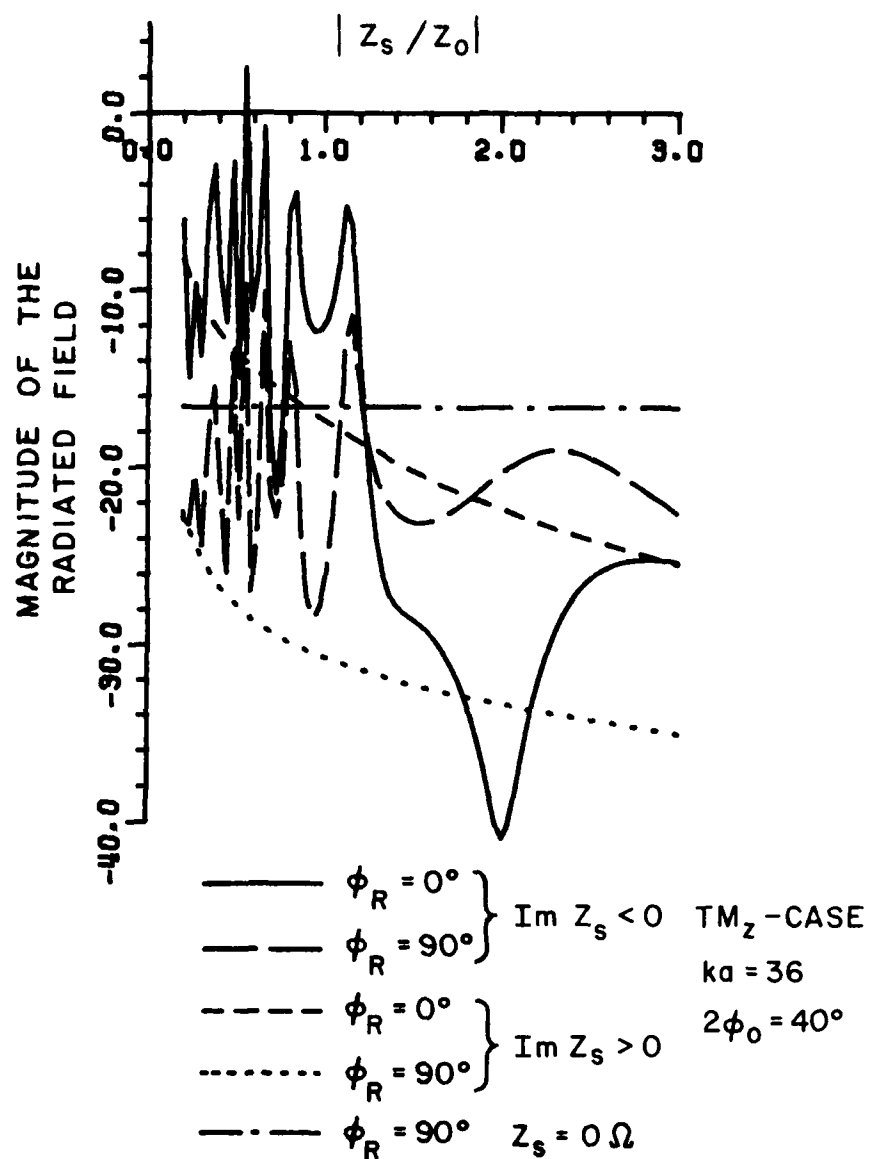


Figure 41--The magnitude of the radiation field of a line dipole source (illustrated in Figure 10) as a function of the normalized surface impedance.

in Figures 42 through 45 for both the capacitive and the inductive type of impedances as well as for the case when there is no impedance patch (unperturbed geometry). The plots are normalized such that their respective maximums are taken as zero dB.

Finally, one may point out that the value of the surface impedance may be different or it may be the same for different orientations of the sources. An example for the first type of surface may be a thin material of thickness, d , relative permittivity, ϵ_r , and relative permeability, μ_r placed on a perfectly conducting surface. From the flat surface geometry, it can be shown that [23], the equivalent surface impedance for the TE_z and TM_z cases are given as follows:

$$Z_s = j \frac{k}{V_h} Z_0 \quad \text{for } TE_z\text{-case} \quad (41a)$$

$$Z_s = -j \frac{V_s}{k} Z_0 \quad \text{for } TM_z\text{-case} \quad (41b)$$

where V_h is the solution of the following pair of equations

$$-ud \cdot \cotan(ud) = \mu_r V_h d \quad (42a)$$

$$(ud)^2 + (V_h d)^2 = (\epsilon_r - 1)(kd)^2 \quad (42b)$$

Similarly, V_s is obtained by solving the following equations simultaneously

$$ud \cdot \tan(ud) = \epsilon_r V_s d \quad (43a)$$

$$(ud)^2 + (V_s d)^2 = (\epsilon_r - 1)(kd)^2 \quad (43b)$$

A proper combination of d , ϵ_r and μ_r may be used to build a surface which can support Elliot type modes for both the TE_z and TM_z cases with desired surface wave propagation constants. Such a surface may be referred to as an "arbitrary polarization surface wave structure" [24]. In Figure 46, the radiation patterns of a magnetic line source and a magnetic line dipole source are presented. The source is assumed to be located on an impedance surface which appears as a capacitive surface ($Z_s = -j710$) for the TM_z -case and an inductive surface ($Z_s = j200$) for the TE_z -case, so that the surface wave propagation constants associated with both cases are the same (i.e., $\beta = \beta_s = \beta_0 = 1.13k$). The radiation patterns for $Z_s = j710$ and $Z_s = -j200$ for the TM_z and TE_z case, respectively, are also included in this figure for comparison. The plots are normalized to their respective peak values.

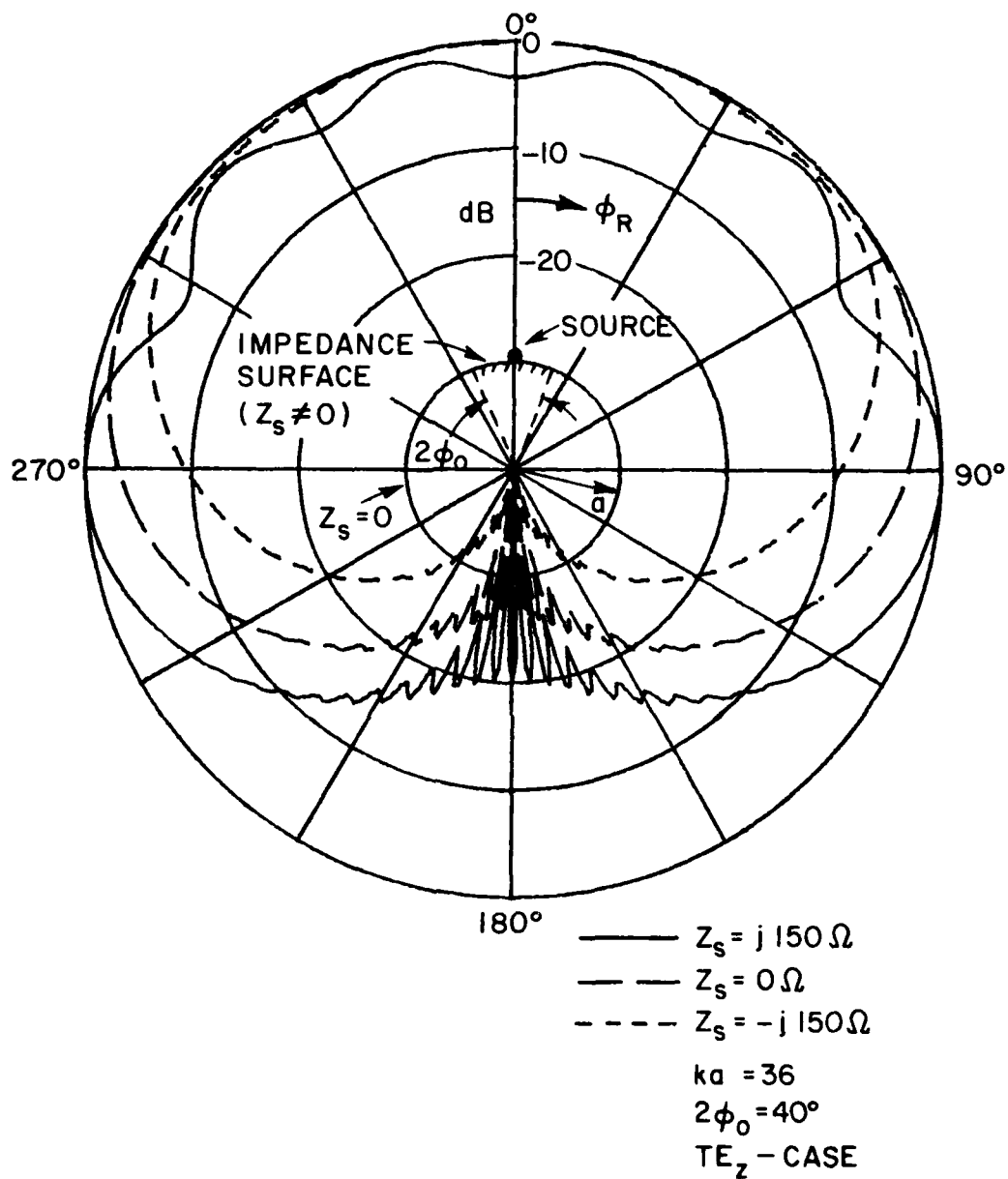


Figure 42--Radiation pattern of a magnetic line source on a perfectly-conducting cylinder which is partly covered with an impedance surface patch.

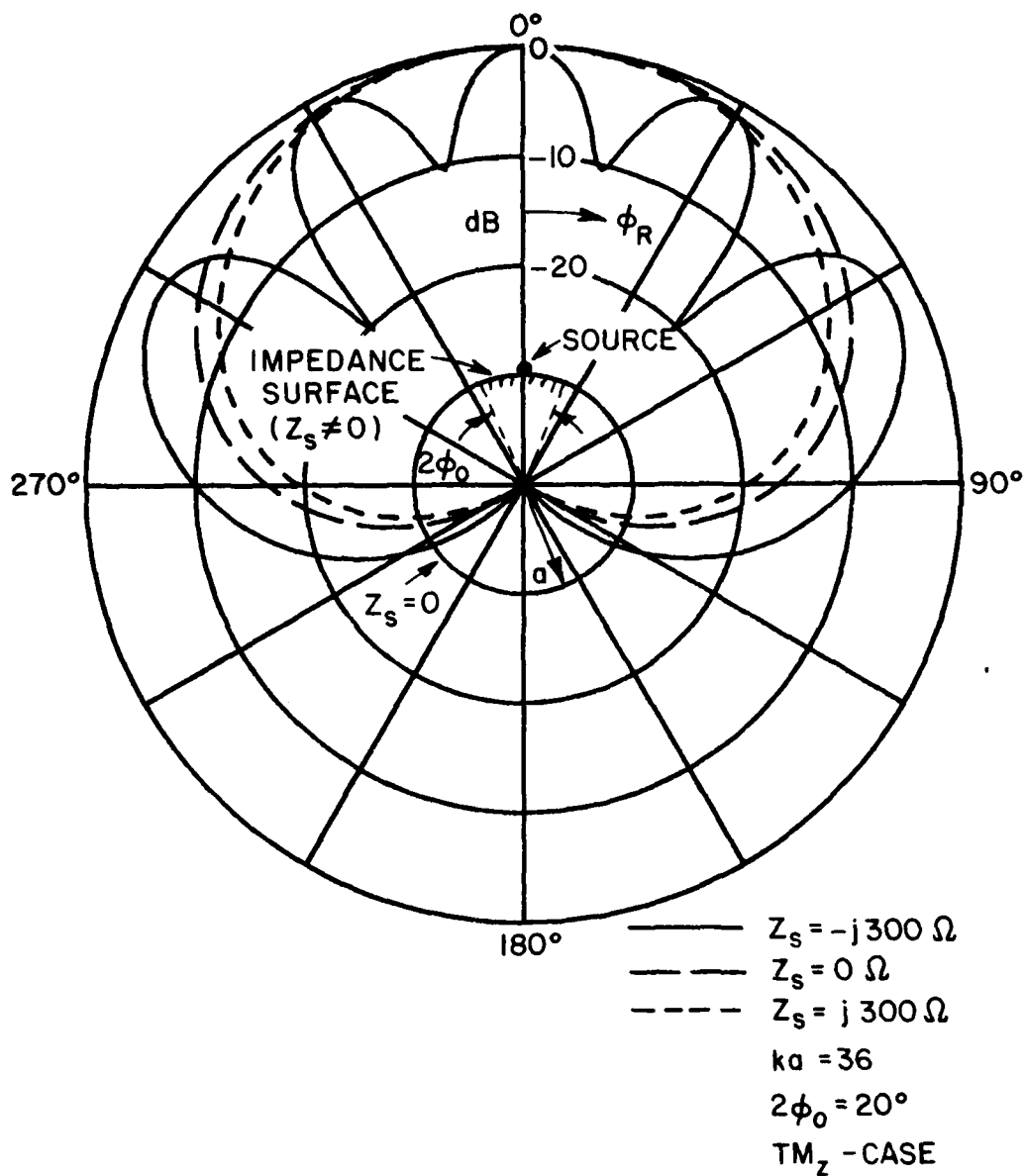


Figure 44--Radiation pattern of a magnetic line dipole source on a perfectly-conducting cylinder which is partly covered with an impedance surface patch.

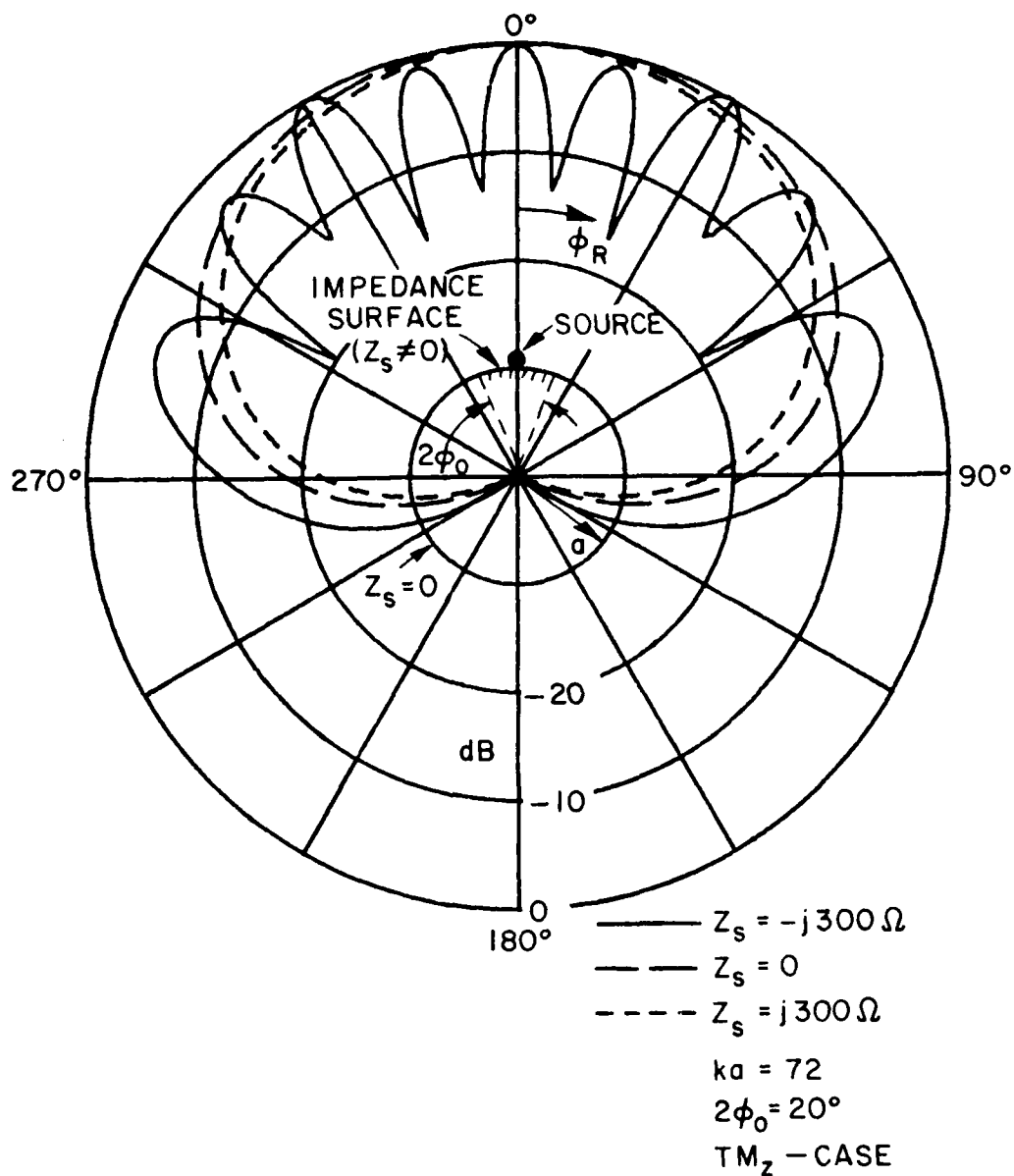
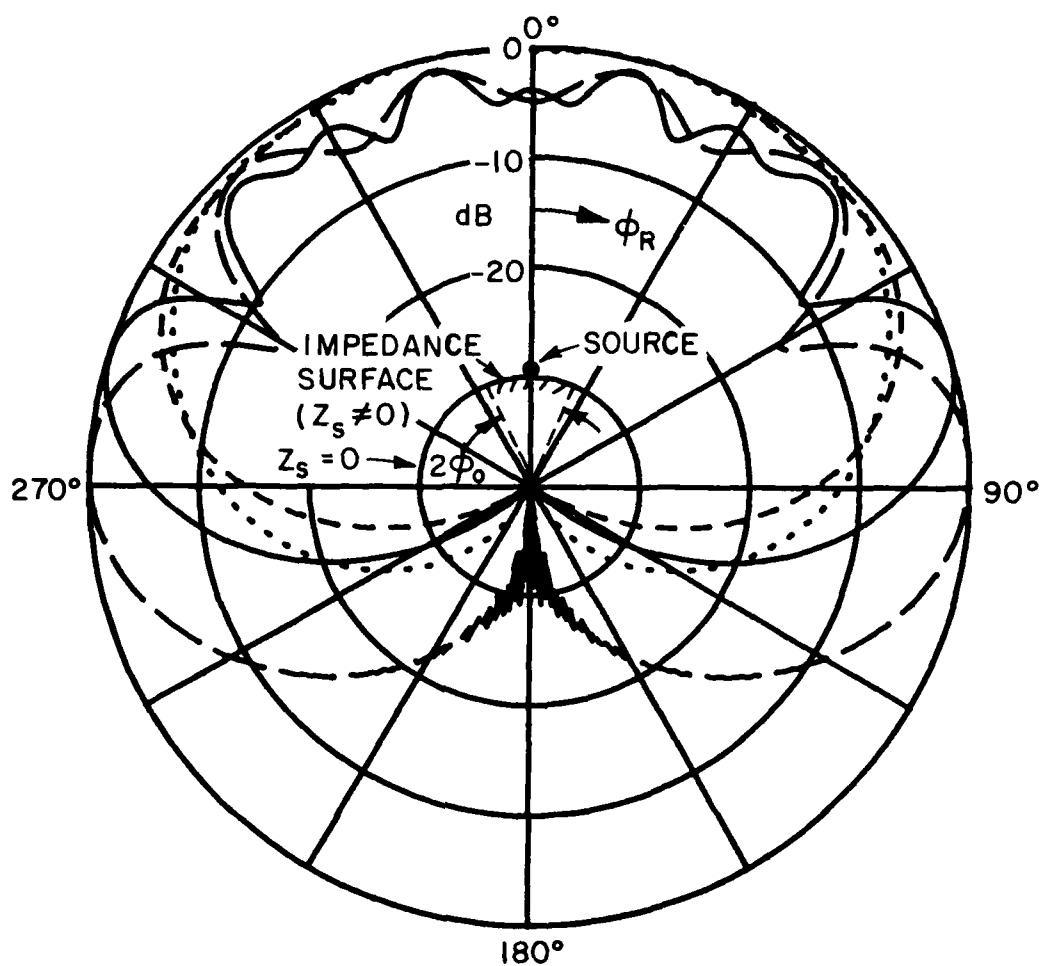


Figure 45--Radiation pattern of a magnetic line dipole source on a perfectly-conducting cylinder which is partly covered with an impedance surface patch.



| | | | |
|-----------|-----------------------|-----------------|-----------------------------------|
| — | $Z_s = -j 710 \Omega$ | } TM_z - CASE | $ka = 72$ $2\phi_0 = 20^\circ$ |
| - - - | $Z_s = j 710 \Omega$ | | |
| — | $Z_s = j 200 \Omega$ | } TE_z - CASE | $\beta_s = \beta_h = 1.13k$ |
| - - - - - | $Z_s = -j 200 \Omega$ | | |

Figure 46--Radiation pattern of a magnetic line source and magnetic line dipole source on a perfectly conducting circular cylinder which is partly covered with an impedance surface patch. The value of the impedance is assumed to depend on the type of the source.

In Figures 47 through 51, additional radiation patterns of a magnetic line dipole source (TM_z -case) are presented for values of the reflection coefficient, R_z^s , moderately small. It should be noted that, these patterns are much smoother than the ones presented in Chapter III. As indicated earlier, the radiation patterns in Chapter III for the TM_z case are included in this work only for comparison purposes.

As indicated earlier, the SCIM can be employed to analyze the radiation pattern of a source on a general convex cylinder. In Chapter II, the way to extend the circular cylinder results to an arbitrary convex cylinder is presented. In Figure 52, this procedure is used in order to obtain the radiation pattern of a magnetic line source located on an elliptic cylinder which is covered with an impedance surface patch.

In conclusion, the present analysis of the radiation from a line source on an impedance surface patch which partly covers a perfectly conducting convex cylinder indicates that for impedance surfaces which support an Elliot type mode, a moderate increase can be achieved in the radiation intensity near the horizon ($\phi_0 = 90^\circ$) over that which would exist in the absence of the impedance patch. In general, the radiation patterns associated with those impedance surfaces which support the Elliot mode are found to be rather sensitive to changes in the operating frequency. Furthermore, the increase in the radiation intensity near the horizon is accompanied by a ripple in the radiation pattern within the lit region. The addition of a small loss and/or taper to the impedance patch would decrease this ripple somewhat without seriously degrading the radiation intensity near the horizon. In particular, the field strength at the edges of the impedance patch can be controlled by a small loss, this in turn allows one to reduce the ripple size. The loss can be introduced to the solution as a perturbation to the lossless case via an exponential decay factor along the propagation path on the impedance surface. It is observed that the ripple size, besides being dependent on other parameters (such as patch length, radius of the cylinder) is also related to the magnitude of the reflection coefficient $|R_s|$. As a rough estimate, an average reduction of 8-2 dB in the ripple size can be achieved upon reducing the magnitude of the reflection coefficient by 0.2 in the region $0.5 < |R_s| < 0.9$; whereas, it is possible to smooth out the ripples by 4-2 dB with a decrease in the magnitude of the reflection coefficient by 0.2 in the region $|R_s| < 0.5$. For the TM_z -case, the average ripple size at $|R_s| = 0.7$ and $|R_s| = 0.9$ is 8 dB and 18 dB, respectively. Similarly, for the TE_z -case, the average ripple size at $|R_h| = 0.1$ and $|R_h| = 0.3$ is 8 dB and 12 dB, respectively. It may be possible to reduce the reflection coefficient by tapering the impedance patch without drastically changing the actual antenna structure, thereby reducing the ripple size in the radiation pattern within the lit region.

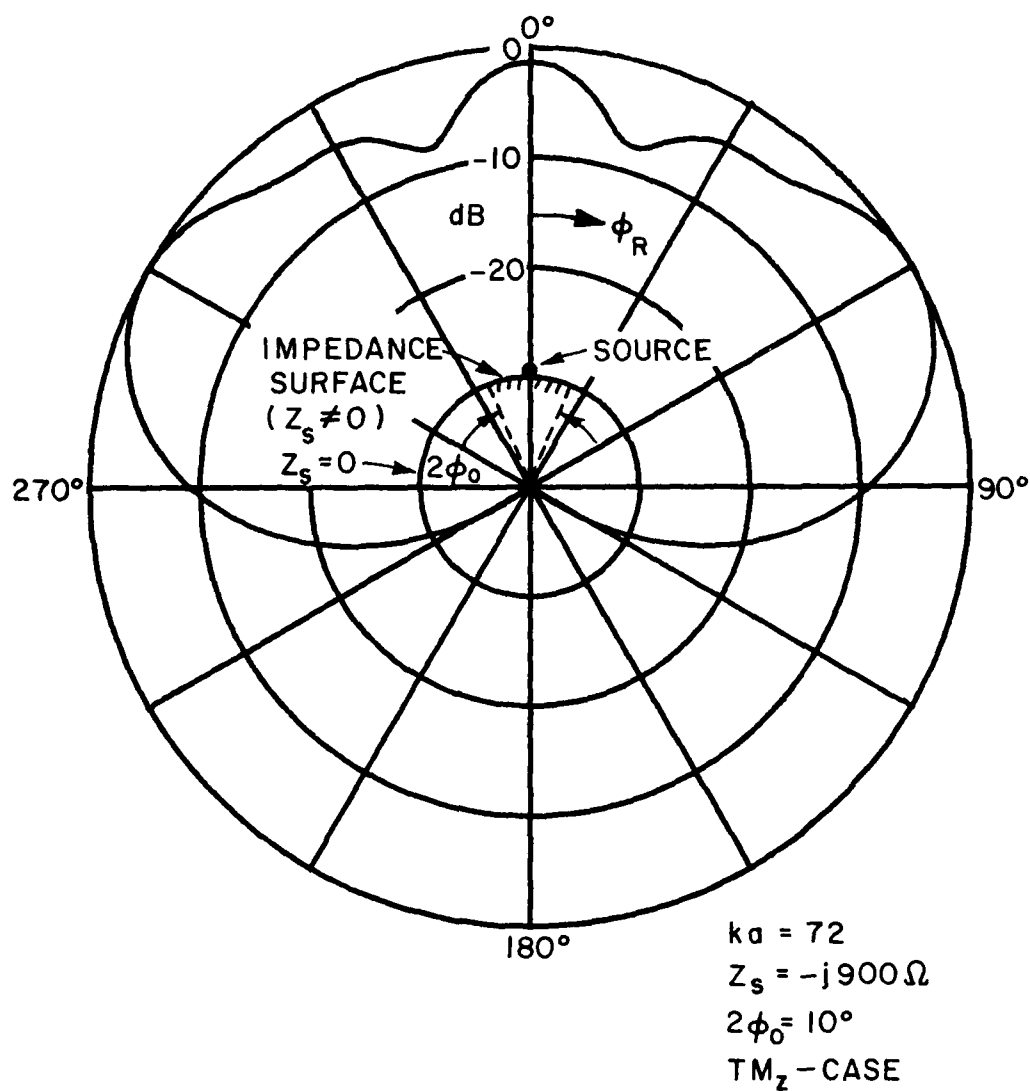


Figure 47--Radiation pattern of a magnetic line dipole source on a perfectly-conducting circular cylinder which is partly covered with an impedance surface patch.

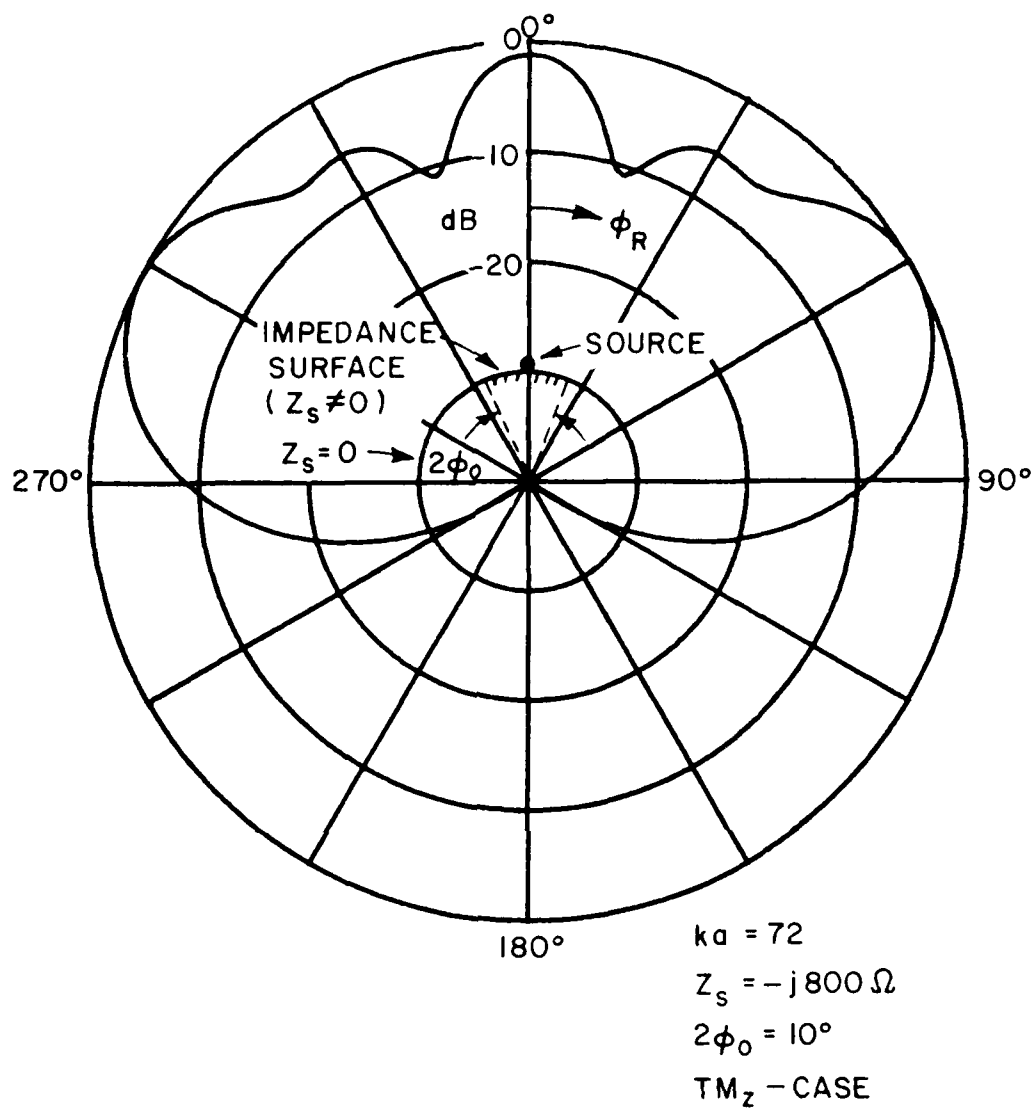


Figure 48--Radiation pattern of a magnetic line dipole source on a perfectly-conducting circular cylinder which is partly covered with an impedance surface patch.

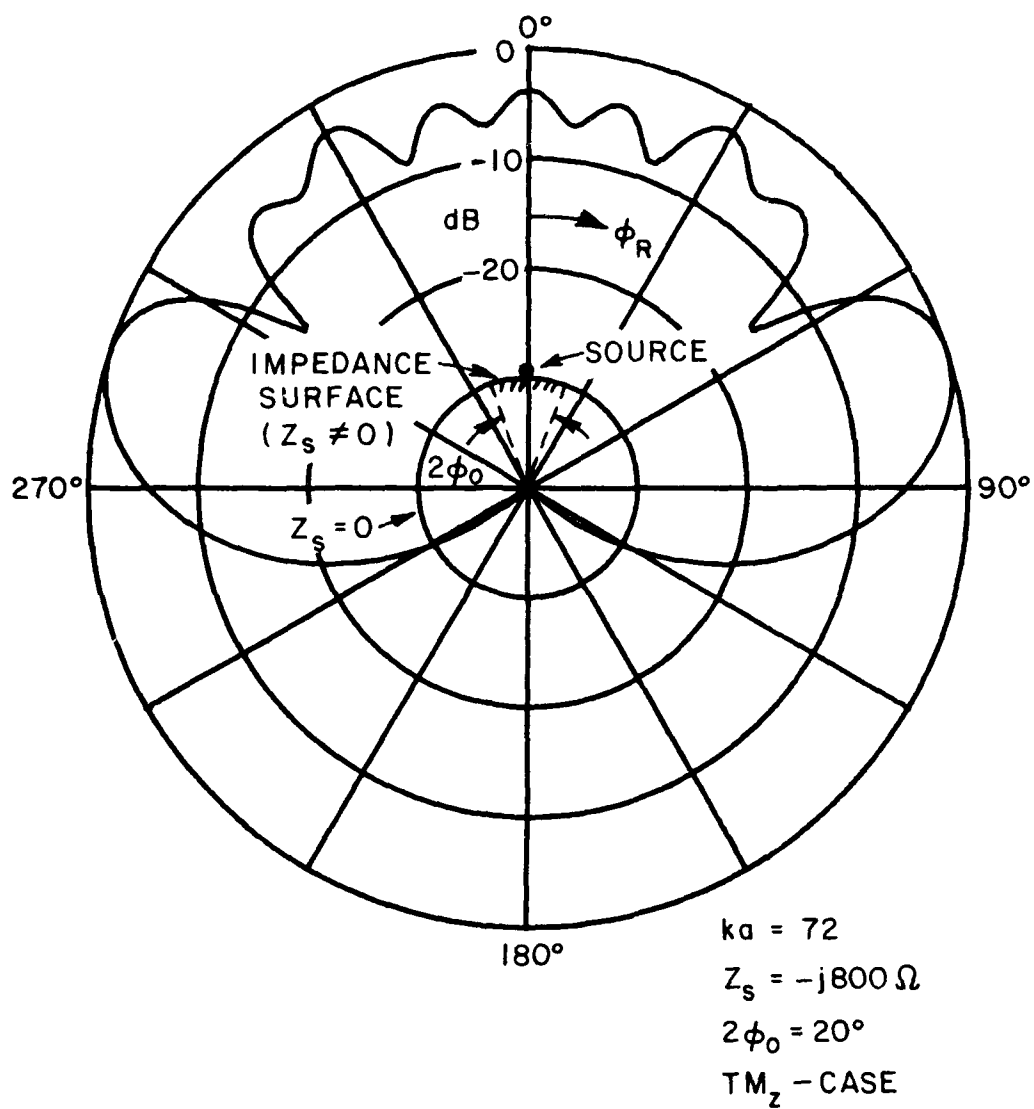


Figure 49--Radiation pattern of a magnetic line dipole source on a perfectly-conducting circular cylinder which is partly covered with an impedance surface patch.

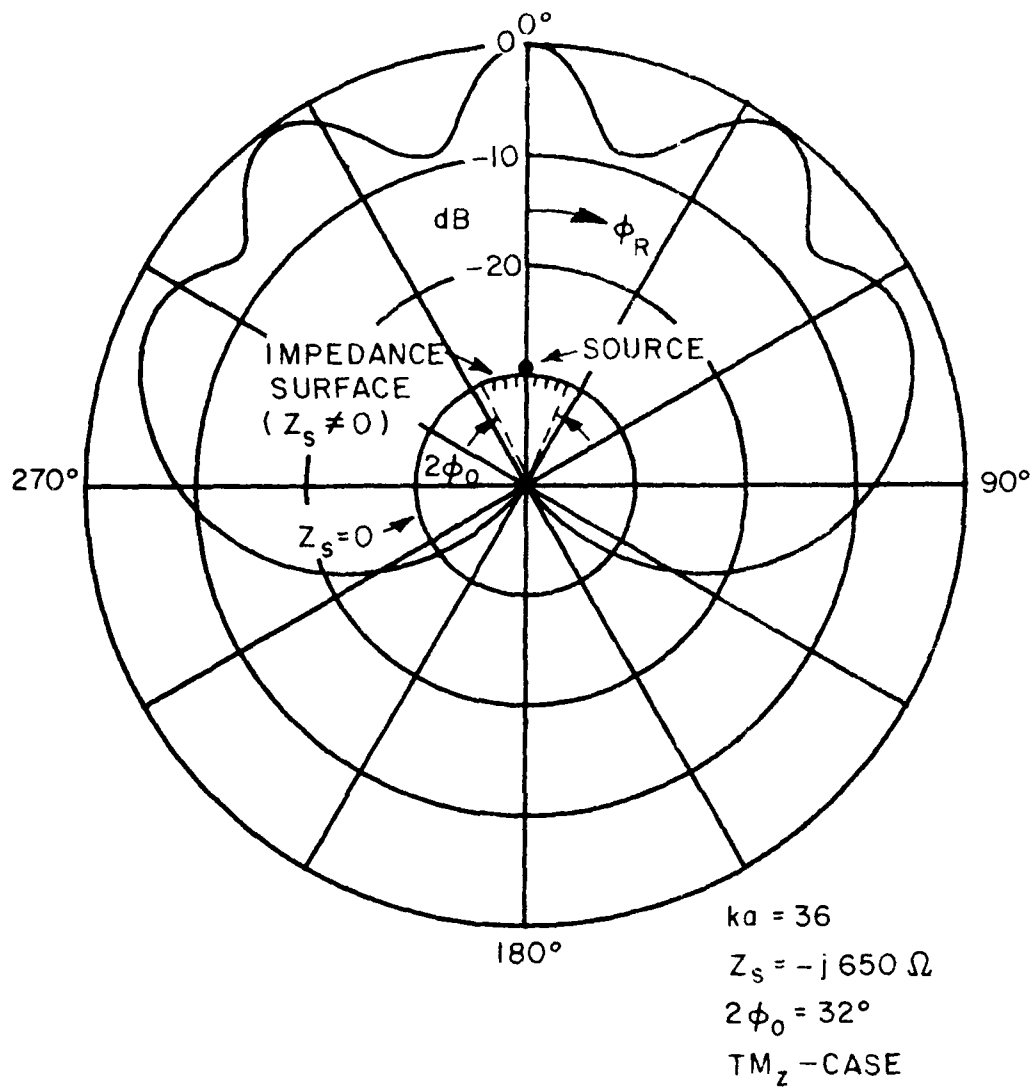


Figure 50--Radiation pattern of a magnetic line dipole source on a perfectly-conducting circular cylinder which is partly covered with an impedance surface patch.

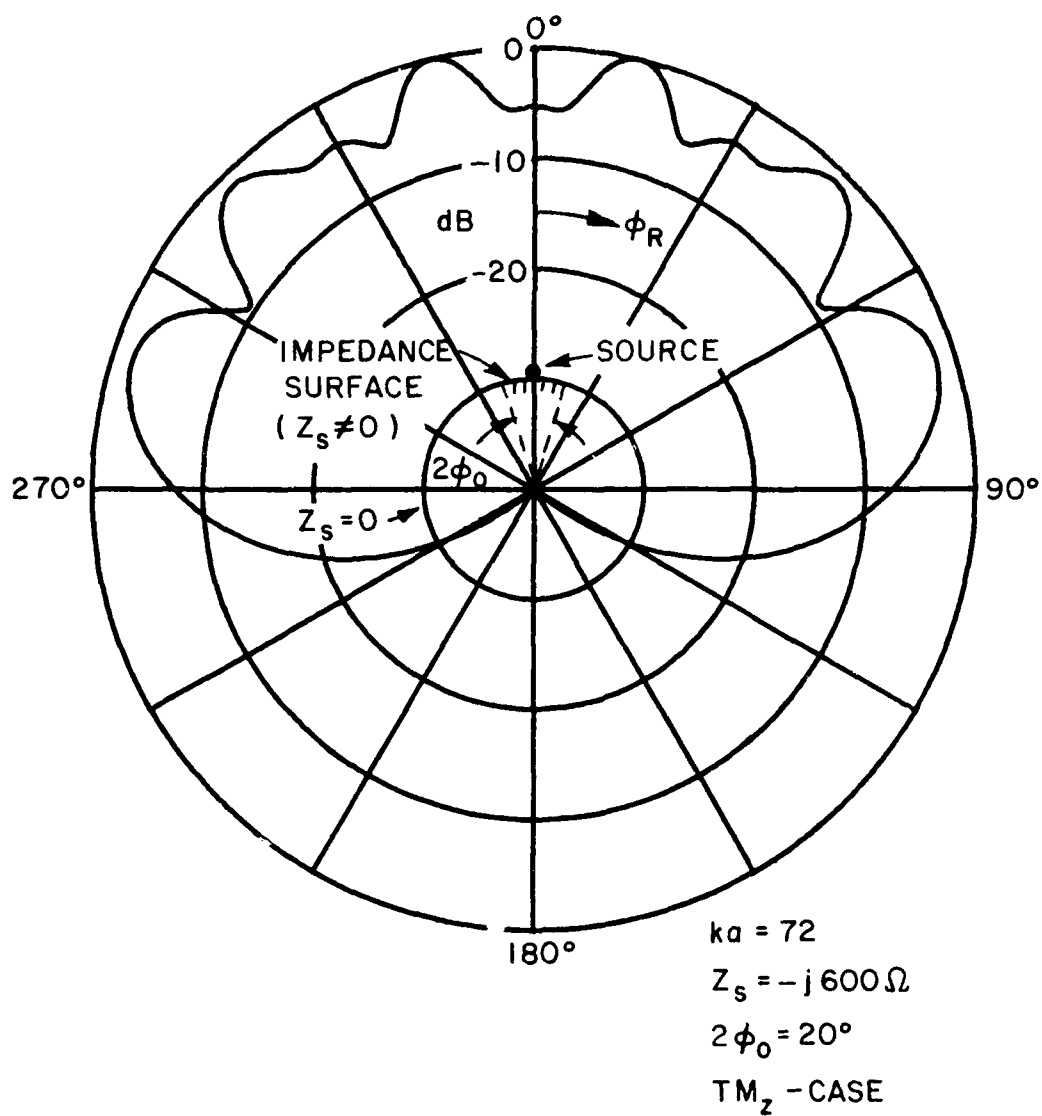


Figure 51--Radiation pattern of a magnetic line dipole source on a perfectly-conducting circular cylinder which is partly covered with an impedance surface patch.

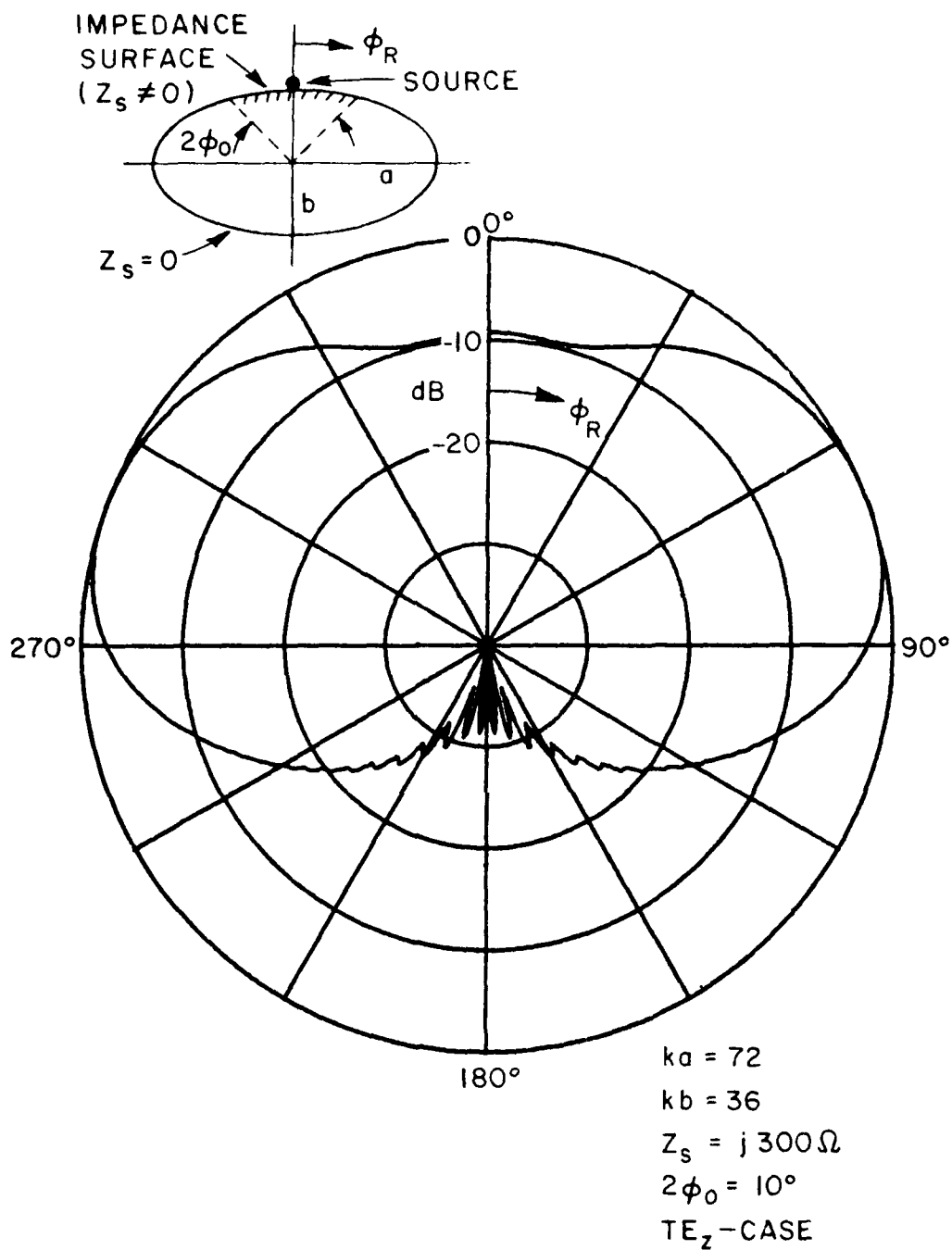


Figure 52--Radiation pattern of a magnetic line source on a perfectly-conducting elliptic cylinder which is partly covered with an impedance surface patch.

The present analysis based on the SCIM constitutes an extension and improvement over the earlier GTD analysis [2] which was restricted to only those impedance surfaces which support an Elliot type mode and for which the Elliot mode propagates with negligible leakage on the curved impedance patch. These limitations of the GTD solution are absent in the SCIM. While the SCIM in it's present form appears to be quite accurate in it's fairly broad regions of validity, further work is recommended to remove some of the minor restrictions which currently exist (as outlined earlier) and also make this solution applicable to a wider class of problems than the one treated here.

CHAPTER V CONCLUSIONS

A high frequency solution is developed for predicting the radiation patterns of sources on a perfectly conducting convex cylinder which is partly covered by an impedance surface patch. It is expected that this study will be useful to the design of an aircraft antenna which can be made to radiate strongly in the vicinity of the horizon by impedance loading. Such an antenna structure excited by a crossed slot on an aircraft fuselage can find applications for satellite communications. Thus, it is important to develop a theoretical model for this type of an antenna in order to gain a better understanding of the effect of the impedance loading on its radiation pattern. It is also interesting to point out that this theoretical model may be useful in the design of antennas which will radiate strongly only in the broadside direction and shed little energy in the horizon and in the shadow region of the antenna.

The surface impedance concept is an approximation for certain types of surfaces, such as thin dielectric layers, corrugated surfaces, slightly rough surfaces, and imperfectly conducting surfaces. The value of this equivalent surface impedance associated with these surfaces may depend on the orientations of the source. It is pointed out earlier that the arbitrary polarization surface wave structure could be an example for this type of impedance surfaces.

The analysis of the two dimensional (2-D) problem of the radiation by a magnetic line source (TE_z case) and a magnetic line dipole source (TM_z case) on a perfectly conducting circular cylinder partly covered with an impedance surface patch is employed in this work to simulate the 3-D crossed slot configuration. It is noted that the radiation pattern of the 3-D configuration would be the same as the one for the simpler 2-D case in the roll plane containing the slots, provided the effect of the wings are ignored. The basic approach applied here for the solution of the 2-D problem is called the surface current integration method (SCIM). The SCIM is an important extension and generalization of some of the earlier solutions based on the Geometrical Theory of Diffraction (GTD) and the hybrid moment method (MM)-GTD technique for analyzing this problem. The previous GTD solution was restricted to those

types of impedances which support an Elliot type mode for a given source orientation; whereas, the SCIM can be used for an arbitrary uniform impedance surface for both the TE_z and the TM_z cases. The MM-GTD solution obtained previously for the TE_z case is sufficiently general (includes non-uniform impedance surfaces) and is accurate; however, the SCIM leads to a far simpler and more efficient solution. On the other hand the MM-GTD solution for the TM_z case contains integrals which are very difficult to evaluate numerically; whereas, in the SCIM, the TM_z case can be handled as easily as the TE_z case.

In the SCIM, one integrates the equivalent surface current densities on the impedance patch in conjunction with an accurate, asymptotic form of the perfectly conducting, convex cylinder Green's function. The relations between the far field radiation pattern of the sources and these integrals are obtained via a generalized reaction theorem as explained in section IIA. The form of the equivalent surface current densities are found from the canonical problems of Appendix B. In these canonical problems for the TE_z and the TM_z cases, it is assumed that the cylinder is completely covered by an impedance surface. The finite length of the impedance patch is, then, introduced later into the solution by a self-consistent procedure for summing up the fields reflected from the edges of the patch as presented in section IIB.

The SCIM can also be used in the solution of crossed-slot antennas located on an arbitrary polarization surface wave structure as long as the coupling between the TE_z and TM_z surface wave (or Elliot) modes is negligible at the edge² of the structure so that the performance of each of the antennas can be analyzed independently as in the ordinary, single valued impedance surface case and these results can then be superimposed to yield the total radiation pattern.

The effect of the different parameters on the radiation pattern for both the TM_z and the TE_z cases can be summarized as follows:

TM_z Case:

- 1) The capacitive impedance surface (i.e., $Z_s = -j|x_c|$ where x_c is a real number) supports an Elliot mode field^s for this polarization; hence, it is possible for this case to guide more energy into the end fire direction ($\phi_p = 90^\circ$) i.e., near the horizon. It is observed for the Elliot mode case that the antenna patterns become increasingly frequency sensitive for those values of $Z_s = -j|x_c|$ for which $|x_c|$ is small.

2) The Elliot mode reflection coefficient, R_s , approaches unity as the capacitive impedance surface tends to the perfectly conducting case (i.e., as $|x_c|$ becomes small). Antenna structures with high reflection coefficients generate badly broken radiation patterns with deep ripples.

3) An inductive impedance surface does not support an Elliot mode, hence the field strength in the vicinity of the horizon is much lower than that obtained with a capacitive impedance surface.

4) In the case of the capacitive impedance patch, the number of lobes within the lit region increases as the width of the patch increases.

5) Inductive impedance patches generate smooth radiation patterns.

TE_z Case:

1) The inductive impedance surface ($Z_s = j|x_L|$) supports an Elliot mode field for this polarization. An increase in the field strength near the horizon is possible for this type of impedance.

2) The Elliot mode reflection coefficient, R_s , increases as the value of the inductive impedance increases. Hence, inductive impedance surfaces with small $|x_L|$ lead to smooth radiation patterns.

3) The capacitive impedance surface does not support an Elliot mode, hence the field strength in the endfire (horizon) direction is much lower than that obtained with an inductive impedance surface.

4) In the case of the inductive impedance patch, the number of lobes within the lit region increases as the width of the patch increases.

5) Capacitive impedance patches generate smooth radiation patterns.

APPENDIX A
AN ANALYSIS OF THE RADIATION FROM LINE SOURCES ON AN
INFINITE PLANAR IMPEDANCE SURFACE

In this appendix, the radiation from line sources on an infinite planar impedance surface is analyzed. The geometrical configuration of the problem is illustrated in Figure 53. Two different source orientations are discussed. The first of these is for the case of a z -directed magnetic line source excitation, which will henceforth be referred to as the TE_z case; this case is treated in Section I below. Likewise, the treatment of the case of an \hat{x} -directed magnetic line dipole source type excitation, which is henceforth designated as the TM_z case, is dealt with subsequently in Section II.

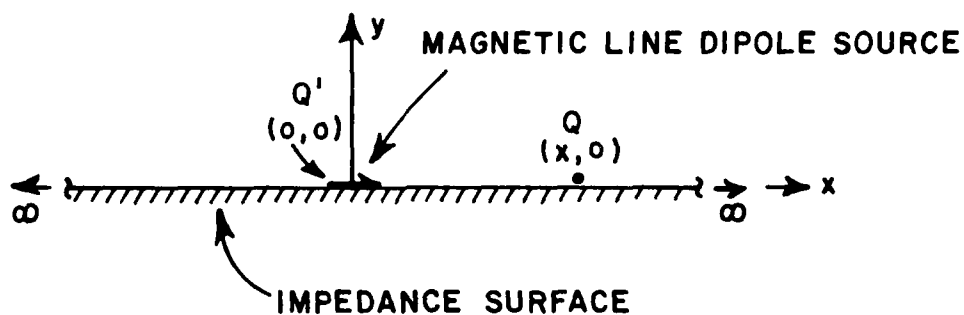
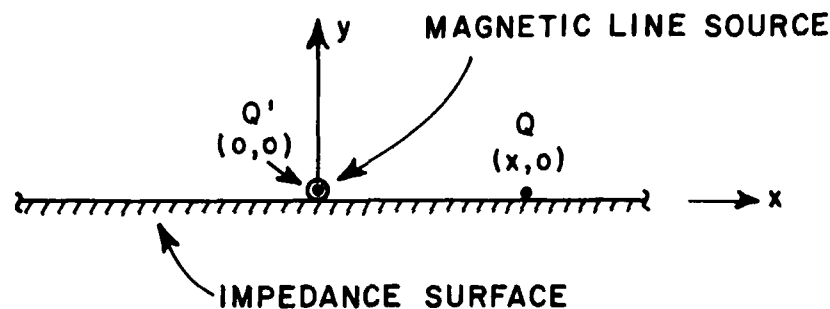


Figure 53--Geometry of the canonical problem of a line source on an infinite, planar impedance surface.

I. TE_z or Magnetic Line Source Excitation Case

The magnetic source density for this polarization is denoted by \bar{M} ; it is given by

$$\bar{M} = \hat{z} M \delta(x) \delta(y) \quad (A-1)$$

where M is the strength of the source and is assumed known. The magnetic field generated by such a source has only a \hat{z} -component and it will be denoted by H_z . H_z satisfies the reduced, inhomogeneous wave equation, and the following boundary conditions:

$$(\nabla_t^2 + k^2)H_z = jkY_0 M \delta(x) \delta(y); \quad y \geq 0, |x| < \infty \quad (A-2)$$

$$\frac{\partial H_z}{\partial n} + \alpha_h H_z = 0 \quad \text{at } y = 0 \quad (A-3)$$

where

$$\alpha_h = -jk \frac{Z_s}{Z_0} \quad (A-4)$$

For the problem of interest, α_h is chosen to be a real number (i.e., $\text{Re } Z_s = 0$); however, the method of solution is applicable to complex α_h as well. The impedance boundary condition given in (A-3) can asymptotically be obtained from the more general form of the boundary condition given in (5a) with the aid of the Maxwell's equations. $Z_s = 1/Y_s$ is the surface impedance, $Z_0 = Y_0^{-1}$ is the free space impedance. ∇_t^2 is the two dimensional Laplacian operator. Also, H_z satisfies the radiation condition for an $e^{j\omega t}$ time dependence.

In the process of solving (A-2) one defines a two-dimensional Green's function, $G(x,y|x',y')$ such that

$$H_z(x,y) = -jkY_0 M G^h(x,y|0,0). \quad (A-5)$$

$G^h(x,y|x',y')$ is the solution of (A-2) for a $-\delta(x-x')\delta(y-y')$ type source term on the right. It also satisfies (A-3) and the radiation condition. Using the procedure for constructing higher dimensional Green's function as in [25], one obtains,

$$G^h(x,y|0,0) = \frac{1}{2\pi j} \int_{-\infty - j\epsilon}^{\infty - j\epsilon} \frac{e^{-j\sqrt{k^2 - k_x^2}y - jk_x|x|}}{(\sqrt{k^2 - k_x^2} + j\alpha_h)} dk_x, \quad (A-6)$$

where ϵ is a positive but otherwise arbitrarily small number. The proper k_x sheet associated with the integrand of (A-6) is one for which $\text{Im} \sqrt{k^2 - k_x^2} < 0$ with branch points at $\pm k$. The integrand also has poles located at $k_{xp}^{\pm} = \pm \sqrt{k^2 + \alpha_0^2}$ on the proper sheet for $\text{Im } Z_s > 0$. These properties of (A-3) are illustrated in Figure 54.

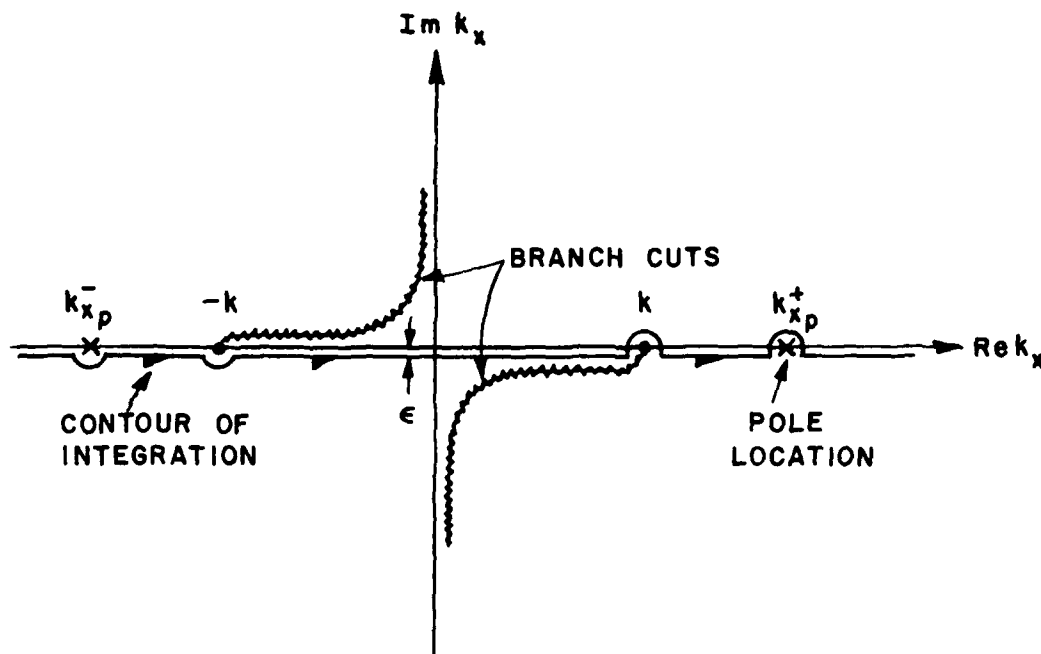


Figure 54--Contour of integration in the complex k_x -plane.

The expression in (A-6) can also be represented as a perturbation of the fields on the perfectly conducting surface as follows:

$$G^h = G_c^h + G_p^h \quad (\text{A-7})$$

where G_c^h is the green's function for the perfectly conducting ground plane; it is given by

$$G_c^h = \frac{1}{2\pi j} \int_{-\infty - j\epsilon}^{\infty - j\epsilon} \frac{e^{-jk_x |x|}}{\sqrt{k^2 - k_x^2}} dk_x = \frac{1}{2j} H_0^{(2)}(k|x|). \quad (\text{A-8})$$

G_p^h is the perturbation Green's function and has the following form

$$G_p^h = -j\alpha_h \frac{1}{2\pi j} \int_{-\infty-j\epsilon}^{\infty-j\epsilon} \frac{e^{-jk_x|x|}}{\sqrt{k^2-k_x^2} [\sqrt{k^2-k_x^2+j\alpha_h}] } dk_x \quad (A-9)$$

In both (A-8) and (A-9), the observation point is brought on to the impedance surface (i.e., $y=0$).

The two alternative expressions for the Green's function given by (A-6) and (A-7) may be approximated asymptotically. The asymptotic evaluation of (A-6) is discussed below in part I-a and that of (A-7) is discussed in part I-b.

a. Saddle Point Approximation

In the asymptotic evaluation of (A-6), it is convenient to begin by introducing the following polar transformations:

$$k_x = k \cos \eta ; \quad dk_x = -k \sin \eta \, d\eta \quad (A-10)$$

and

$$x = \rho \cos \phi ; \quad y = \rho \sin \phi \quad (A-11)$$

The transformation in (A-11) is shown in Figure 55. The Green's function G^h of (A-6) is now expressed in the complex η plane as

$$G^h = -\frac{1}{2\pi j} \int_c F_h(\eta) e^{f(\eta)\Omega} d\eta \quad (A-12)$$

where

$$F_h(\eta) = \frac{\sin \eta}{\sin \eta + j\alpha_h k^{-1}} \quad (A-13)$$

and

$$f(\eta) = -j \cos(\eta - \phi); \quad \Omega = k\rho. \quad (A-14a);$$

$$(A-14b)$$

Ω is the large parameter in this asymptotic development. The contour of integration c is indicated in Figure 56.

η_{p_1} and η_{p_2} are the poles of (A-6) in the complex η plane.

By setting the denominator of (A-13) to zero, one can easily show

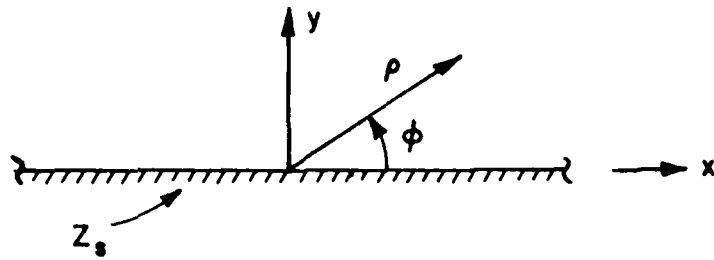


Figure 55--Polar and rectangular coordinate systems.

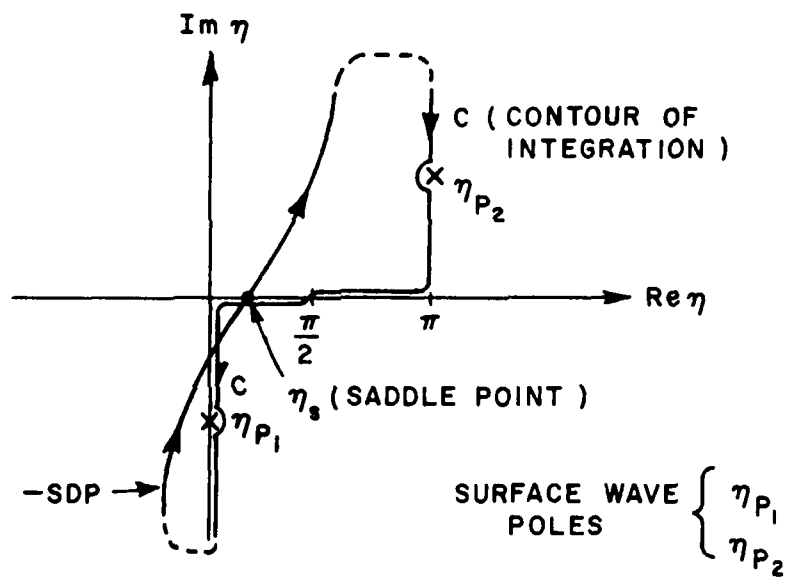


Figure 56--Contour of integration in the complex η -plane.

that $\eta_{p_1} = -j \sinh^{-1}(\alpha_h/k)$ and $\eta_{p_2} = \pi + j \sinh^{-1}(\alpha_h/k)$. The saddle point is denoted by η_s , and it is the solution of $f'(\eta)=0$. It can be shown that $\eta_s = \phi$ for $(0 < \phi < \pi)$. For the special case when the observation point is on the impedance surface (i.e., $\phi=0$), $\eta_s=0$.

Using the results of Felsen and Marcuvitz[26] one can obtain an asymptotic solution for (A-6) as follows

$$G^h \sim R \epsilon^{-1} - \frac{e^{\Omega f(\eta)}}{2\pi j} \left[\pm j 2a \sqrt{\pi} e^{-\Omega b^2} Q(\mp j b \sqrt{\Omega}) + \sqrt{\frac{\pi}{\Omega}} \frac{a}{b} \right]; \quad (A-15)$$

$\text{Im } b \geq 0, \quad \Omega \rightarrow \infty$

where

$$R = \lim_{\eta \rightarrow \eta_{p_1}} \left[(\eta - \eta_{p_1}) F_h(\eta) e^{-f(\eta)\Omega} \right], \quad a = \lim_{\eta \rightarrow \eta_{p_1}} [(\eta - \eta_{p_1}) F_h(\eta)] \quad (A-15a)$$

$$b = \sqrt{f(\eta_s) - f(\eta_{p_1})}, \quad \epsilon = \begin{cases} 1 \\ 0 \end{cases} \quad \text{for } \begin{cases} \text{Im } b > 0 \\ \text{Im } b < 0 \end{cases} \quad (A-15b)$$

$$Q(y) = \int_y^\infty e^{-x^2} dx = \frac{\sqrt{\pi}}{2} \text{erfc}(y) \quad (A-15c)$$

where erfc is the complementary error function. Alternatively, substituting (A-13) and (A-14) into (A-15), with $\eta_s=0$, yields

$$G^h \sim -\frac{j\alpha_h}{\beta_h} e^{-j\beta_h x} \epsilon_h + e^{-jkx} \left[\pm \frac{j\alpha_h}{\beta_h \sqrt{\pi}} Q(\mp j b_h \sqrt{kx}) e^{-kx b_h^2} + \frac{1}{2\pi j} \sqrt{\frac{\pi}{kx}} \frac{j\alpha_h}{\beta_h b_h} \right]; \quad \text{Im } b_h \geq 0 \quad (A-16)$$

where

$$b_h = \sqrt{j} \frac{\alpha_h}{k} \left(\frac{\beta_h}{k} + 1 \right)^{-1/2}; \quad \beta_h = \sqrt{k^2 + \alpha_h^2}. \quad (A-16a)$$

$$\epsilon_h = \begin{cases} 1 \\ 0 \end{cases} \text{ for } (\alpha_h \geq 0) \text{ or } (\text{Im } b_h \geq 0). \quad (\text{A-16b})$$

b. Asymptotic Evaluation of the Perturbation Green's Function Representation

The first term in (A-7) was readily evaluated in (A-8) as the Green's function for the half-space with a magnetic line source located at the coordinate origin. The effect of the impedance is represented by the perturbation Green's function, G_p^h which is given in (A-9). As indicated earlier, the integrand in (A-9) has poles for positive values of α_h . In the process of evaluating (A-9), one defines a new quantity as follows

$$G_p^{h-} = -j\alpha_h^- \frac{1}{2\pi j} \int_{-\infty-j\epsilon}^{\infty-j\epsilon} \frac{e^{-jk_x|x|}}{\sqrt{k^2-k_x^2}[\sqrt{k^2-k_x^2+j\alpha_h^-}]} dk_x \quad (\text{A-17})$$

where $\alpha_h^- = -|\alpha_h|$.

Through a simple manipulation, (A-9) becomes

$$G_p^h = -2j\alpha_h \frac{1}{2\pi j} \epsilon_h \int_{-\infty-j\epsilon}^{\infty-j\epsilon} \frac{e^{-jk_x|x|}}{(k^2+\alpha_h^2)-k_x^2} dk_x + G_p^{h-}. \quad (\text{A-18})$$

The first term in RHS of (A-18) can be calculated by enclosing the contour in the lower half complex k_x -plane and evaluating the residues enclosed. Hence, (A-18) becomes,

$$G_p^h = -\frac{j\alpha_h}{\beta_h} e^{-j\beta_h|x|} \epsilon_h + G_p^{h-}. \quad (\text{A-19})$$

The integrand in G_p^{h-} has no poles on the proper sheet, therefore it can be rewritten as follows:

$$G_p^{h-} = \frac{\alpha_h^-}{2j} \int_0^\infty H_0^{(2)}(k\sqrt{\tau^2+x^2}) e^{\alpha_h^- \tau} d\tau \quad (\text{A-20})$$

where the relations

$$\frac{1}{\sqrt{k^2-k_x^2+j\alpha_h^-}} = j \int_0^\infty e^{-j[\sqrt{k^2-k_x^2} + j\alpha_h^-]\tau} d\tau$$

and

$$H_0^{(2)}(k\sqrt{\tau^2+x^2}) = \frac{1}{\pi} \int_{-\infty}^{\infty} dk_x \frac{e^{-jk_x|x| - j\tau\sqrt{k^2-k_x^2}}}{\sqrt{k^2-k_x^2}}$$

are employed [26] in the integrand of (A-17) to arrive at (A-20).

For large values of α_h^- and x , (A-20) can be evaluated by the large argument approximation for the Hankel function as

$$G_p^{h-} \sim \frac{\alpha_h^-}{2j} \int_0^{\infty} \frac{2}{\sqrt{\pi k|x|}} e^{-j(kx[1 + \frac{1}{2}(\frac{\tau}{x})^2] - \frac{\pi}{4}) + \alpha_h^- \tau} d\tau. \quad (A-21)$$

Next, introducing a new variable $z = \sqrt{jk}(\frac{\tau}{\sqrt{2t}} + j\frac{\alpha_h^-}{k}\sqrt{\frac{t}{2}})$, one can show that

$$G_p^{h-} \sim -\frac{j\alpha_h^-}{k\sqrt{\pi}} e^{-jk|x|(1 + \frac{\alpha_h^2}{2k^2})} Q\left(j\left[\frac{\sqrt{j}\alpha_h^-}{\sqrt{2}k}\right]\sqrt{k|x|}\right); \quad |x| \rightarrow \infty \quad (A-22)$$

For small values of α_h^- , the integral in (A-20) is slowly convergent; however, one could overcome this difficulty by expanding G_p^{h-} in a power series of α_h^- as follows.

$$G_p^{h-} = -j\alpha_h^- \frac{1}{2\pi j} \int_{-\infty-j\epsilon}^{\infty-j\epsilon} dk_x e^{-jk_x|x|} \left[\frac{1}{(k^2 + \alpha_h^2) - k_x^2} - \frac{j\alpha_h^-}{\sqrt{k^2 - k_x^2}[(k^2 - k_x^2) + \alpha_h^2]} \right] \quad (A-23)$$

Evaluating the first term in (A-23) by the calculus of residues, and expanding the second term in powers of α_h^- yields

AD-A084 345

OHIO STATE UNIV COLUMBUS ELECTROSCIENCE LAB F/6 20/14
RADIATION BY SOURCES ON PERFECTLY CONDUCTING CONVEX CYLINDERS W--ETC(U)
JAN 80 L ERSOY, P H PATHAK F19628-77-C-0107
ESL-784641-2

UNCLASSIFIED

RADC -TR-79-281

NL

2 of 2
AD
70014.1-06

END
DATE
FILMED
6-80
DTIC

$$G_p^{h-} = -j \frac{\alpha_h^-}{2\beta_h} e^{-j\beta_h|x|} - \frac{\alpha_h^2}{2\pi j} \int_{-\infty-j\epsilon}^{\infty-j\epsilon} dk_x e^{-jk_x|x|} \left[\frac{1}{(k^2-k_x^2)^{3/2}} - \frac{\alpha_h^2}{(k^2-k_x^2)^{5/2}} + \frac{\alpha_h^4}{(k^2-k_x^2)^{7/2}} + \dots \right] \quad (A-24)$$

or

$$G_p^{h-} = -j \frac{\alpha_h^-}{2\beta_h} e^{-j\beta_h|x|} - \frac{\alpha_h^2}{2jk^2} \sum_{p=1}^{\infty} \frac{(k|x|)^p}{1 \cdot 3 \dots (2p-1)} \left(\frac{j\alpha_h^-}{k} \right)^{2(p-1)} H_p^{(2)}(k|x|) \quad (A-25)$$

In obtaining (A-25) from (A-24), the relation

$$\frac{1}{2\pi j} \int_{-\infty-j\epsilon}^{\infty-j\epsilon} \frac{e^{-jk_x|x|}}{(k^2-k_x^2)^p \sqrt{k^2-k_x^2}} dk_x = \frac{1}{2j} \frac{(k|x|)^p}{1 \cdot 3 \dots (2p-1)} H_p^{(2)}(k|x|); p=1,2,3,\dots \quad (A-26)$$

is used.

A closed form expression for (A-25) may be obtained for large values of x . To this end, one uses the asymptotic approximation for the Hankel function and rearranges the resulting series in (A-25) which yields

$$G_p^{h-} = -\frac{j\alpha_h^-}{2\beta_h} e^{-j\beta_h|x|} + \frac{j\alpha_h^-}{2k} e^{-jk|x|} \left(1 + \frac{\alpha_h^2}{2k^2} \right) \frac{2}{\sqrt{\pi}} e^{j\frac{\alpha_h^2}{2k^2} k|x|} \cdot \sum_{n=0}^{\infty} \frac{2^n}{1 \cdot 3 \dots (2n+1)} \left(j \left[\frac{j\alpha_h^-}{k\sqrt{2}} \right] \sqrt{k|x|} \right)^{2n+1} \quad (A-27a)$$

or

$$G_p^{h-} = -\frac{j\alpha_h^-}{2\beta_h} e^{-j\beta_h|x|} + \frac{j\alpha_h^-}{2k} e^{-jk|x|} \left(1 + \frac{\alpha_h^2}{2k^2} \right) \operatorname{erf} \left(j \left[\frac{j\alpha_h^-}{k\sqrt{2}} \right] \sqrt{k|x|} \right) \quad (A-27b)$$

Since (A-27b) is derived for small values of α_h , one can approximate $\beta_h \sim k$ for the amplitude terms (i.e., when β_h is in the denominator), and by $\beta_h \sim k(1 + \alpha_h^2/2k^2)$ for the phase terms (i.e., when it is in the exponent). This approximation yields

$$G_p^h \sim - \frac{j\alpha_h^-}{k\sqrt{\pi}} e^{-jk|x| \left(1 + \frac{\alpha_h^2}{2k^2}\right)} Q\left(j \left[\frac{\sqrt{j}\alpha_h^-}{k\sqrt{2}}\right] \sqrt{k|x|}\right) \quad (A-28)$$

The above analysis shows that regardless of the value of α_h , G_p^h has the same form as given by (A-22) or (A-28), for large values of $|x|$.

Substituting (A-27) or (A-28) into (A-19) and substituting this result and (A-8) into (A-7) yields

$$G^h \sim - \frac{j\alpha_h}{\beta_h} e^{-j\beta_h|x|} \epsilon_h + \left[- \frac{j\alpha_h^-}{k\sqrt{\pi}} e^{-jk|x|} Q\left(j \beta_h \sqrt{k|x|}\right) e^{-k|x|\tilde{\beta}_h^2} + \frac{1}{2j} H_0^{(2)}(k|x|) \right] \quad (A-29)$$

where

$$\tilde{\beta}_h = \frac{\alpha_h^-}{k} \sqrt{\frac{j}{2}} \quad (A-29a)$$

As indicated earlier, (A-29) is valid for both small and large values of α_h , when $|x|$ is large. It can easily be shown that (A-29) goes to the saddle point approximation of (A-16) for small values of α_h and large values of $|x|$. On the other hand, for small values of $|x|$, the Hankel function in (A-29) will dominate and provide an adequate description of the current near the source. Thus Equation (A-29) is an asymptotic approximation of the Green's function which also remains valid in the vicinity of the source for all values of α_h ; whereas, (A-16) is an asymptotic approximation of the Green's function for large values of x .

II. TM_z or Magnetic Line Dipole Source Excitation Case

The magnetic source density for this polarization is denoted by \overline{M}_d , and it is given by

$$\overline{M}_d = \hat{x} M_d \delta(x)\delta(y) \quad (A-30)$$

where M_d is the strength of the source which is assumed known. The tangential magnetic field generated by such a source has only \hat{x} -component and it will be denoted by H_x . H_x can be obtained from the only electric field E_z^I generated by an electric line source $\vec{I} = \hat{z} I \delta(x-x') \delta(y-y')$. Here, I is the known strength of the electric line source. E_z^I satisfies (A-2) and (A-3) with the exception that $Y_0 M$ is replaced by $Z_0 I$ and α_h is replaced by α_s respectively, where

$$\alpha_s = -jk \frac{Y_s}{Y_0} \quad (A-31)$$

E_z^I also satisfies the radiation condition for an $e^{j\omega t}$ time dependence. With above changes, (A-5) becomes

$$E_z^I(x', y') = -jk Z_0 I G^S(x', y' | x, y) \quad (A-32)$$

G^S corresponds to G^h of the TE_z -case, and using the procedure of [25], one can show that

$$G^S(x', y' | x, y) = \frac{1}{2\pi j} \int_{-\infty - j\epsilon}^{\infty - j\epsilon} \frac{e^{-j\sqrt{k^2 - k_x^2}(y' - y)} + R_s e^{-j\sqrt{k^2 - k_x^2}(y' + y)}}{2\sqrt{k^2 - k_x^2}} e^{-jk_x |x' - x|} dk_x; y' > y \quad (A-33)$$

where $R_s = (\sqrt{k^2 - k_x^2} - j\alpha_s)(\sqrt{k^2 - k_x^2} + j\alpha_s)^{-1}$.

The case for $y > y'$ can be obtained from (A-33) by interchanging y and y' . It is no surprise that (A-6) is the special case of (A-33) when $y=0$ and α_s is replaced by α_h . The magnetic field, M_x^I generated by \vec{I} can be found from $\nabla \times \vec{E} = -j\omega \mu_0 \vec{H}^I$. The electric field, E_z^I generated by \vec{M}_d of (A-30) can now be found from the reciprocity theorem which yields $\vec{I} \cdot \vec{E} = -M_d \hat{x} \cdot \vec{H}^I$. Making use of the other Maxwell's curl equation, $\vec{H} = -(j\omega \mu_0)^{-1} [\nabla \times \vec{E} + \vec{M}_d]$ it can be shown that

$$H_x(x, y) = -jk Y_0 M_d G^S(x, y | 0, 0) \quad (A-34)$$

where

$$G^S(x, y | 0, 0) = \frac{j\alpha_s}{k^2} \frac{1}{2\pi j} \int_{-\infty - j\epsilon}^{\infty - j\epsilon} \frac{\sqrt{k^2 - k_x^2}}{\sqrt{k^2 - k_x^2} + j\alpha_s} e^{-j\sqrt{k^2 - k_x^2} y - jk_x |x|} dk_x \quad (A-35)$$

The contour of integration in (A-35) and the branch cuts in the integrand (A-35) are the same as in Figure 54. The integrand in (A-35) has poles located at $k_{xp}^2 = \sqrt{k^2 - \alpha_s^2}$ on the proper sheet for the positive values of α_s .

The expression in (A-35) can also be represented as a perturbation of the fields on the perfectly conducting plane surface as follows:

$$G^S = G_C^S + G_P^S \quad (A-36)$$

where G_C^S is the TM_y type Green's function for the perfectly conducting ground plane; it is given by

$$G_C^S = \frac{1}{2\pi j} \frac{1}{k^2} \int_{-\infty-j\epsilon}^{\infty-j\epsilon} \sqrt{k^2 - k_x^2} e^{jk_x |x|} dk_x = \frac{1}{2j} \frac{H_1^{(2)}(k|x|)}{k|x|} \quad (A-37)$$

G_P^S is the perturbation Green's function, and it has the following form:

$$G_P^S = \frac{1}{2\pi j} \int_{-\infty-j\epsilon}^{\infty-j\epsilon} \frac{k^2 - k_x^2}{k^2 (\sqrt{k^2 - k_x^2 + j\alpha_s})} e^{-jk_x |x|} dk_x \quad (A-38)$$

In both (A-37) and (A-38), the observation point is brought on to the impedance surface (i.e., $y=0$). The integral in (A-35) will next be asymptotically approximated via the saddle point method in part II-(a); likewise, the perturbation integral corresponding to G_P^S in (A-38) will be asymptotically approximated in part II-(b).

a. Saddle Point Approximation

Equation (A-35) will be asymptotically evaluated in a manner similar to that in part I-a of this appendix.

Substituting the transformations (A-10) and (A-11) into (A-35) yields

$$G^S = -\frac{1}{2\pi j} \int_C F_S(\eta) e^{f(\eta)\Omega} d\Omega \quad (A-39)$$

where

$$F_S(\Omega) = \frac{j\alpha_s}{k} \frac{\sin^2 \eta}{\sin \eta + j \frac{\alpha_s}{k}} \quad (A-40)$$

and $f(\eta)$ is the same as in (A-14).

Figures 55 and 56 are also the same for TM_z case with the exception that the poles of (A-40) are now located at $\eta_p = -j \sinh^{-1}(\alpha_s/k)$ and $\eta_{p2} = \pi + j \sinh^{-1}(\alpha_s/k)$. Changing the subscript¹ or superscript "h" to "s" in (A-15) through (A-15c), one arrives at an asymptotic representation of G^s . The final result has the following form

$$G^s \sim -\frac{j\alpha_s^3}{k^2\beta_s} e^{-j\beta_s|x|} \epsilon_s + e^{-jk|x|} \left[\frac{j\alpha_s^3}{k^2\beta_s\sqrt{\pi}} Q(\mp j\beta_s\sqrt{k|x|}) e^{-jkxb_s^2} + \frac{1}{2\pi j} \sqrt{\frac{\pi}{k|x|}} \frac{j\alpha_s^3}{k^2\beta_s b_s} \right]; \quad \text{Im } b_s \geq 0 \quad (\text{A-41})$$

where

$$b_s = \frac{j\alpha_s}{k} \left(\frac{\beta_s}{k} + 1 \right)^{-1/2}, \quad \beta_s = \sqrt{k^2 + \alpha_s^2} \quad (\text{A-42a})$$

$$\epsilon_s = \begin{cases} 1 \\ 0 \end{cases} \text{ for } (\alpha_s \geq 0) \text{ or } (\text{Im } b_s \geq 0) \quad (\text{A-42b})$$

b. Asymptotic Evaluation of the Perturbation Green's Function Representation

The alternative representation in (A-36) will now be evaluated. It is already shown in (A-37) that G^s is the Green's function for the perfectly conducting plane surface with an \hat{x} -directed magnetic line dipole source located at the coordinate region. The impedance effect is then represented by G_p^s which is given in (A-38). In the process of evaluating (A-38), one first separates the pole contribution as follows.

$$G_p^s = -\frac{1}{2\pi j} \int_{-\infty-j\epsilon}^{\infty-j\epsilon} \frac{k^2 - k_x^2}{k^2(\sqrt{k^2 - k_x^2 + j\alpha_x^-})} e^{-jk_x|x|} dk_x - \frac{\epsilon_s}{2\pi j} \int_{-\infty-j\epsilon}^{\infty-j\epsilon} \frac{1}{k^2} \left[\frac{2j\alpha_s^3}{k^2 + \alpha_s^2 - k_x^2} - 2j\alpha_s \right] e^{-jk_x|x|} dk_x \quad (\text{A-43})$$

where $\alpha_x^- = -|\alpha_x|$. The last integral in (A-43) can be integrated via the calculus of residues.

Next, incorporating the following relationships

$$\left(1 + \frac{d^2}{d(k|x|)}\right) e^{-jk_x|x|} = \frac{k^2 - k_x^2}{k^2} e^{-jk_x|x|} \quad (A-44a)$$

and

$$\frac{1}{\sqrt{k^2 - k_x^2 + j\alpha_s}} = \frac{1}{\sqrt{k^2 - k_x^2}} - \frac{j\alpha_s}{k\sqrt{k^2 - k_x^2}[\sqrt{k^2 - k_x^2} + j\alpha_s]} \quad (A-44b)$$

into the first integral of (A-43) yields

$$G_p^s = -\left(1 + \frac{d^2}{d[k|x|]^2}\right) \left[\frac{1}{2j} H_0^{(2)}(k|x|) + \left\{ -j\alpha_s^- \frac{1}{2\pi j} \int_{-\infty - j\epsilon}^{\infty - j\epsilon} \frac{e^{-jk_x|x|}}{\sqrt{k^2 - k_x^2}[\sqrt{k^2 - k_x^2} + j\alpha_s^-]} dk_x \right\} - \frac{j\alpha_s^3}{\beta_s k^2} e^{-j\beta_s|x|} \epsilon_s + \frac{2\alpha_s}{k} \delta(k|x|) \epsilon_s \right] \quad (A-45)$$

Comparison of (A-17) with the term in the curly bracket of (A-45) shows that they are the same with the exception that in the latter α_s^- is replaced by α_s^- . Hence the evaluation of (A-17) leading to the result in (A-22) is equally valid for the integral in (A-45) as long as all of the superscripts and subscripts in part I-b are replaced by "s" in the present development. With the above comments in mind, one can now readily write an asymptotic expression for G_p^s by substituting (A-22) or (A-28) into (A-45).

$$G_p^s \sim -\left(1 + \frac{d^2}{d[k|x|]^2}\right) \left[\frac{1}{2j} H_0^{(2)}(k|x|) - \frac{j\alpha_s^-}{k\sqrt{\pi}} e^{-jk|x|} Q(j\tilde{b}_s\sqrt{k|x|}) e^{-k|x|\tilde{b}_s^2} - \frac{j\alpha_s^3}{\beta_s k^2} e^{-j\beta_s|x|} \epsilon_s + \frac{2\alpha_s}{k} \delta(k|x|) \epsilon_s \right] \quad (A-46)$$

where

$$\tilde{b}_s = \frac{\alpha_s^-}{k} \sqrt{\frac{j}{2}} \quad (A-46a)$$

The term involving the Q function in (A-46) can be written as follows

$$\begin{aligned} \frac{j\alpha_s^-}{k\sqrt{\pi}} e^{-jk|x|} Q(j\tilde{b}_s \sqrt{k|x|}) e^{-k|x|\tilde{b}_s^2} &= \\ &= \frac{1}{2j} \left[\sqrt{\frac{2j}{\pi t}} e^{-jt} \right] 2z e^{z^2} Q(z) \end{aligned} \quad (A-47)$$

where $z = j\tilde{b}_s \sqrt{k|x|}$. The term inside the brackets is recognized as the large s argument approximation of the Hankel function. Hence one can conjecture a different asymptotic form for (A-46) as follows

$$\begin{aligned} G_p^s \sim & - \left(1 + \frac{d^2}{d|k|x|^2} \right) \left[\frac{1}{2j} H_0^{(2)}(k|x|) - \frac{1}{2j} H_0^{(2)}(k|x|) 2z e^{z^2} Q(z) \right] - \\ & - \frac{j\alpha_s^3}{\beta_s k^2} e^{-j\beta_s|x|} \epsilon_s + \frac{2\alpha_s}{k} \delta(k|x|) \epsilon_s. \end{aligned} \quad (A-48)$$

This conjecture can be justified if one notes that as the admittance tends to infinity corresponding to the case of a perfectly conducting ground plane then $2z e^{z^2} Q(z)$, tends to unity (i.e., $\lim_{\alpha_s \rightarrow \infty} 2z e^{z^2} Q(z) = 1$) for $x \neq 0$. Hence, the first two terms in (A-48) cancel each other as $\alpha_s \rightarrow \infty$. The addition of a small loss in the medium for ($y > 0$, $|x| < \infty$) nullifies the surface wave as $\alpha_s \rightarrow \infty$, thereby resulting in a zero contribution from G_p^s term to G^s . Hence, in the limit as the impedance surface goes to the perfectly conducting ground plane, G^s becomes:

$$\lim_{\substack{\alpha_s \rightarrow \infty \\ |x| \neq 0}} G^s = G_c^s = \frac{1}{2j} \frac{H_1^{(2)}(k|x|)}{k|x|}. \quad (A-49)$$

which is the desired result for TM_z case.

Finally substituting (A-37) and (A-48) into (A-36) yields:

$$G^S \sim -\frac{j\alpha_s^3}{k^2\beta_s} e^{-j\beta_s|x|} \epsilon_s + \frac{2\alpha_s}{k} \delta(k|x|)\epsilon_s + \frac{1}{2j} \frac{H_1^{(2)}(k|x|)}{|k|x|} \\ - \left(1 + \frac{d^2}{d[k|x|]^2}\right) \left[\frac{1}{2j} H_0^{(2)}(k|x|) \cdot \left\{ 1 - 2z e^{z^2} Q(z) \right\} \right] \quad (A-50)$$

where as before $z = j\tilde{b}\sqrt{k|x|}$ and b_s is defined in (A-46a). The first term in (A-50) corresponds to the surface wave field.

APPENDIX B

AN ANALYSIS OF THE RADIATION FROM LINE SOURCES ON A CIRCULAR CYLINDER COMPLETELY COVERED WITH AN IMPEDANCE SURFACE

In this appendix, the radiation from line sources on a circular cylinder covered with an impedance surface is analyzed. The geometrical configuration of the problem is illustrated in Figure 4.

Two different source orientations are discussed. The first of these is for the case of a \hat{z} -directed magnetic line source excitation which is illustrated in Figure 4; this case will be referred to as the TE_z case and it is treated first in Section I below. The second source orientation refers to a $\hat{\phi}$ -directed magnetic line dipole source excitation case as shown in Figure 4. Henceforth, the second case will be designated as the TM_z case and it will be dealt with subsequently in Section II.

I. TE_z or Magnetic Line Source Excitation Case

The magnetic source density for this polarization is denoted by \bar{M} and is given by

$$\bar{M} = \hat{z} M \frac{\delta(\rho-a)\delta(\phi)}{\rho} \quad (B-1)$$

where M is the known strength of the source and a is the radius of the cylinder. The magnetic field generated by such a source has only a \hat{z} -component and it will be denoted by H_z . H_z satisfies the reduced, inhomogeneous wave equation, and the following boundary conditions:

$$(\nabla_t^2 + k^2)H_z = jkY_0 M \frac{\delta(\rho-a)\delta(\phi)}{\rho}; \quad \begin{matrix} \rho > a \\ 0 \leq \phi \leq 2\pi \end{matrix} \quad (B-2)$$

and

$$\frac{\partial H_z}{\partial \rho} + \alpha_h H_z = 0 \text{ at } \rho = a \quad (B-3)$$

where α_h is given in (A-4). Also H_z satisfies the radiation condition for an $e^{j\omega t}$ time dependence. For solving (B-2) one defines a two-

dimensional Green's function, $\tilde{G}^h(\rho, \phi | \rho', \phi')$ such that

$$H_z(\rho, \phi) = -jkY_0 M \tilde{G}^h(\rho, \phi | a, 0) \quad (B-4)$$

$\tilde{G}^h(\rho, \phi | \rho', \phi')$ is the solution of (B-2) with $-\delta(\rho - \rho')\delta(\phi - \phi')/\rho$ the source term on the RHS. It also satisfies (B-3) and the radiation condition. It can be shown that the Green's function has the following form [26]:

$$\begin{aligned} \tilde{G}^h(\rho, \phi | \rho', \phi') = & -\frac{1}{8} \int_{-\infty - j\epsilon}^{\infty - j\epsilon} dv \left[H_v^{(1)}(k\rho') - \frac{Q_h H_v^{(1)}(ka)}{Q_h H_v^{(2)}(ka)} H_v^{(2)}(k\rho') \right] \\ & \cdot H_v^{(2)}(k\rho) \frac{\cos v(\pi - |\phi - \phi'|)}{\sin v\pi} \end{aligned} \quad (B-5)$$

where $Q_h = \frac{\partial}{\partial [k\rho]} + \frac{\alpha_h}{k}$.

One may write

$$\frac{\cos v(\pi - |\phi - \phi'|)}{\sin v\pi} = j \sum_{l=0}^{\infty} [e^{-jv|\phi - \phi'|} + e^{-jv\phi^-}] e^{-jv(2\pi l)} \quad (B-6)$$

where $\phi^- = 2\pi - |\phi - \phi'|$. Physically, the above series corresponds to multiple encirclements of the field around the cylinder in the azimuthal propagation representation for Green's function of (B-5). Since one is interested in applying the results of the present analysis to perfectly conducting cylinders with an impedance surface patch, the effect of these multiple encirclements will be neglected with the exception of the ray which will travel the shortest distance between the source and the observation points, i.e., $(\cos v(\pi - |\phi - \phi'|))/\sin v\pi$ will be replaced by $je^{-jv|\phi - \phi'|}$ in (B-5), yielding

$$\begin{aligned} G^h(\rho, \phi | \rho', \phi') \sim & -\frac{j}{8} \int_{-\infty - j\epsilon}^{\infty - j\epsilon} dv \left[H_v^{(1)}(k\rho') - \frac{Q_h H_v^{(1)}(ka)}{Q_h H_v^{(2)}(ka)} H_v^{(2)}(k\rho') \right] \\ & H_v^{(2)}(k\rho) \cdot e^{-jv|\phi - \phi'|} \end{aligned} \quad (B-7)$$

From here on, G^h in (B-7) will be referred to as the Green's function and it will be used in place of \tilde{G}^h (for example Equation (B-4) now will read $H_z(\rho, \phi) = -jkY_0 M G^h(\rho, \phi | a, 0)$). One notes that

the contributions from higher order encirclements to \tilde{G} in (B-5) can be found simply by replacing $|\phi - \phi'|$ in G^h of (B-7) with $|\phi - \phi'| + 2\pi$ or with $(2\pi - |\phi - \phi'|) + 2\pi\ell$ and summing them up over ℓ as indicated by (B-6).

The expression in (B-7) can be represented as a perturbation of the fields on the perfectly conducting cylindrical surface as follows:

$$G^h = G_C^h + G_p^h \quad (B-8)$$

where G_C^h is the Green's function for the magnetic line source in (B-1) when it is placed on a perfectly conducting cylinder; it is obtained from (B-7) upon setting $\alpha_h = 0$. Thus,

$$G_C^h = -\frac{1}{2\pi} \int_{-\infty-j\epsilon}^{\infty-j\epsilon} d\left(\frac{\nu}{ka}\right) \frac{H_\nu^{(2)}(ka)}{H_\nu^{(2)'}(ka)} e^{-j\nu|\phi|}. \quad (B-9)$$

Following an analysis which is based on some earlier work by Hasserjian and Ishimaru[19], one obtains the following approximation for (B-9):

$$G_C^h \sim \frac{1}{2j} H_0^{(2)}(ka|\phi|) \left[1 - \frac{\sqrt{\pi}j}{4} \xi^{3/2} + j \frac{7}{60} \xi^3 + \frac{7\sqrt{-\pi}j}{512} \xi^{9/2} + \dots \right] \quad (B-10)$$

$$\text{where } \xi = \left(\frac{ka}{2}\right)^{1/3} |\phi|.$$

G_p^h is the perturbation Green's function and it is given as follows:

$$G_p^h = \frac{j\alpha_h}{k} \frac{1}{2\pi j} \int_{-\infty-j\epsilon}^{\infty-j\epsilon} d\left(\frac{\nu}{ka}\right) P_\nu(ka; \alpha_h) P_\nu(ka; 0) e^{j\nu|\phi|} \quad (B-11)$$

where

$$P_\nu(ka; \alpha_h) = \frac{H_\nu^{(2)}(ka)}{H_\nu^{(2)'}(ka) + \frac{\alpha_h}{k} H_\nu^{(2)}(ka)} \quad (B-12)$$

The prime over the Hankel function in (B-12) indicates differentiation with respect to the argument. In both (B-9) and (B-11), the observation point is brought on to the surface of the cylinder (i.e., $\rho=a$).

In the process of evaluating G^h in (B-11), one encounters the problem of expanding the Hankel function in an asymptotic series for the different ranges of the parameters involved. In the immediate neighborhood of the source; that is, when $ka|\phi|$ is small, the main contribution to the integral in (B-11) comes from the values of v which satisfies the inequality $|v-ka|>0(m)$ where $2m^3(=ka)$ is taken as the large parameter. The Debye asymptotic expansion is the most suitable representation for the Hankel function for small values of $ka|\phi|$. If $ka|\phi|$ is moderately small then one employs the Watson approximation for the Hankel function. The Watson approximation corresponds to the values of v such that $|v-ka|<0(m)$.

A third representation referred to as the creeping wave representation for the fields can be found by evaluating (B-8) via the calculus of residues. This creeping wave solution is rapidly convergent for large values of $ka|\phi|$. One points out that the Debye approximation presented below goes to the Watson approximation for $v \sim 0(ka)$, and that the results obtained from the Watson approximation for the Green's function blend with the creeping wave representation for moderately large values of $ka|\phi|$.

Equation (B-11) will be evaluated firstly by the method of Debye approximation in part Ia of this appendix. The Watson approximation and the creeping wave representations of (B-11) will be carried out subsequently in parts (Ib) and (Ic) respectively.

a. Debye Approximation

This asymptotic expansion is valid for large values of the argument, ka , and the order, v , of the Hankel function such that $|v-ka|>0(m)$. Then, it can be shown that [27,28]

$$H_v^{(2)}(ka) \sim j \frac{e^{-jv(\tan\eta-\eta) - j\frac{\pi}{4}}}{\sqrt{\frac{\pi}{2}} v \tan \eta} \left[1 - \frac{u_1}{v} + o\left(\frac{1}{v^2}\right) \right] \quad (B-13a)$$

and

$$H_v^{(2)'}(ka) \sim -j \frac{\sin 2\eta}{\pi \eta} e^{-jv(\tan\eta-\eta) + j\frac{\pi}{4}} \left[1 - \frac{v_1}{v} + o\left(\frac{1}{v^2}\right) \right] \quad (B-13b)$$

where η is a fixed positive number and $\cos \eta = v/ka$. Also, u_1 and v_1 are given as

$$u_1 = -\frac{j}{24} (3 \cot \eta + 5 \cot^3 \eta) ; \quad v_1 = \frac{j}{24} (9 \cot \eta + 7 \cot^3 \eta) \quad (B-14)$$

After substituting (B-13) into (B-12) and rearranging the terms, one arrives as

$$P_v(ka; \alpha_h) \sim \frac{j}{\sin \eta + j \frac{\alpha_h}{k}} \frac{1 - \frac{u_1}{v} + O\left(\frac{1}{v^2}\right)}{1 - \frac{v_1 \sin \eta + j \alpha_h k^{-1} u_1}{\sin \eta + j \alpha_h k^{-1}} \frac{1}{v} + O\left(\frac{1}{v^2}\right)} \quad (B-15a)$$

Carrying out the division in (B-15) and retaining only the terms up to and including terms of order $1/v$ with respect to unity and using (B-14) yields,

$$P_v(ka; \alpha_h) \sim \frac{j}{\sin \eta + j \alpha_h k^{-1}} \left[1 + \frac{j}{2 \sin^2 \eta} \frac{1}{\sin \eta + j \alpha_h k^{-1}} \frac{\cos \eta}{v} + O\left(\frac{1}{v^2}\right) \right] \quad (B-15b)$$

Substituting (B-15b) into (B-11) and performing the indicated multiplication between $P_v(ka; \alpha_h)$ and $P_v(ka; 0)$ leads to:

$$G_p^h \sim G_{p_0}^h + G_{p_1}^h \left(\frac{1}{ka} \right) + O\left(\frac{1}{[ka]^2} \right), \quad (B-16)$$

where

$$G_{p_0}^h = -j \alpha_h \frac{1}{2\pi j} \int_{-\infty - j\epsilon}^{\infty - j\epsilon} d\xi \frac{e^{-j\xi a|\phi|}}{\sqrt{k^2 - \xi^2} [\sqrt{k^2 - \xi^2} + j \alpha_h]}, \quad (B-17)$$

and

$$G_{p_1}^h = \frac{k\alpha_h}{2} \frac{1}{2\pi j} \int_{-\infty-j\epsilon}^{\infty-j\epsilon} d\xi \frac{2\sqrt{k^2-\xi^2} + j\alpha_h}{(k^2-\xi^2)^2 [\sqrt{k^2-\xi^2} + j\alpha_h]^2} e^{-j\xi a|\phi|}. \quad (B-18)$$

A change of variable, (i.e., $\xi = v/a$) has been introduced in the above equations, and it is recognized that $\cos \eta = v/ka$ and $\sin \eta = \sqrt{k^2 - \xi^2}/k$. Comparison of (B-17) and (A-9) reveals that these two equations are indeed identical with the exception that the distance, $|x|$ between the source and the observation point on the flat surface in (A-9) is now being replaced by the arc length $a|\phi|$ on the surface of the cylinder. Hence, the same argument presented in Appendix I can also be used here for (B-17); this results in

$$G_{p_0}^h = -\frac{j\alpha_h}{\beta_h} e^{-j\beta_h a|\phi|} \epsilon_h - \frac{j\alpha_h^-}{k\sqrt{\pi}} e^{-jka|\phi|} Q(j\tilde{b}_h \sqrt{ka|\phi|}) e^{-ka|\phi|} \tilde{b}_h^2 \quad (B-19)$$

where, as before

$$\beta_h = \sqrt{k^2 + \alpha_h^2}; \quad \tilde{b}_h = \frac{\alpha_h^-}{k} \sqrt{\frac{j}{2}}; \quad \alpha_h^- = -|\alpha_h| \quad (B-19a)$$

and

$$\epsilon_h = \begin{cases} 1 \\ 0 \end{cases} \text{ for } \alpha_h \gtrless 0 \quad (B-19b)$$

In order to evaluate $G_{p_1}^h$, one rewrites (B-18) as follows:

$$G_{p_1}^h = -\frac{k^3}{4\pi} \int_{-\infty-j\epsilon}^{\infty-j\epsilon} d\xi e^{-j\xi a|\phi|} \left[\frac{1}{(k^2-\xi^2)^2} + \frac{1}{\alpha_h^2} \frac{1}{(k^2-\xi^2)} - \frac{1}{\alpha_h^2} \left(1 - \alpha_h \frac{d}{d\alpha_h} \right) \cdot \frac{1}{\sqrt{k^2-\xi^2} [\sqrt{k^2-\xi^2} + j\alpha_h]} \right] \quad (B-20)$$

The first two terms in (B-20) can be evaluated using calculus of residues. The last term in (B-20) can be written in terms of $G_{p_0}^h$ of (B-17), leading to

$$G_{p_1}^h = -\frac{jk^2}{4\alpha_h^2} \left[e^{-jka|\phi|} \left(\frac{1+jka|\phi|}{2} \frac{\alpha_h^2}{k^2} + 1 \right) + 2 \left(1 - \alpha_h \frac{d}{d\alpha_h} \right) \left\{ \frac{kG_{p_0}^h}{j\alpha_h} \right\} \right] \quad (B-21)$$

The explicit form of the derivative term in (B-2) can be found by simply differentiating (B-19) with respect to α_h , resulting in

$$\alpha_h \frac{d}{d\alpha_h} \left\{ \frac{kG_{p_0}^h}{j\alpha_h} \right\} = \left(j\beta_h t + 1 \right) \frac{k\alpha_h^2}{\beta_h^3} e^{-j\beta_h a|\phi|} \epsilon_h + \frac{j\alpha_h}{k} \sqrt{\frac{jka|\phi|}{2\pi}} e^{-jka|\phi|} \\ \mp \frac{j\alpha_h^2 a|\phi|}{k\sqrt{\pi}} e^{-jka|\phi|} Q(j\beta_h \sqrt{ka|\phi|}) e^{-k\beta_h^2 a|\phi|}; \alpha_h \geq 0 \quad (B-22)$$

In the process of deriving (B-22) one uses the fact that $\frac{d}{d\alpha_h} Q(j\beta_h \sqrt{ka|\phi|}) = \pm \frac{j}{k} \sqrt{\frac{jka|\phi|}{2\pi}} e^{-k\beta_h^2 a|\phi|}$, which is the consequence of the definition of the Q function (see (A-15c)), and $\frac{d}{dz} \text{erfc}(z) = -\frac{2}{\sqrt{\pi}} e^{-z^2}$. It may also be pointed out that $\alpha_h^-/\alpha_h = \mp 1$; $\alpha_h \geq 0$.

b. Watson Approximation

The Watson approximation is valid for the large values of the argument, ka and the order, ν of the Hankel functions such that $|\nu - ka| < O(m)$. For such values of ν , it can be shown that [28]

$$H_\nu^{(2)}(ka) \sim \frac{j}{m\sqrt{\pi}} w_2(\sigma) \quad (B-23a)$$

and

$$H_\nu^{(2)'}(ka) \sim -\frac{j}{m^2\sqrt{\pi}} w_2'(\sigma) \quad (B-23b)$$

where

$$\sigma = \frac{\nu - ka}{m}, \quad m = \left(\frac{ka}{2}\right)^{1/3} \quad (\text{B-23c})$$

$$w_2(\sigma) = \sqrt{\pi} [Bi(\sigma) - j Ai(\sigma)], \quad w_2'(\sigma) = \sqrt{\pi} [Bi'(\sigma) - j Ai'(\sigma)] \quad (\text{B-23d})$$

$Ai(\sigma)$ and $Bi(\sigma)$ are the Miller type Airy functions. Substituting (B-23a,b) into (B-12) yields

$$P_v(ka; \alpha_h) \sim - \frac{1}{\frac{1}{m} \psi_2(\sigma) - \frac{\alpha_h}{k}} \quad (\text{B-24})$$

where $\psi_2(\sigma)$ is the ratio of $w_2'(\sigma)$ to $w_2(\sigma)$ and has the following asymptotic form

$$\psi_2(\sigma) = \frac{w_2'(\sigma)}{w_2(\sigma)} \sim \sqrt{\sigma} - \frac{1}{4\sigma} + O\left(\frac{1}{\sigma^2}\right) \quad (\text{B-25})$$

Substituting (B-25) into (B-24), expanding (B-24), and retaining only the terms of order $1/ka$ leads to

$$P_v(ka; \alpha_h) \sim - \frac{1}{m^{-1} \sqrt{\sigma} - \frac{\alpha_h}{k}} \left[1 + \frac{1}{2} \frac{1}{(m^{-1} \sqrt{\sigma})^2 \left[m^{-1} \sqrt{\sigma} - \frac{\alpha_h}{k} \right]} \cdot \frac{1}{ka} + O\left(\frac{1}{[ka]^2}\right) \right] \quad (\text{B-26})$$

Substituting (B-26) into (B-11) and keeping only the terms up to the order of $\left(\frac{1}{[ka]^2}\right)$ leads to

$$G_p^h \sim G_{p_0}^h + G_{p_1}^h \left(\frac{1}{ka}\right) + O\left(\frac{1}{[ka]^2}\right) \quad (\text{B-27})$$

where

$$G_{p_0}^h = -\frac{j\alpha_h}{2k} \frac{e^{-jka|\phi|}}{2\pi j} \int_{-j\infty}^{j\infty} ds \frac{e^{\frac{1}{2}a|\phi|s}}{\sqrt{s}(\sqrt{s} + j\sqrt{j}\alpha_h k^{-\frac{1}{2}})} \quad (B-28)$$

and

$$G_{p_1}^h = \frac{1}{4} j\sqrt{j} \alpha_h \sqrt{k} \frac{e^{-jka|\phi|}}{2\pi j} \int_{-j\infty}^{j\infty} ds \frac{2\sqrt{s} + j\sqrt{j}\alpha_h k^{-\frac{1}{2}}}{s^2(\sqrt{s} + j\sqrt{j}\alpha_h k^{-\frac{1}{2}})^2} e^{\frac{1}{2}a|\phi|s} \quad (B-29)$$

In the process of obtaining (B-28) and (B-29) one employs a change of variable $s = -j2(\frac{\sigma}{a} - k)$. In the s domain, (B-23c) becomes $\sigma = \frac{ja}{2m} s$, and naturally, $m^{-1}\sqrt{\sigma} = \sqrt{js/k}$.

Equations (B-28) and (B-29) are in the form of an inverse Laplace transformation. Equation (B-28) can be readily evaluated using standard Laplace transformation tables [28]:

$$G_{p_0}^h = -\frac{j\alpha_h}{2k} e^{-jka|\phi|} \operatorname{erfc}\left(j \left[\frac{\sqrt{j}\alpha_h}{\sqrt{2}k}\right] \sqrt{ka|\phi|}\right) e^{-ka|\phi| [\sqrt{j}\alpha_h/\sqrt{2}k]^2} \quad (3-30)$$

Since $\operatorname{erfc}(-z) = 2 - \operatorname{erfc}(z)$ and $z = j \left[\frac{\sqrt{j}\alpha_h}{\sqrt{2}k}\right] \sqrt{ka|\phi|}$, one can rewrite (B-30) as follows

$$G_{p_0}^h = -\frac{j\alpha_h}{k} e^{-jka|\phi|} \epsilon_h - \frac{j\alpha_h^-}{k\sqrt{\pi}} e^{-jka|\phi|} Q(j\tilde{b}_h \sqrt{ka|\phi|}) e^{-ka|\phi| \tilde{b}_h^2} \quad (B-30b)$$

Again, in (B-30b) $\tilde{b}_h = \frac{\alpha_h^-}{k} \sqrt{\frac{j}{2}}$ and $\alpha_h^- = -|\alpha_h|$.

Comparing (B-19) with (B-30b) reveals that they both are the same with the exception that the surface wave term in (B-19) is more accurate than the one in (B-30b). It can be shown that (B-30b) is the limiting case of (B-19) for small impedances (i.e., α_h is small, $\beta_h \sim k$). The second term, $G_{p_1}^h$ in (B-27) can easily be calculated from (B-29), if one recognizes that (B-29) can be rewritten as follows:

$$G_{p_1}^h = - \frac{e^{-jka|\phi|}}{4} \frac{k^2}{2\pi j} \int_{-j\infty}^{j\infty} ds e^{\frac{1}{2} a|\phi|s} \left[\frac{1}{k^2 s^2} - \frac{j}{\alpha_h s} - \frac{j}{\alpha_h} \left(1 - \alpha_h \frac{d}{d\alpha_h} \right) \cdot \frac{1}{\sqrt{s}(\sqrt{s} + j\sqrt{j}\alpha_h k^{-\frac{1}{2}})} \right] \quad (B-31)$$

Equation (B-31) can now be evaluated with the aid of a Laplace transformation table, yielding

$$G_{p_1}^h = - \frac{jk^2}{4\alpha_h^2} e^{-jka|\phi|} \left(\frac{jk|\phi|}{2} \frac{\alpha_h^2}{k^2} + 1 \right) + 2 \left(1 - \alpha_h \frac{d}{d\alpha_h} \right) \left\{ \frac{kG_{p_0}^h}{j\alpha_h} \right\} \quad (B-32)$$

In obtaining (B-32) from (B-31), the definition of $G_{p_0}^h$ in (B-30) is also used. The explicit form of the derivative in (B-21) can be found by simply differentiating (B-30b) with respect to α_h :

$$\alpha_h \frac{d}{d\alpha_h} \left\{ \frac{kG_{p_0}^h}{j\alpha_h} \right\} = \frac{j\alpha_h}{k} \sqrt{\frac{jk|\phi|}{2}} e^{-jka|\phi|} + \frac{j\alpha_h^2 a|\phi|}{k\sqrt{\pi}} e^{-jka|\phi|} Q(j\sqrt{j}\alpha_h k|\phi|) e^{-jka|\phi|} \tilde{b}_h^2; \quad \alpha_h \geq 0 \quad (B-33)$$

Comparison of (B-21) and (B-22) with (B-32) and (B-33) reveals that the latter pair is the special case of the former pair for small impedances, and larger arc lengths, $a|\phi|$. It can be seen that in the limit as $a|\phi|$ becomes large and α_h becomes small, which is the region where the Watson approximation is valid, the Debye approximation goes to the Watson approximation smoothly; whereas, one can not obtain the Debye approximation from the Watson approximation for small values of $a|\phi|$ which is the region where Debye approximation is valid. Hence, one concludes that the representation given in part (Ia) is superior to the one given in part (Ib) of this appendix.

c. Creeping Wave Formulation

Even though one can directly obtain the creeping wave modal representation for (B-8), it is more convenient for later purposes to use (B-7) with $\rho=\rho'=a$ and $\phi'=0$ (i.e., both the source point and the observation point are located on the surface of the impedance cylinder and arc length is measured from the source point). This specialized form of (B-7) is given as follows:

$$G^h = -\frac{1}{2\pi} \int_{-\infty-j\epsilon}^{\infty-j\epsilon} d\left(\frac{\nu}{ka}\right) \frac{H_\nu^{(2)}(ka)}{H_\nu^{(2)'}(ka) + \frac{\alpha_h}{k} H_\nu^{(2)}(ka)} e^{j\nu|\rho|} \quad (B-34)$$

As mentioned earlier, the creeping wave modal representation is valid for large values of arc length, $a|\phi|$ and it is obtained by evaluating (B-34) via the calculus of residues. To this end, one would use the Watson approximation for the Hankel functions in (B-34), leading to

$$G^h = \frac{e^{-jka|\phi|}}{4\pi m} \int_{-\infty-j\epsilon}^{\infty-j\epsilon} d\sigma \frac{w_2(\sigma)}{w_2'(\sigma) - \alpha_h m k^{-1} w_2(\sigma)} e^{-jk\sigma m|\phi|} \quad (B-35)$$

where the use of (B-23) is made in the process going from (B-34) to (B-35). The location of the poles of the integrand in (B-35) will be denoted by σ_p and they are the solutions of

$$w_2'(\sigma) - \alpha_h m k^{-1} w_2(\sigma) = 0. \quad (B-36)$$

The solution of (B-36) and the extensive numerical tables of the values of σ_p for different ranges of the parameter ($\alpha_h m$) are given elsewhere [20], and they will not be included here for the sake of brevity. From the calculus of residues, it can be shown that

$$G^h \sim -2\pi j \frac{e^{-jka|\phi|}}{4\pi m} \sum_{p=0}^{\infty} \frac{e^{-j\sigma_p^h m|\phi|}}{\sigma_p^h + (\alpha_h m k^{-1})^2} \quad (B-37)$$

where (B-36) and the differential equation for the Airy function (i.e., $w_2''(\sigma) - w_2(\sigma) = 0$) is used in the process of obtaining (B-37). One notes that the root σ_p^h (i.e., $p=0$ case) is chosen such that it corresponds to the surface wave for the inductive surface; whereas, there is no σ_p^h root for the capacitive surface and the summation in (B-37), for this later case, starts from $p=1$ (rather than $p=0$).

II. TM_z or Magnetic Line Dipole Source Excitation Case

The magnetic source density for the TM_z case is denoted by \overline{M}_d , and it is given by

$$\vec{M}_d = \hat{\phi} M_d \frac{\delta(\rho-a) \delta(\phi)}{\rho} \quad (B-38)$$

where M_d is the strength of the source. The tangential magnetic field generated by such a source has only a $\hat{\phi}$ -component and it will be denoted by H_ϕ . H_ϕ can be obtained from the z directed electric field E_z^I generated by an electric line source $\vec{I} = \hat{z} I \frac{\rho(\rho-a)\delta(\phi)}{\rho}$ where I is the strength of the line source. E_z^I satisfies (B-2) and (B-3) with the exception that Y_M is replaced by $Z I$ and α_s is substituted by α_s where α_s is given in (A-31). E_z^I also satisfies the radiation condition for an $e^{j\omega t}$ time dependence.

With above changes, (B-4) becomes

$$E_z^I(\rho', \phi') = -jkZ_0 I G^S(\rho', \phi' | \rho, \phi) \quad (B-39)$$

Using the procedure of [26], one can show that

$$G^S(\rho', \phi' | \rho, \phi) \sim -\frac{j}{8} \int_{-\infty-j\epsilon}^{\infty-j\epsilon} dv \left[H_v^{(1)}(k\rho') - \frac{Q_s H_v^{(1)}(ka)}{Q_s H_v^{(2)}(ka)} H_v^{(2)}(k\rho') \right] \cdot H_v^{(2)}(k\rho) e^{-jv|\phi-\phi'|} ; \rho > \rho' \quad (B-40)$$

where $Q_s = \frac{\partial}{\partial [k\rho]} + \frac{\alpha_s}{k}$.

Actually the term $\cos v(\pi - |\phi - \phi'|) / \sin v\pi$ of (B-6) is present in the construction of the complete cylinder Green's function for the TM_z case. However, only the term $j e^{-jv|\phi-\phi'|}$ on the right hand side of (B-6) is of interest in this analysis; this is the only term which is included in (B-40) just as in (B-7). The case for $\rho' > \rho$ can be obtained from (B-40) by interchanging ρ and ρ' . The magnetic field, H_ϕ generated by \vec{I} can be found from $\nabla \times \vec{E} = -j\omega \mu \vec{H}$. The electric field, E_z generated by \vec{M}_d of (A-38) can now be found from reciprocity theorem via the equation $\int \vec{I} \cdot \vec{E} = -M_d \int \hat{\phi} \cdot \vec{H}$ as follows

$$E_z^m(\rho, \phi | \rho', 0) = -M_d \alpha_s G^e(\rho, \phi | \rho', 0) \quad \rho > \rho' \quad (B-41a)$$

$$E_z^m(\rho, \phi | \rho', 0) = M_d k G^e(\rho, \phi | \rho', 0) \quad \rho' > \rho \quad (B-41b)$$

where

$$G^e(\rho, \phi | \rho', 0) = \frac{jk}{8\alpha_s} \int_{-\infty-j\epsilon}^{\infty-j\epsilon} dv \left[H_v^{(1)'}(k\rho') - \frac{Q_s H_v^{(1)}(ka)}{Q_s H_v^{(2)}(ka)} H_v^{(2)'}(k\rho) \right] H_v^{(2)}(k\rho) e^{-jv|\phi|}; \quad \rho' > \rho \quad (B-42a)$$

and

$$G^e(\rho, \phi | \rho', 0) = -\frac{j}{8} \int_{-\infty-j\epsilon}^{\infty-j\epsilon} dv \left[H_v^{(1)}(k\rho) - \frac{Q_s H_v^{(1)}(ka)}{Q_s H_v^{(2)}(ka)} H_v^{(2)}(k\rho) \right] H_v^{(2)'}(k\rho') e^{-jv|\phi|}; \quad \rho' > \rho \quad (B-42b)$$

Equations (B-42a) and (B-42b) can further be simplified for $\rho=a$ and $\rho'=a$, with the aid of the following wronskin relationship

$$H_v^{(2)}(ka) H_v^{(1)'}(ka) - H_v^{(2)'}(ka) H_v^{(1)}(ka) = \frac{4j}{\pi ka}, \quad (B-43)$$

yielding:

$$G^e(\tilde{Q}^+ | Q') = -\frac{1}{2\pi} \int_{-\infty-j\epsilon}^{\infty-j\epsilon} d\left(\frac{v}{ka}\right) \frac{H_v^{(2)}(ka)}{Q_s H_v^{(2)}(ka)} e^{-jv|\phi|};$$

$$\tilde{Q}^+ = \lim_{\epsilon \rightarrow 0} (\rho = a + \epsilon; \phi)$$

$$Q' = (\rho' = a; 0) \quad (B-44a)$$

and

$$G^e(\tilde{Q} | Q') = -\frac{1}{2\pi} \int_{-\infty-j\epsilon}^{\infty-j\epsilon} d\left(\frac{v}{ka}\right) \frac{H_v^{(2)'}(ka)}{Q_s H_v^{(2)}(ka)} e^{-jv|\phi|};$$

$$\tilde{Q} = (\rho = a; \phi)$$

$$Q' = \lim_{\epsilon \rightarrow 0} (\rho' = a + \epsilon; 0) \quad (B-44b)$$

Making use of the other Maxwell's curl equation, $\nabla \times \mathbf{H} = -j\omega\mu_0 \mathbf{E}$, it can be shown that

$$H_{\phi}(\rho, \phi) = -jkY_0 M_d G^S(\rho, \phi | a, 0) \quad (B-45)$$

where

$$G^S(\rho, \phi | a, 0) = \frac{j\alpha_s}{k} \frac{1}{2\pi j} \int_{-\infty-j\epsilon}^{\infty-j\epsilon} d\left(\frac{\nu}{ka}\right) \frac{H_{\nu}^{(2)'}(k\rho)}{H_{\nu}^{(2)'}(ka) + \frac{\alpha_s}{k} H_{\nu}^{(2)}(ka)} e^{-j\nu|\phi|}; \quad \rho > a \quad (B-46)$$

the prime over the Hankel function on (B-46) indicates derivative with respect to the argument. Equation (B-46) is specialized to the case where the source point is on the surface of the cylinder such that $\rho' = a$ and $\phi' = 0$ and the observation point is exterior of the cylinder (i.e., $\rho > \rho' = a$).

The expression in (B-46) can be represented as a perturbation of the fields on the perfectly conducting cylindrical surface as follows:

$$G^S = G_C^S + G_p^S \quad (B-47)$$

where G_C^S is the Green's function for the magnetic line dipole source of (B-38) when this source is placed on a perfectly conducting cylinder. G_p^S is obtained from (B-46) upon taking the limit as α_s tends to infinity. Thus,

$$G_C^S = \frac{1}{2\pi} \int_{-\infty-j\epsilon}^{\infty-j\epsilon} d\left(\frac{\nu}{ka}\right) \frac{H_{\nu}^{(2)'}(ka)}{H_{\nu}^{(2)}(ka)} e^{-j\nu|\phi|} \quad (B-48)$$

Following an analysis which is based on some earlier work by Hassejian and Ishimaru [19], and Pathak and Huang [2] one obtains the following approximation for (B-48):

$$G_C^S \sim \frac{1}{2j} \frac{H_1^{(2)}(ka|\phi|)}{ka|\phi|} \left[1 - \frac{\sqrt{\pi j}}{2} \xi^{3/2} + \frac{j5}{12} \xi^3 + \frac{5}{64} \sqrt{-\pi j} \xi^{9/2} + \dots \right] \quad (B-49)$$

G_p^S is the perturbation Green's function and it is given as follows:

$$G_p^S = -\frac{1}{2\pi} \int_{-\infty-j\epsilon}^{\infty-j\epsilon} d\left(\frac{\nu}{ka}\right) P_\nu(ka; \alpha_s) [P_\nu(ka; 0)]^{-2} e^{-j\nu|\phi|} \quad (B-50)$$

where as before

$$P_\nu(ka; \alpha_s) = \frac{H_\nu^{(2)}(ka)}{H_\nu^{(2)}(ka) + \frac{\alpha_s}{k} H_\nu^{(2)}(ka)} \quad (B-51)$$

One notes that in both (B-48) and (B-50), the observation point, as well as the source point, is brought on to the surface of the cylinder (i.e., $\rho' = \rho = a$).

As in the TE_z case presented in section I of this appendix, the perturbation Green's function, G_p^S of (B-50) can also be evaluated asymptotically for the different ranges of the parameters involved via the Debye, Watson and creeping wave representations for small, moderately small and large values of the arc length, $ka|\phi|$, respectively. In part (IIa) of this appendix, the Debye approximation of (B-50) is examined. The Watson approximation and the creeping wave representation of (B-50) is discussed subsequently in parts (IIb) and (IIc), respectively.

a. Debye Approximation

The series expansion of $P_\nu(ka; \alpha_s)$ resulting from the Debye approximation can simply be obtained from (B-15b) by changing α_h to α_s , which yields

$$P_\nu(ka; \alpha_s) \sim \frac{j}{\sin\eta + j\alpha_s k^{-1}} \left[1 + \frac{j}{2\sin^2\eta} \frac{1}{\sin\eta + j\alpha_s k^{-1}} \frac{\cos\eta}{\nu} + O\left(\frac{1}{\nu^2}\right) \right] \quad (B-52a)$$

It can also be shown that the term $P_\nu^{-2}(ka; 0)$ in (B-50) has the following form when it is expanded via the Debye approximation:

$$P_\nu^{-2}(ka; 0) \sim -\sin^2\eta \left[1 - \frac{j}{ka} \frac{1}{\sin^3\eta} + O\left(\frac{1}{\nu^2}\right) \right] \quad (B-52b)$$

where as before $\cos\eta = \nu/ka$.

Substitution of (B-52) into (B-50) and keeping the terms only up to the order of $1/v^2$, leads to

$$G_p^s \sim G_{p_0}^s + G_{p_1}^s \left(\frac{1}{ka} \right) + O \left(\frac{1}{[ka]^2} \right) \quad (B-53)$$

where

$$G_{p_0}^s = - \frac{1}{2\pi j} \int_{-\infty-j\epsilon}^{\infty-j\epsilon} d\xi \frac{k^2 - \xi^2}{k^2 [\sqrt{k^2 - \xi^2} + j\alpha_s]} e^{-j\xi a|\phi|} \quad (B-54)$$

and

$$G_{p_1}^s = \frac{k}{4\pi} \int_{-\infty-j\epsilon}^{\infty-j\epsilon} d\xi (k^2 - \xi^2) \frac{\sqrt{k^2 - \xi^2} + 2j\alpha_s}{(k^2 - \xi^2)^{3/2} [\sqrt{k^2 - \xi^2} + j\alpha_s]^2} e^{-j\xi a|\phi|} \quad (B-55)$$

A change of variable (i.e., $\xi = \frac{v}{a}$) has been introduced in (B-51) and it is recognized that $\cos v = v/ka$ and $\sin \eta = \sqrt{k^2 - \xi^2}/k$. Comparison of (B-54) and (A-38) reveals that these two equations are the same as long as one uses the arclength, $a|\phi|$ as the distance between the source and the observation point. This distance was denoted by $|x|$ in (A-38). Hence the same argument presented in Appendix I can also be used here for the evaluation of (A-38), this results in

$$G_{p_0}^s \sim \frac{j\alpha_s}{k} \left(- \frac{\alpha_s^2}{k\beta_s} \right) e^{-j\beta_s a|\phi|} \epsilon_s - \left(1 + \frac{d^2}{d[ka|\phi|]^2} \right) \left[\frac{1}{2j} H_0^{(2)}(ka|\phi|) - \frac{1}{2j} H_0^{(2)}(ka|\phi|) 2z e^{z^2} Q(z) \right] + \frac{2\alpha_s}{k} \delta(ka|\phi|) \epsilon_s, \quad (B-56)$$

where, as in Appendix I,

$$\beta_s = \sqrt{k^2 + \alpha_s^2}; \quad z = j\tilde{\beta}_s \sqrt{ka|\phi|} \quad (\text{B-56a})$$

$$\tilde{\beta}_s = \frac{\alpha_s^-}{k} \sqrt{\frac{j}{2}}; \quad \alpha_s^- = -|\alpha_s| \quad (\text{B-56b})$$

In order to evaluate $G_{p_1}^s$, one rewrites (B-55) as follows:

$$G_{p_1}^s = \frac{k}{4\pi} \left(1 - \alpha_s \frac{d}{d\alpha_s}\right) \int_{-\infty - j\epsilon}^{\infty - j\epsilon} d\xi \frac{e^{-j\xi a|\phi|}}{\sqrt{k^2 - \xi^2} [\sqrt{k^2 - \xi^2 + j\alpha_s}] \quad (\text{B-57})$$

Comparison of (B-17) and (B-57) reveals that the integrals involved are the same as long as α_h in (B-17) is replaced by α_s . Hence (B-57) becomes

$$G_{p_1}^s = \frac{1}{2j} \left(1 - \alpha_s \frac{d}{d\alpha_s}\right) \left[\frac{k G_{p_0}^h(\alpha_h \rightarrow \alpha_s)}{j\alpha_s} \right] \quad (\text{B-58})$$

where the notation, $\alpha_h \rightarrow \alpha_s$ in $G_{p_0}^h(\alpha_h \rightarrow \alpha_s)$ of (B-58) indicates that α_h in $G_{p_0}^h$ of (B-19) will be replaced by α_s . Or, more explicitly, (B-58) can be rewritten as

$$G_{p_1}^s = \frac{1}{2j} \left(1 - \alpha_s \frac{d}{d\alpha_s}\right) \left[-\frac{k}{\beta_s} e^{-j\beta_s a|\phi|} \epsilon_s + \frac{e^{-jka|\phi|}}{\sqrt{\pi}} Q(j\tilde{\beta}_s \sqrt{ka|\phi|}) e^{-ka|\phi|\tilde{\beta}_s^2} \right]; \quad \alpha_s \geq 0 \quad (\text{B-59})$$

The derivative term in (B-58) or in (B-59) can be evaluated with the aid of (B-22), resulting with

$$\begin{aligned} \alpha_s \frac{d}{d\alpha_s} \left[\frac{k G_{p_0}^h(\alpha_h \rightarrow \alpha_s)}{j\alpha_s} \right] &= (j\beta_s a|\phi| + 1) \frac{k\alpha_s^2}{\beta_h^3} e^{-j\beta_s a|\phi|} \epsilon_s + \frac{j\alpha_s}{k} \sqrt{\frac{jka|\phi|}{2\pi}} \\ &\cdot e^{-jka|\phi|} + \frac{j\alpha_s^2 a|\phi|}{k\sqrt{\pi}} e^{-jka|\phi|} Q(j\tilde{\beta}_s \sqrt{ka|\phi|}) e^{-k\tilde{\beta}_s^2 a|\phi|}; \quad \alpha_s \geq 0 \end{aligned} \quad (\text{B-60})$$

b. Watson Approximation

For moderately small distances from the source, one again employs the Watson approximation. In order to apply this approximation, one again starts by approximating the Hankel functions by the Fock-type Airy functions as in (B-23). Following the arguments presented in part (Ib), the Watson approximation for $P_v(k\alpha; \alpha_s)$ of (B-51) can be readily written from (B-26) upon changing α_h to α_s ; that is

$$P_v(k\alpha; \alpha_s) \sim -\frac{1}{m^{-1}\sqrt{\sigma}-\alpha_s k^{-1}} \left[1 + \frac{1}{2} \frac{1}{(m^{-1}\sqrt{\sigma})^2 [m^{-1}\sqrt{\sigma}-\alpha_s k^{-1}]} \frac{1}{ka} + 0\left(\frac{1}{[ka]^2}\right) \right] \quad (B-61)$$

where as before $\sigma = m^{-1}(\nu - ka)$ and $2m^3 = ka$. It can also be simply shown that $P_v^{-2}(ka; 0)$ has the following form

$$P_v^{-2}(ka; 0) \sim (m^{-1}\sqrt{\sigma})^2 \left[1 - \frac{1}{(m^{-1}\sqrt{\sigma})^3} \frac{1}{ka} + 0\left(\frac{1}{[ka]^2}\right) \right] \quad (B-52)$$

Substitution of (B-61) and (B-52) into (B-50) yields

$$G_p^s \sim G_{p_0}^s + G_{p_1}^s \frac{1}{ka} + 0\left(\frac{1}{[ka]^2}\right) \quad (B-63)$$

where

$$G_{p_0}^s = \frac{e^{-jka|\phi|}}{2k} \sqrt{\frac{j}{k}} \frac{1}{2\pi j} \int_{-\infty}^{\infty} ds \frac{s}{\sqrt{s+j\sqrt{j/k}\alpha_s}} e^{\frac{1}{2}sa|\phi|} \quad (B-64)$$

and

$$G_{p_1}^s = \frac{j}{4} e^{-jka|\phi|} \frac{1}{2\pi j} \int_{-\infty}^{\infty} ds \frac{\sqrt{s} + 2j\sqrt{j/k}\alpha_s}{\sqrt{s}[\sqrt{s+j\sqrt{j/k}\alpha_s}]} e^{\frac{1}{2}sa|\phi|}. \quad (B-65)$$

In the process of obtaining (B-64) and (B-65), one employs a change of variable $s = -j2\left(\frac{\nu}{a} - k\right)$; and naturally $m^{-1}\sqrt{\sigma} = \sqrt{js/k}$.

Evaluation of (B-64) via the method of inverse Laplace transformation yields

$$G_{p_0}^S = e^{-jk|\phi|} \frac{d}{d(ka|\phi|)} \left\{ \sqrt{\frac{2j}{\pi ka|\phi|}} + \frac{\alpha_s}{k} \operatorname{erfc} \left(j \left[\frac{\sqrt{j\alpha_s}}{\sqrt{2} k} \right] \sqrt{ka|\phi|} \right) e^{-ka|\phi| \left[\frac{\sqrt{j\alpha_s}}{\sqrt{2} k} \right]^2} \right\} \quad (B-66)$$

Since $\operatorname{erfc}(-z) = 2 - \operatorname{erfc}(z)$, and $z = j \left[\frac{\sqrt{j\alpha_s}}{\sqrt{2} k} \right] \sqrt{ka|\phi|}$, one can show that

$$G_{p_0}^S = -\frac{j\alpha_s^3}{k^3} e^{-jka|\phi| \left(1 + \frac{\alpha_s^2}{2k^2} \right)} \epsilon_s + e^{-jka|\phi|} \frac{d}{dt} \left\{ \sqrt{\frac{2j}{\pi ka|\phi|}} [1 - 2z e^{z^2} Q(z)] \right\} \quad (B-67)$$

Comparison of (B-67) with the results obtained from the Debye approximation for $G_{p_0}^S$ given in (B-56) reveals after some manipulation that (B-56) reduces to (B-67) for large values of the arclength, $ka|\phi|$ and small values of α_s ; whereas, one needs to conjecture that

$$\left(e^{-jka|\phi|} \frac{d}{d(ka|\phi|)} \sqrt{\frac{2j}{\pi ka|\phi|}} \right)$$

should be replaced by

$$\left(-\frac{1}{2j} \frac{H_1^{(2)}(ka|\phi|)}{ka|\phi|} \right)$$

in order to obtain (B-56) from (B-67). (It is noted that the previous expression is the large argument approximation of the latter one.)

Hence, one concludes that (B-56) is a more general result than (B-67) because (B-56) goes to (B-67) for large values of the arclength where (B-67) is valid; whereas, (B-67) does not readily go to (B-56) for small values of the arclength where (B-56) is valid.

In order to evaluate $G_{p_1}^S$ of (B-65), one rewrites the equation as follows

$$G_{p_1}^S = \frac{j}{4} e^{-jka|\phi|} \left(1 - \alpha_s \frac{d}{d\alpha_s} \right) \left[\frac{1}{2\pi j} \int_{-\infty}^{\infty} ds \frac{e^{\frac{1}{2}sa|\phi|}}{\sqrt{s} [\sqrt{s+j\sqrt{j/k}} \alpha_s]} \right] \quad (B-68)$$

The integrals in (B-28) and (B-68) are the same with the exception that α_h in the former is replaced by α_s in the latter integral.

Hence, (B-68) becomes:

$$G_{p_1}^S = \frac{1}{2j} \left(1 - \alpha_s \frac{d}{d\alpha_s} \right) \left[\frac{k G_{p_0}^h(\alpha_h \rightarrow \alpha_s)}{j\alpha_s} \right], \quad (B-69)$$

where the rotation $\alpha_h \rightarrow \alpha_s$ in (B-69) indicates that α_h in $G_{p_0}^h$ of (B-30b) will be replaced by α_s in (B-69) as before. Or more explicitly

$$G_{p_1}^S = \frac{1}{2j} \left(1 - \alpha_s \frac{d}{d\alpha_s} \right) \left[-e^{-jka|\phi|} \epsilon_s \pm \frac{e^{-jka|\phi|}}{\sqrt{\pi}} Q(jb_s \sqrt{ka|\phi|}) e^{-ka|\phi| \tilde{b}_s^2} \right]; \quad \alpha_s \geq 0 \quad (B-70)$$

Comparison of (B-59) and (B-70) reveals that the latter one is the special case of (B-58) for small values of α_s . One notes that the derivative term in (B-69) or (B-70) can be obtained from (B-33) by changing α_h to α_s .

c. Creeping Wave Formulation

With both the source and the observation points on the surface of the cylinder (i.e., $\rho = \rho' = 0$), (B-46) becomes

$$G^S = \frac{j\alpha_s}{k} \frac{1}{2\pi j} \int_{-\infty-j\epsilon}^{\infty-j\epsilon} d\left(\frac{v}{ka}\right) \frac{H_v^{(2)'}(ka)}{H_v^{(2)'}(ka) + \frac{\alpha_s}{k} H_v^{(2)}(ka)} e^{-jv|\phi|} \quad (B-71)$$

A creeping wave or residue series representation will now be given for (B-77). In the process of obtaining a residue series expansion, one uses the Watson approximation of (B-23) into (B-71), yielding

$$G^S \sim \frac{j\alpha_s e^{-jka|\phi|}}{2km} \frac{1}{2\pi j} \int_{-\infty-j\epsilon}^{\infty-j\epsilon} d\sigma \frac{w_2'(\sigma)}{w_2'(\sigma) - \alpha_s m k^{-1} w_2(\sigma)} e^{-j\sigma m|\phi|} \quad (B-72)$$

The poles of the integrand in (B-72) will be denoted by σ_p^S and they are the roots of following characteristics equation

$$w_2'(\sigma_p) - \alpha_s m k^{-1} w_2(\sigma_p) = 0 \quad (B-73)$$

As indicated earlier for σ_p^h , extensive numerical tables for the values of σ_p^S for different ranges of the parameters (α_m) are also given by Logan [20], and they will not be included here for the sake of brevity. From the calculus of residues and the differential equation for the Airy functions (i.e., $w_2''(\sigma) - w_2(\sigma) = 0$), one can show that

$$G_s \sim - \frac{j\alpha_s^2}{2k^2 m} e^{-jka|\phi|} \sum_{p=0}^{\infty} \frac{e^{-j\sigma_p^S m|\phi|}}{\sigma_p^S - (\alpha_s m k^{-1})^2} \quad (B-74)$$

In the TM_z case, σ_0^S root (i.e., $p=0$ case) corresponds to the surface (or Elliot) wave for the capacitive surface, whereas, there is no σ_0^S root for the inductive surface and the summation in (B-74), for this latter case, starts from $p=1$ (instead of $p=0$).

REFERENCES

1. P. H. Pathak and R. G. Kouyoumjian, "An Analysis of the Radiation from Apertures in Curved Surfaces by the Geometrical Theory of Diffraction," Proc. IEEE, Vol. 62, No. 11, November 1974, pp. 1438-1447.
2. P. H. Pathak and J. Huang, "An MM-GTD Analysis of the Radiation from Slots in Planar and Cylindrical Perfectly-Conducting Structures with a Surface Impedance Patch," Report 4396-1, July 1977, The Ohio State University ElectroScience Laboratory, Department of Electrical Engineering; prepared under Contract F19628-76-C-0154 for Rome Air Development Center, Air Force Systems Command. (AD A046048)
3. R. S. Elliot, "Azimuthal Surface Waves on Circular Cylinders," Jour. of Appl. Phys., Vol. 26, No. 4, April 1955, pp. 368-376.
- 4.* P. Pathak, "A GTD Analysis of the Radiation from Slots in Planar and Cylindrical Perfectly Conducting Structures with a Surface Impedance Patch," Report 4396-2, February 1977, The Ohio State University ElectroScience Laboratory, Department of Electrical Engineering; prepared under Contract F19628-76-C-0154 for Rome Air Development Center, Air Force Systems Command, (RADC-TR-77-156) (AD A041974)
5. P. Pathak and L. Ersoy, "A Continuation of the Study of the Radiation from Slots in Perfectly-Conducting Surfaces which are Partly Covered with an Impedance Surface Patch," Report 784641-1, May 1978, The Ohio State University ElectroScience Laboratory, Department of Electrical Engineering; prepared under Contract F19628-77-C-0127 for Department of the Air Force, Electronic Systems Division, AFSC, Hanscom Air Force Base, Mass. 01731.

*Some typographical errors appearing in [4] are as follows:

1. The minus sign in front of the integral of (A-37) and in front of the terms on the RHF of (A-39) must be replaced by a plus sign. Also, a minus sign must be put on the RHS of (A-45).
2. It is noted that the second term on the RHS of (A-39) contains an extra factor of "k".

6. Y. M. Hwang, R. G. Kouyoumjian and P. H. Pathak, "The Radiation from Slots in Truncated Dielectric-covered Surfaces," NASA CP-2397, June 1974.
7. J. R. Wait, Electromagnetic Waves in Stratified Media, Pergamon Press Book, The McMillan Co., N. Y., 1962.
8. J. R. Wait, "Currents Excited on a Conducting Surface of Large Radius of Curvature," IRE Trans., Vol. MTT-4, No. 3, July 1956, pp. 143-145. (Also see: Hasserjian and Ishimaru, Jour. of Research, N.B.S., Vol. 66D, No. 3, May-June 1962, pp. 335-365.)
9. J. R. Wait, "Radiation from a Vertical Antenna Over a Curved Stratified Ground," Journal of Research of the National Bureau of Standards, Vol. 56, No. 4, April 1956, pp. 237-244.
10. J. R. Wait, "Recent Analytical Investigations of Electromagnetic Ground Wave Propagation over Inhomogeneous Earth Models," Proceedings of IEEE, Vol. 62, No. 8, August 1974, pp. 1061-1072.
11. J. R. Wait, "On the Excitation of Electromagnetic Surface Waves on a Curved Surface," IRE Transactions on Antennas and Propagation, Vol. AP-8, No. 4, July 1960, pp. 445-448.
12. K. P. Spies and J. R. Wait, "On the Calculation of Antenna Patterns for an Inhomogeneous Spherical Earth," Radio Science, Vol. 2, No. 11, November 1967, pp. 1361-1378.
13. J. Shapira and L. B. Felsen and A. Hessel, "Surface Ray Analysis of Mutually Coupled Arrays on Variable Curvature Cylinder Surfaces," Proceedings of the IEEE, Vol. 62, No. 11, November 1974, pp. 1482-1492.
14. J. Shapira, L. B. Felsen and A. Hessel, "Ray Analysis of Conformal Antenna Arrays," IEEE Transactions on Antennas and Propagation, Vol. AP-22, No. 1, January 1974, pp. 49-63.
15. J. H. Richmond, "A Reaction Theorem and its Application to Antenna Impedance Calculations," IRE Trans., Vol. AP-9, No. 6, pp. 515-520, November 1961.
16. V. H. Rumsey, "Reaction Concept in Electromagnetic Theory," Phys. Rev., vol. 94, pp. 1843-1491, June 1954.
17. R. Mittra, "A Vector Form of Compensating Theorem and It's Applications to Boundary Value Problems," Scientific Rept. No. 2, prepared for University of Colorado on Contract AF19(604)-4556 with AFCRL, Bedford, Mass., June 1961.

18. S. W. Lee and S. Naini, "Approximate Asymptotic Solution of Surface Field due to a Magnetic Dipole on a Cylinder," IEEE Trans., Vol. AP-26, No. 4, pp. 593-597, July 1978.
19. Hasserjian and Ishimaru, Jour. of Research, N.B.S., Vol. 66D, No. 3, May-June 1962, pp. 335-365.
20. N. A. Logan, "General Research in Diffraction Theory," Missiles and Space Div., Lockheed Aircraft Corp., Vol. 1, Rep. LMSR-288087 and Vol. 2, Rep. LMSD-288088, December 1959.
21. H. Bremmer, Terrestrial Radio Waves, Theory of Propagation, Elsevier Publishing Company, Inc., New York, 1949.
22. V. A. Fock, Electromagnetic Diffraction and Propagation Problems, New York, Pergamon, 1965.
23. C. H. Walter, Traveling Wave Antennas, Dover Publications, Inc., New York, 1965.
24. R. C. Hansen, "Single Slab Arbitrary Polarization Surface Wave Structure," IRE Trans. Microwave Theory Tech., MTT-5: 115, 1957.
25. Collin and Zucker Eds., Antenna Theory, Pt. II, New York, McGraw-Hill, 1969.
26. L. B. Felsen and N. Marcuvitz, Radiation and Scattering of Waves, Prentice-Hall, Inc., New Jersey, 1973.
27. L. Boersma and S. W. Lee, "Surface Field Due to a Magnetic Dipole on a Cylinder: Asymptotic Expansion of Exact Solution," Electromagnetics Laboratory, Department of Electrical Engineering, University of Illinois at Urbana-Champaign, Technical-Report No. 78-17, December 1978, Department of the Navy, Naval Air Systems Command, Washington, D.C. Cont. No. N00019-78-C-0064.
28. Handbook of Mathematic Functions, National Bureau of Standards, Applied Mathematical series 55, November 1970.



MISSION of Rome Air Development Center

RADC plans and executes research, development, test and selected acquisition programs in support of Command, Control Communications and Intelligence (C³I) activities. Technical and engineering support within areas of technical competence is provided to ESD Program Offices (POs) and other ESD elements. The principal technical mission areas are communications, electromagnetic guidance and control, surveillance of ground and aerospace objects, intelligence data collection and handling, information system technology, ionospheric propagation, solid state sciences, microwave physics and electronic reliability, maintainability and compatibility.

Printed by
United States Air Force
Hanscom AFB, Mass. 01731